



HAL
open science

Numerical study of 2D stratified turbulence forced by internal gravity waves

Miguel Calpe Linares

► **To cite this version:**

Miguel Calpe Linares. Numerical study of 2D stratified turbulence forced by internal gravity waves. Fluid mechanics [physics.class-ph]. Université Grenoble Alpes, 2020. English. NNT: 2020GREAI008 . tel-02612797v1

HAL Id: tel-02612797

<https://theses.hal.science/tel-02612797v1>

Submitted on 19 May 2020 (v1), last revised 20 May 2020 (v2)

HAL is a multi-disciplinary open access archive for the deposit and dissemination of scientific research documents, whether they are published or not. The documents may come from teaching and research institutions in France or abroad, or from public or private research centers.

L'archive ouverte pluridisciplinaire **HAL**, est destinée au dépôt et à la diffusion de documents scientifiques de niveau recherche, publiés ou non, émanant des établissements d'enseignement et de recherche français ou étrangers, des laboratoires publics ou privés.

THÈSE

Pour obtenir le grade de

DOCTEUR DE L'UNIVERSITE GRENOBLE ALPES

Spécialité : **Mécanique des fluides, procédés, énergétique**

Arrêté ministériel : 25 mai 2016

Présentée par

Miguel CALPE LINARES

Thèse dirigée par **Nicolas MORDANT**
et coencadrée par **Pierre AUGIER**

préparée au sein du **Laboratoire des Écoulements
Géophysiques et Industriels** dans l'École Doctorale **IMEP2**

Étude numérique de la turbulence stratifiée 2D forcée par des ondes internes de gravité

Numerical study of 2D stratified turbulence forced by internal gravity waves

Thèse soutenue publiquement le **26 février 2020**,
devant le jury composé de :

M. Sylvain JOUBAUD

Mâitre de conférences, ENS Lyon, Rapporteur

M. Wouter BOS

Chargé de recherche, École Centrale Lyon, Rapporteur

M. Paul BILLANT

Directeur de recherche, École Polytechnique, Examineur

M. Joël SOMMERIA

Directeur de recherche, Université Grenoble Alpes, Président

M. Nicolas MORDANT

Professeur des universités, Université Grenoble Alpes, Directeur de thèse

M. Pierre AUGIER

Chargé de recherche, Université Grenoble Alpes, Co-encadrant de thèse



Abstract

The oceanic motions are composed of eddies with a very large horizontal scale and 3D propagating internal gravity waves. Its kinetic energy spectra follow the well-known Garrett and Munk spectrum, which is usually interpreted as the signature of interacting internal gravity waves. Our main motivation is to reproduce the turbulence regime observed in nature by forcing waves.

Two-dimensional (2D) stratified flows on a vertical cross-section differ from its analogous three-dimensional flows in its lack of vertical vorticity, supporting only waves and shear modes. In this PhD work, we perform a numerical study of 2D stratified turbulence forced with internal gravity waves. We get rid of the shear modes, sustaining a system only with wave modes. Unlike precedent studies, the forcing is applied to a localized region of the spectral space, in which forced internal waves have a similar time scale. We force intermediate-scale waves to allow the dynamics to develop both upscale and downscale energy cascade.

We first present the different regimes of 2D stratified turbulence with a particular interest in the ocean-like regime, i.e. strong stratification and large Reynolds number. The dynamics of the energy cascade is analysed by means of the spectral energy budget. Furthermore, we check if it is possible to obtain turbulence driven by weakly non-linear interacting waves by performing a spatio-temporal analysis. To conclude, we report results of numerical simulations forced either on the vorticity or on the eigenmode of the Navier-Stokes equations in order to study the degree of universality of 2D stratified turbulence with respect to the forcing.

Résumé

Les écoulements océaniques sont composés des tourbillons ayant une grande échelle horizontale et des ondes internes de gravité. Le spectre d'énergie cinétique suit le fameux spectre de Garrett et Munk qui est habituellement interprété comme la signature des ondes internes de gravité. Notre motivation principale est donc de reproduire le régime de turbulence observé dans la nature avec un système forcé seulement avec des ondes.

Les écoulements stratifiés bidimensionnels (2D) sur une section transversale verticale diffèrent des écoulements stratifiés tridimensionnels par l'absence de vorticit  verticale et par la pr sence d'ondes et de modes de cisaillement. Dans ce travail de th se, nous effectuons une  tude num rique de la turbulence stratifi e 2D forc e par des ondes internes de gravit . Nous  liminons les modes de cisaillement pour avoir un syst me uniquement constitu  d'ondes. Contrairement aux  tudes pr c dentes, le for age est appliqu    une r gion localis e de l'espace spectral. Nous for ons aussi les ondes avec une  chelle spatiale interm diaire pour permettre le d veloppement d'une cascade d' nergie directe et aussi inverse.

Nous pr sentons d'abord les diff rents r gimes de turbulence stratifi e 2D avec un int r t particulier au r gime typique de l'oc an avec une forte stratification et un grand nombre de Reynolds. La dynamique de la cascade d' nergie est analys e par un bilan  nerg tique spectral. Ensuite, nous v rifions s'il est possible d'obtenir un r gime de turbulence d'onde faible en r alisant une analyse spatio-temporelle. Nous  tudions enfin le degr  d'universalit  de la turbulence stratifi e 2D par rapport au for age.

Contents

| | | |
|----------|---|-----------|
| 1 | Dynamics of geophysical flows | 7 |
| 1.1 | Atmosphere and ocean's role in the Earth's climate system | 7 |
| 1.1.1 | Large-scale circulation of the Earth's ocean | 8 |
| 1.1.2 | Deep ocean circulation and climate change | 9 |
| 1.1.3 | Energy for maintaining the large-scale ocean's circulation | 9 |
| 1.1.4 | The effect of rotation on the atmosphere and ocean dynamics | 11 |
| 1.2 | Density stratification of the ocean and the atmosphere | 11 |
| 1.2.1 | Stable density stratification: the buoyancy frequency | 13 |
| 1.2.2 | Linear internal gravity waves | 13 |
| 1.3 | Ocean and atmosphere are turbulent flows | 17 |
| 1.3.1 | Atmospheric turbulence | 18 |
| 1.3.2 | Ocean turbulence | 19 |
| 1.3.3 | Ocean observations interpreted as a pure wave mechanism: the Garrett - Munk spectra | 19 |
| 1.4 | Turbulence in stratified fluids | 21 |
| 1.4.1 | The Froude number in the strongly stratified turbulence regime | 21 |
| 1.4.2 | Scaling analysis and the buoyancy Reynolds number | 22 |
| 1.4.3 | Coupling of the horizontal motions and internal waves | 23 |
| 1.4.4 | Direct energy cascade in strongly stratified turbulence | 24 |
| 1.4.5 | Internal waves and stratified turbulence | 24 |
| 1.5 | Problem statement | 25 |
| 1.6 | Objectives of this thesis | 27 |
| 2 | Theory of 2D stratified turbulence | 29 |
| 2.1 | Spectral description: the Fourier transform | 29 |
| 2.2 | Eigenmodes of the linear 2D Navier-Stokes equations | 30 |
| 2.3 | Scaling analysis 2D stratified turbulence | 33 |
| 2.3.1 | Weakly stratified flows $F_h \sim 1$ | 34 |
| 2.3.2 | Strongly stratified flows $F_h \rightarrow 0$ | 34 |
| 3 | Numerical setup and characteristic simulation | 37 |
| 3.1 | ns2d.strat: 2D Boussinesq equations solver | 37 |
| 3.2 | Forcing scheme | 38 |
| 3.2.1 | About the forcing region: ring-shaped versus rectangular | 38 |
| 3.2.2 | About the forcing quantity: vorticity $\hat{\xi}$ versus linear mode \hat{a}_+ | 40 |
| 3.2.3 | Normalization of the forcing in the solver ns2d.strat | 41 |
| 3.3 | Time scales of the problem | 42 |
| 3.4 | Output modules of the solver ns2d.strat | 45 |
| 3.5 | Description of a characteristic simulation | 47 |
| 3.5.1 | With or without shear modes? | 47 |
| 3.5.2 | How is the structure of the flow? | 49 |

| | | |
|----------|---|------------|
| 3.5.3 | Energy transfer mechanisms | 53 |
| 3.6 | Computation of the hyper-viscosity coefficient ν_8 | 54 |
| 4 | Effects of varying the stratification and the Reynolds number | 57 |
| 4.1 | Effects of varying the stratification strength | 58 |
| 4.2 | Effects of varying the Reynolds number | 76 |
| 4.3 | Varying stratification and Reynolds number | 80 |
| 4.4 | Regimes in 2D stratified turbulence | 86 |
| 4.5 | Description of flows with $F_{h,f} < 0.5$ and $\mathcal{R}_8 > 1$ | 88 |
| 5 | Is 2D stratified turbulence driven by internal gravity waves? | 93 |
| 5.1 | The spatio-temporal energy spectra | 94 |
| 5.2 | Where are internal waves most likely to develop? | 100 |
| 6 | Effects of varying the forcing | 103 |
| 7 | Conclusions and perspectives | 109 |

Chapter 1

Introduction to the dynamics of geophysical flows

Geophysical flows such as the atmosphere and oceans play a critical role in the Earth's climate system. They are the major contributors to the transport of heat from the subtropical latitudes to the polar regions. In particular, almost all the transport of heat from the equator to the poles, is achieved by currents, turbulent eddies and waves. Understanding the character of these eddy transports is crucial if we want to understand the response of the planets climate to changes in the external forcing. Moreover, the dynamics of geophysical flows is strongly affected by density stratification. The atmosphere is stratified in temperature, and the ocean is stratified in both temperature and salinity. Our main motivation is to better understand the dynamics of turbulent flows strongly affected by the density stratification by means of Direct Numerical Simulations (DNS). In this chapter, I introduce the role of oceans and the atmosphere on the global climate system. I review the notion of the density stratification and its consequences on geophysical flows. Finally, I present the stratified turbulence approach which describes accurately some ocean and atmospheric turbulence measurements.

1.1 Atmosphere and ocean's role in the Earth's climate system

The atmosphere and oceans are crucial elements of the Earth's climate system (Pedlosky, 1987; Vallis, 2006). The ocean, together with the atmosphere, transports heat away from the equator toward higher latitudes thereby keeping the equator to pole temperature difference to less than 40°C . In the absence of the ocean and atmosphere, the temperature difference would exceed 100°C . In the atmosphere, the mechanisms responsible of the heat transport are large-scale eddies. The largest and most energetic eddies in the atmosphere have scales in excess of 1000 km, while large eddies in the ocean are typically on the order of 100 km in size. In the ocean, mesoscale eddies (10-100 km) and internal waves play an important role in the transport of heat, carbon and other climatically important tracers across the oceans (Wunsch, Ferrari, 2004). Figure 1.1 displays the Gulf stream. It is a warm and swift Atlantic ocean current that originates in the Gulf of Mexico, and follows the eastern coastlines of the United States before crossing the Atlantic Ocean. It is responsible of the heat transport from the Equator to middle and high latitudes. One can observe the formation of mesoscale eddies right next to the coastlines of the United States. These mesoscale eddies emerge mainly due to the strong horizontally sheared motions. At slightly smaller scales, sub-mesoscale eddies, order of tens of kilometers, are generated by the misalignment of the pressure gradient with the density gradient in a process known as

baroclinic instability. Both mechanisms lead to hot spots of eddy energy in the vicinity of the Gulf stream and the Antarctic Circumpolar Current.

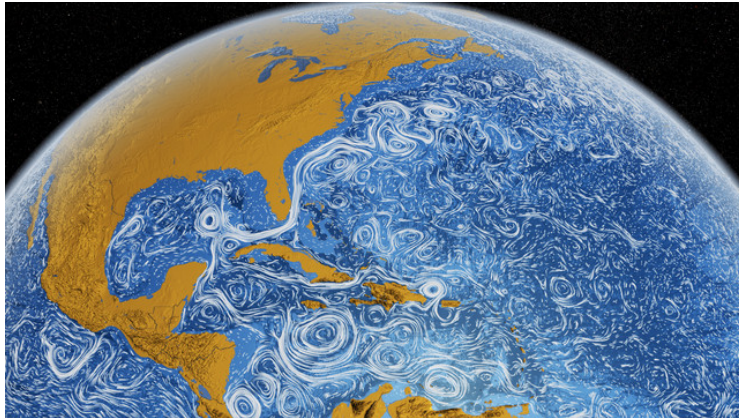


Figure 1.1: The Gulf stream is an Atlantic ocean current which transports heat from the the subtropical regions to the high latitudes. The interaction of the current with the continental coastlines generates the mesoscale eddies. The image was generated by NASA using a simulation run with the MIT general circulation model as part of the ECCO project.

Furthermore, the ocean participates in storing carbon dioxide from the atmosphere (Rahmstorf, 2002; Schuster, Watson, 2007). The ocean stores 60 times more carbon than the atmosphere thereby keeping the greenhouse effect at bay. The ocean is also a key regulator of life on our planet: ocean phytoplankton generates half of the oxygen we breath. It is absolutely necessary to understand how the ocean achieves these global effects. This requires understanding the physics that drives large scale currents on scales of thousand of kilometers down to the swirls that mix waters on scales of millimeters.

1.1.1 Large-scale circulation of the Earth's ocean

The ocean circulation is the result of a balance between wind forcing and air-sea heat and freshwater fluxes at planetary scales and dissipation at centimeter scales (Wunsch, Ferrari, 2004; Vallis, 2006; Ferrari et al., 2014). The ocean circulation can be therefore divided into two main components: a fast and energetic wind-driven surface circulation, and a slow and large density-driven circulation which dominates the deep sea. Wind-driven circulation is by far the most dynamic. Blowing wind produces currents at the surface of the ocean which are oriented at 90 degrees to its direction due to the Earth rotation (Ekman transport). As a consequence, it creates zones of convergence or divergence of ocean currents at the point where they meet. Divergence of currents creates an upwelling phase (interior waters reach the surface) and convergence a downwelling phase (surface waters sink in the interior ocean). The Gulf stream, discussed in figure 1.1, is wind-driven ocean current.

The slow and deep circulation, also called thermohaline circulation, is largely driven by water density, and thus its temperature and salinity. It acts on the ocean as a whole and has a major influence on the abyssal properties where wind-driven circulation has no effect. Figure 1.2 is a schematic representation of the thermohaline circulation. In the Artic and Antarctic regions, the cold dense water sinks and spreads over the entire ocean basins. The replacement of these dense sinking waters generates a continuous surface flow coming from low latitudes.

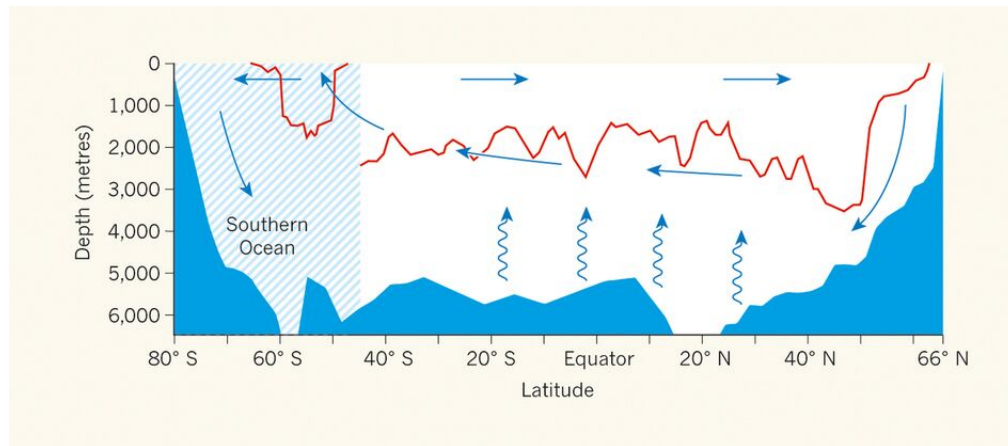


Figure 1.2: Schematic representation of the thermohaline circulation. Deep ocean water masses are formed in the Arctic and Antarctic regions (high latitudes) by sinking of dense water (downwards arrows). The replacement of these deep water masses generates a continuous surface flow coming from low latitudes (horizontal arrows). In the equator deep waters close the loop by going up to the surface (upwards arrows in the equator). Image extracted from the website MIT Earth, Atmospheric and Planetary Science Department.

1.1.2 Deep ocean circulation and climate change

The deep ocean is a huge storehouse of heat, carbon, oxygen and nutrients. Deep ocean circulation regulates uptake, distribution and release of these elements. The low overturning rate stabilizes our global climate. By carrying oxygen into the deeper layers it supports the largest habitat on earth. Recent theories predict that global warming will have a negative impact on the deep ocean circulation. Most studies have focused on the northern Atlantic (Broecker, 2003). The formation of dense sinking surface water in the Arctic region will be counteracted by a higher atmospheric temperature and by release of fresh water by ice melting. The feeding of the Atlantic Meridional Overturning Circulation, which drives warm Gulf Stream waters to the north, will thus be reduced. Besides, the density of the North Atlantic Deep Water will be lower. The cold return current will flow closer to the ocean surface. It is expected that these factors will cause significant cooling of the West European climate. Ice melting and resulting fresh water releases in the Antarctic region will hamper the formation of Antarctic Bottom Water (AABW). Model simulations indicate that this may entail considerable warming of deep waters in the entire Pacific. The impact of fresh water releases in the Antarctic region on the global climate and sea-level rise could even be greater than the impact of freshening of the Arctic waters.

1.1.3 Energy for maintaining the large-scale ocean's circulation

To maintain the large-scale thermohaline circulation of the ocean, it has been estimated that about 2.1 TW (10^{12} Watts) of mixing energy is required (Munk, Wunsch, 1998). Figure 1.3 quantifies the energy exchanged in all ocean processes. It has long been recognized that winds and tides are two important sources of mechanical energy to drive the ocean interior mixing. Although most of the tidal energy from Moon and Sun on the global ocean is dissipated in the shallow seas, perhaps 1.0 TW or more of the tidal energy dissipation occurs in the deep ocean through the scattering by ocean-bottom topography of surface tides into internal tidal waves (Egbert, Ray, 2000). The breaking of internal waves is believed to be a principal contributor to pelagic turbulence.

The winds can also generate internal gravity waves in the surface layer of Earth’s oceans, which are called near-inertial oscillations due to the peak wave energy near the inertial frequency. They are thought to play an important role in diapycnal mixing to sustain the global system of thermohaline circulation. But the exact contribution of wind power to these near-inertial motions and wind’s relative importance compared to tidal forces remain topics of debate (Liu et al., 2019).

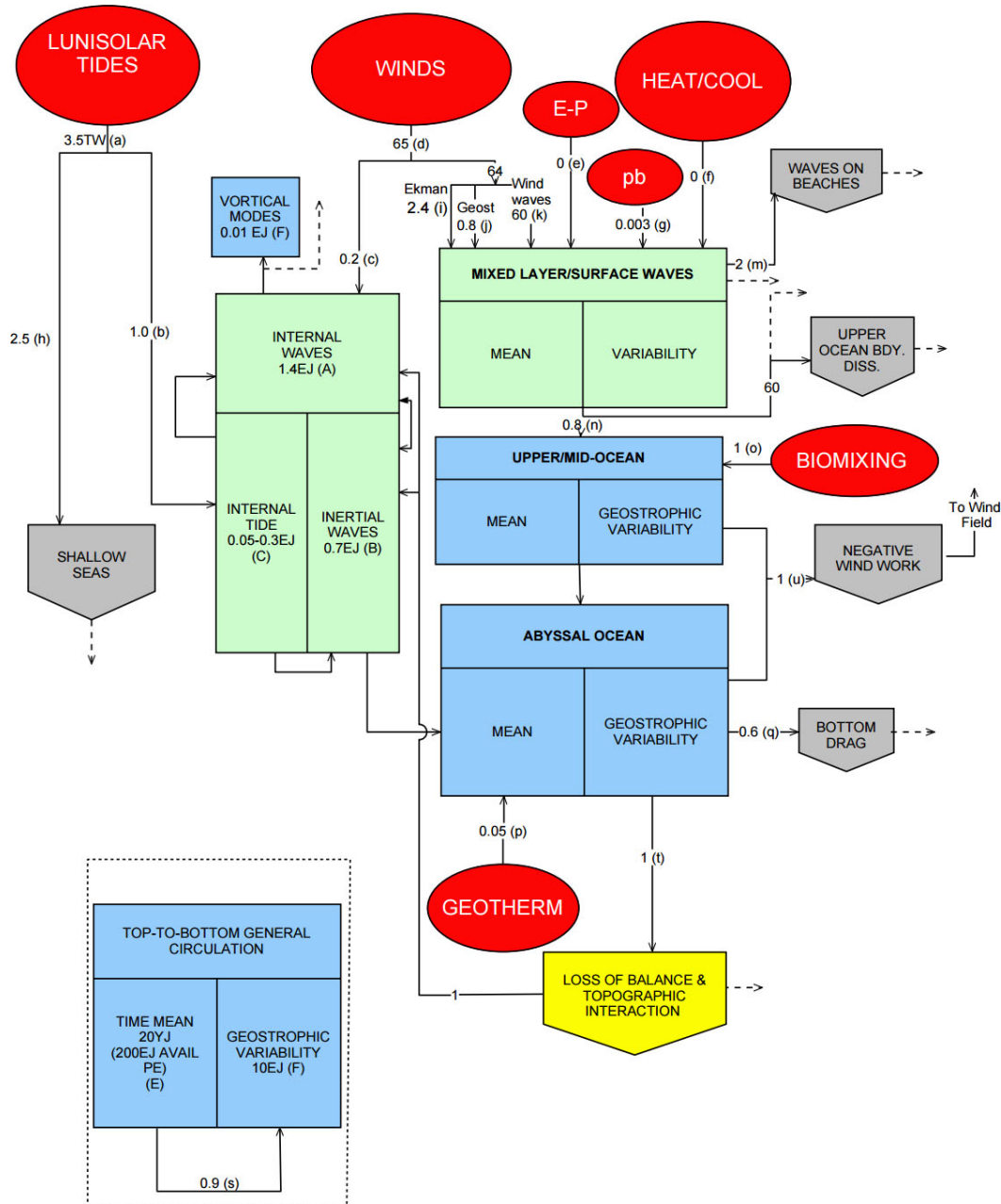


Figure 1.3: Global energy budget of the Earth’s oceans. The arrows represent the energy fluxes in terawatts ($1 \text{ TW} = 10^{12} \text{ Watts}$). Image extracted from Ferrari, Wunsch (2010).

1.1.4 The effect of rotation on the atmosphere and ocean dynamics

The dynamics of the atmosphere and the ocean are affected by the Earth's rotation, and the importance of this effect varies with scale. The influence of rotation and density stratification weakens as one moves downscale. The rotation is present through the horizontal component of the Coriolis force, $f = 2\Omega_0 \sin \lambda$ (Coriolis parameter), where $\Omega_0 \simeq 7.3 \times 10^{-5}$ rad/s is the angular speed of the Earth and λ is the latitude. The non-dimensional quantity which quantifies the rotation effects is the Rossby number $Ro = U/fL$, where U and L are the characteristic velocity and length scales, and f is the Coriolis parameter. According to the classical view, rotation weakens more rapidly than stratification over most of the atmosphere and ocean (Waite, Bartello, 2006a). The typical time scale of the stratification is indeed smaller than the rotation time scale. The atmospheric mesoscale (10-100 km) and oceanic submesoscale (1-10km) are characterized by strong stratification, but only moderate rotation $Ro \gtrsim 1$ (Emanuel, 1986). Stratified turbulence without the rotation effects (with $Ro = \infty$) is often studied as a first approximation to this regime. In this PhD work, I do not consider the rotation effects.

1.2 Density stratification of the ocean and the atmosphere

A density stratified environment is a medium that changes its density with its vertical location. When difference of density exists within a fluid, it tends to redistribute so that the lighter fluid remains above the heavier forming a stable stratification profile. This particular configuration is stable in time and if not perturbed, static. When the fluid is slightly vertically displaced from its equilibrium position, it feels a buoyancy restoring force opposite to the direction of the displacement. Furthermore, it is responsible of the generation of the oscillatory motions in the atmosphere and the oceans.

Atmosphere. The atmosphere is divided in four main layers as displayed in figure 1.4 (left). The bottom layer is called the troposphere at a height 10 km from the Earth's surface. At this layer, turbulence is generated as wind blows over the Earth's surface and thermals rising from the land. The stratosphere extends upwards from the troposphere to about 50 km. These two layers contain most of the energy of the atmosphere. The region above the stratosphere is called mesosphere. Finally, the thermosphere extends to about 600 km altitude.

We now focus on the temperature profile of the atmosphere. A different quantity than the *in situ* temperature is usually used to get rid of the increasing/decreasing of temperature due to compression/expansion of a fluid parcel. This quantity is called the potential temperature. Figure 1.4 (right) displays both *in situ* and potential temperature profiles in the troposphere and stratosphere. One can observe that the decrease of temperature in the troposphere (blue line) is associated mainly with the decrease of pressure with height since the potential temperature (red line) slightly increases with height. In the stratosphere, the potential temperature still increases while the *in situ* temperature remains constant. We can conclude that the potential temperature increases with height indicating that the atmosphere is stable overall.

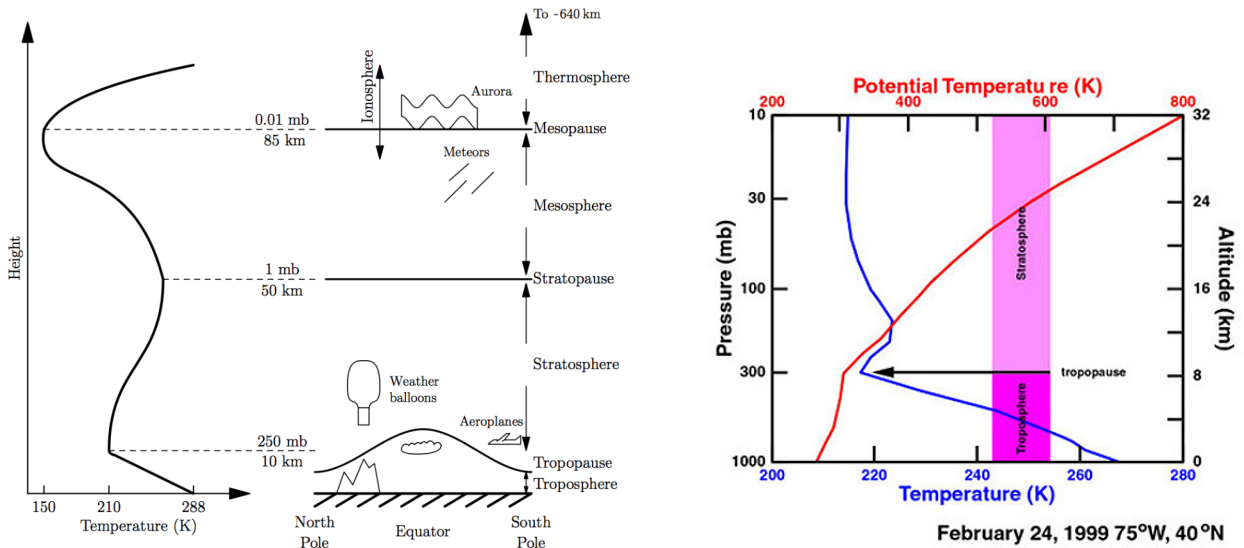


Figure 1.4: Schematic representation of the four main layers of the atmosphere extracted from Sutherland (2010) (left). Temperature and potential temperature profiles of the troposphere and stratosphere on 24th February 1999 at a middle latitude (right).

Oceans. The internal structure of the ocean has taken longer to be measured because it is much more inaccessible than the atmosphere. The ocean is composed of three main layers displayed in figure 1.5. The surface zone (about 100 m deep) is homogeneous in both temperature and salinity. This layer undergoes strong mixing generated by contact with the atmosphere through wind and temperature changes. The *Pycnocline* is the layer with the largest density gradient and is located 200-600 m below the ocean surface. This layer inhibits the vertical motion and acts as a barrier between the surface layer and the abyssal layer. The abyssal layer is the deepest layer, about 4 km thick, with a weak density gradient.

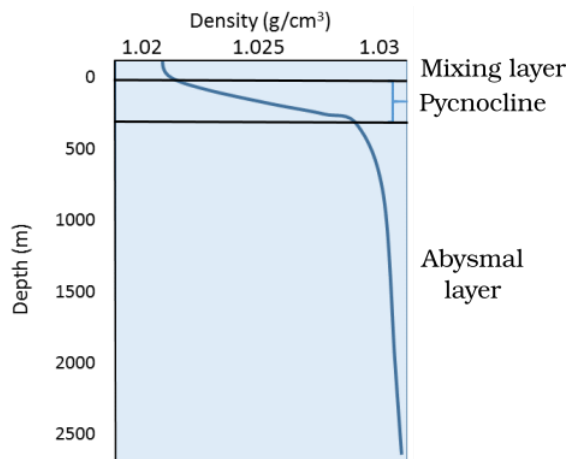


Figure 1.5: Schematic density profile for the open ocean at middle latitudes. Image extracted and modified from Webb (2019).

1.2.1 Stable density stratification: the buoyancy frequency

In section 1.2, we have underlined that the atmosphere and oceans are stratified in density due to the differences in temperature and salinity. All motions parallel to the direction of gravity are affected by a restoring force proportional to the density stratification. Vertical motions are therefore considerably smaller than the horizontal motions. Furthermore, stratified fluids support the generation of oscillatory motions. The computation of the characteristic time scale of these oscillatory motions is reviewed in this section.

We consider a stable density stratification, where light fluid is above a dense fluid. When a fluid particle is slightly vertically displaced, it feels a buoyancy restoring force acting in the opposite direction of the motion. The force acts as a spring, and therefore the fluid oscillates around the equilibrium position. These oscillations are known as internal gravity waves (hereafter, IGW). We consider a stably stratified fluid at rest with respect to a Galilean reference frame $(0, x, z)$, with z oriented upward. The density $\rho_0(z)$ decreases along the vertical axis, $\partial_z \rho_0(z) < 0$. Considering an incompressible fluid, a fluid particle vertically displaced δz from its initial position is subjected to two forces: the buoyancy force $\rho_0(z + \delta z)g$ and its weight $-\rho_0(z)g$. The Newton's equation of motion is expressed as

$$\rho_0(z) \frac{d^2 \delta z}{dt^2} = [\rho_0(z + \delta z) - \rho_0(z)]g. \quad (1.1)$$

Assuming small displacements δz of the fluid particle

$$\frac{d^2 \delta z}{dt^2} = \frac{\rho_0(z + \delta z) - \rho_0(z)}{\rho_0(z)} g = \frac{g}{\rho_0(z)} \frac{d\rho_0(z)}{dz} \delta z, \quad (1.2)$$

which can also be written as

$$\frac{d^2 \delta z}{dt^2} + N^2 \delta z = 0. \quad (1.3)$$

Equation 1.3 corresponds to equation of an harmonic oscillator with a natural frequency N , also called buoyancy frequency or Brunt-Väisälä frequency, which is expressed as

$$N^2 = -\frac{g}{\rho_0(z)} \frac{d\rho_0(z)}{dz}. \quad (1.4)$$

The value of N characterizes the stratification within a fluid. A perturbation in a stratified fluid within produces an oscillation with a characteristic frequency N . In the stratosphere, the N reaches values of order $N = 10^{-2}$ rad/s. In the ocean, the buoyancy frequency in the pycnocline is of order $N = 10^{-2}$ rad/s. In the abyssal region of the ocean, N decreases to values of order $N = 10^{-3}, 10^{-4}$ rad/s. Since the atmospheric and oceanic density profile is not constant, the value of N can vary notably with the vertical direction. In this PhD work and for simplicity reasons, I consider a linear density stratification, i.e. N is constant.

1.2.2 Linear internal gravity waves

The oscillatory perturbations that propagate in a stable stratified fluid are called internal gravity waves. They are observed in the atmosphere, at scales ranging from meters to kilometers (Staquet, Sommeria, 2002). The most common sources of internal waves are the wind blowing over topography, also called Lee waves (Wurtele et al., 1996), cumulus convective clouds and the sudden formation of turbulent patches by a dynamical instability. Internal gravity waves can be observed by cloud patterns (see figure 1.6). As the waves generate vertical motion of the air, the moisture in the air condenses into water.

Internal gravity waves in the ocean's interior have been reported since the beginning of the twentieth century as fluctuations of velocity and temperature, forming background

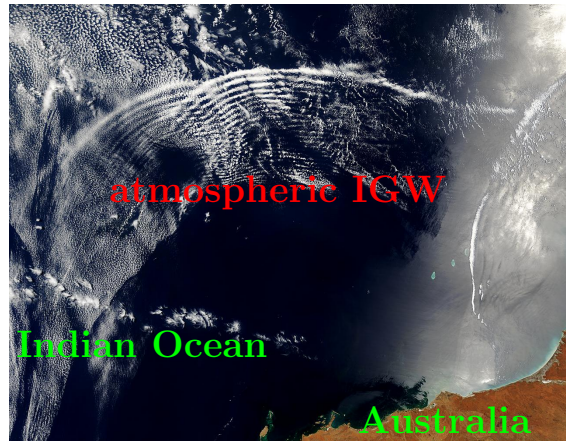


Figure 1.6: Atmospheric gravity waves ripple the surface of the Indian Ocean in front of the Australian coast. The internal waves are mirrored by wave clouds in the atmosphere. The image was taken by the Terra satellite on November 11, 2003. Image from NASA.

“noise,” which often dominates the mean currents. In some cases, the SAR (synthetic aperture radar), in being sensitive to the roughness of the sea surface, is able to provide “footprints” of oceanic internal waves (whose associated flow perturbs the sea surface). The main sources of internal wave generation in the ocean are the interaction of tides with topography and wind stress fluctuations (MacKinnon, 2013). As in the atmosphere, the displacement of a stratified fluid over topography generates waves at different frequencies depending on the size and shape of the topographies and on the velocity of the flow. The different types of internal gravity wave generation are summarized in Garrett (2003). The generation of internal waves due to tides passing through a topography has been widely studied experimentally (Gostiaux, Dauxois, 2007) and numerically (Nycander, 2005). These studies aim to estimate the energy transfer between tides and internal gravity waves, which is thought to be not negligible in the oceanic energy budget (Wunsch, Ferrari, 2004).

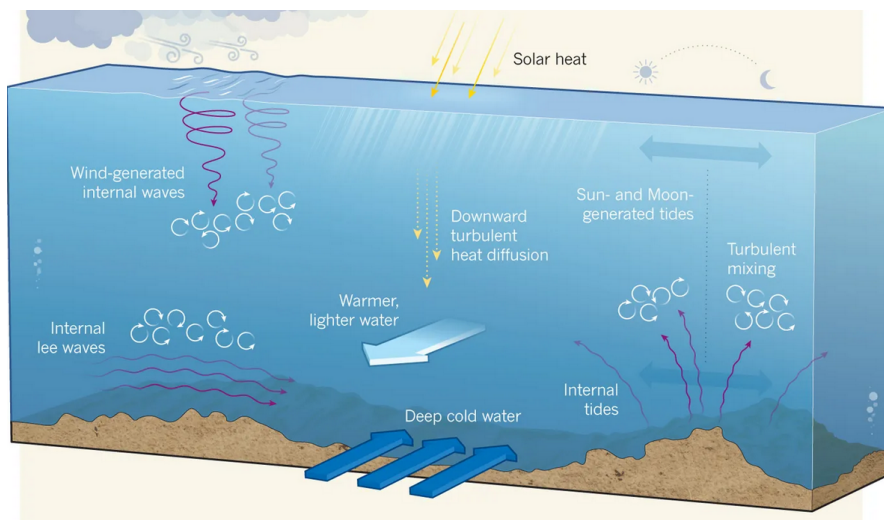


Figure 1.7: Schematic representation of the generation sources of internal gravity waves. There are three main mechanisms: tidal flow over steep or rough topography (lower right); fluctuating wind stress on the ocean surface (upper left); and quasi-steady flow over rough topography (lower left). Extracted from MacKinnon (2013)

Linear operator supports wave solutions

In this section, I describe under which conditions the internal gravity waves arise from the equation of motion. We consider the Navier-Stokes equations for a stratified fluid. The density of a fluid particle $\rho = \rho_0 + \bar{\rho} + \rho'$ can be expressed as the sum of a reference density ρ_0 , a density profile $\bar{\rho}$, and a density fluctuation ρ' . At this point, it is convenient to assume the Boussinesq approximation. It states that, under the condition that the density profile and density fluctuation are small in comparison to the reference density, $\bar{\rho} \ll \rho_0$ and $\rho' \ll \rho_0$ respectively, we can neglect the density fluctuation term in the equation of motion except where it appears with the gravity. The dynamics of an incompressible and stratified fluid is therefore described by the Navier-Stokes equations with the Boussinesq approximation as

$$\partial_t \mathbf{u} + \mathbf{u} \cdot \nabla \mathbf{u} = -\nabla p + b \mathbf{e}_z + \nu \nabla^2 \mathbf{u}, \quad (1.5)$$

$$\partial_t b + \mathbf{u} \cdot \nabla b = -N^2 u_z + \kappa \nabla^2 b, \quad (1.6)$$

$$\nabla \cdot \mathbf{u} = 0. \quad (1.7)$$

The velocity field is $\mathbf{u} = [u_x, u_y, u_z]$. The scalar pressure field is expressed as p . The buoyancy term is $b = (\rho'/\rho_0)g$, where ρ' is the density fluctuation. Molecular coefficients are ν and κ , respectively. N is the Brunt-Väisälä frequency. Here, we only consider the linear and non-viscous terms of the above equations. By doing so, we avoid the interaction among the scales of the flow. The linear system of equations (1.5) to (1.7) is

$$\partial_t \mathbf{u} = -\nabla p + b \mathbf{e}_z, \quad (1.8)$$

$$\partial_t b = -N^2 u_z, \quad (1.9)$$

$$\nabla \cdot \mathbf{u} = 0. \quad (1.10)$$

Applying the divergence operator in equation (1.8), we obtain

$$\partial_t(\nabla \cdot \mathbf{u}) = -\nabla^2 p + \partial_z b \Rightarrow \partial_z b = \nabla^2 p. \quad (1.11)$$

We apply the Laplacian operator to the z component of equation (1.8)

$$\partial_t(\nabla^2 u_z) = -\partial_z \nabla^2 p + \nabla^2 b = -\partial_{zz} b + \nabla^2 b = \partial_h b, \quad (1.12)$$

where the linear operator is $\partial_h = \partial_{xx} + \partial_{yy}$. We compute the time derivative, it gives

$$\partial_{tt}(\nabla^2 u_z) = -N^2 \partial_h u_z \Rightarrow \partial_t(\partial_h b) = -N^2 \partial_h u_z. \quad (1.13)$$

The linear system of equations can be written as

$$\partial_t(\nabla^2 u_z) = \partial_h b, \quad (1.14)$$

$$\partial_t(\partial_h b) = -N^2 \partial_h u_z. \quad (1.15)$$

Applying the time derivative to equation (1.14), we obtain

$$\partial_{tt}(\nabla^2 u_z) = -N^2 \partial_h u_z \quad (1.16)$$

The expression (1.16) is the wave equation of the linear internal gravity waves.

Anisotropic linear dispersion relation

The system of equations (1.8) to (1.10) accepts plane wave solutions such as

$$u_z = U_z e^{i(\mathbf{k} \cdot \mathbf{x} - \omega t)}, \quad (1.17)$$

$$b = B e^{i(\mathbf{k} \cdot \mathbf{x} - \omega t)}, \quad (1.18)$$

where \mathbf{k} is the wavevector and ω is the frequency. Applying the above wave plane solutions to the equation (1.16), we obtain the linear dispersion relation of the internal gravity waves

$$\omega^2 = N^2 \frac{k_h^2}{k_h^2 + k_z^2} = N \sin \theta, \quad (1.19)$$

where θ is the angle formed by the wavevector \mathbf{k} and the vertical axis (see figure 1.8). The frequency of internal gravity waves depends only on the direction of propagation and not on the wavelength and it ranges within $[0, N]$. The wavelength of the internal waves is imposed by the size of the forcing oscillation. The dispersion relation equation (1.19) contains the anisotropic character of the internal gravity waves. The phase and group velocities are, respectively,

$$\mathbf{c}_\psi = (\omega/k) \mathbf{e}_\mathbf{k}, \quad (1.20)$$

$$\mathbf{c}_g = (N/k) \cos \theta (\cos \theta \mathbf{e}_h - \sin \theta \mathbf{e}_z). \quad (1.21)$$

The phase velocity (parallel to the wavevector \mathbf{k}) is perpendicular to the group velocity $\mathbf{c}_\psi \perp \mathbf{c}_g$. Furthermore, the vertical component of the phase velocity is always opposite to the vertical component of the group velocity, as shown in figure 1.8. Waves that appear to propagate their phase upwards will be propagating their energy downwards and vice versa.

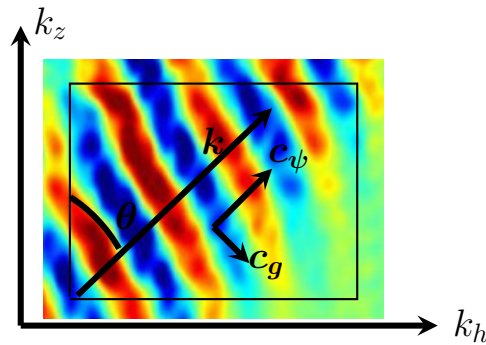


Figure 1.8: Schematic representation of the propagation of internal gravity waves. The phase and group velocities are perpendicular. The group velocity is parallel to the direction of propagation of the energy. Background field courtesy of L erisson, Chomaz and Ortiz (LadHyX, France)

Two different situations arise depending on the value of the angle θ (see figure 1.9). For low values of θ , internal waves have a low aspect ratio (small vertical scale and large horizontal scale). The phase propagates quasi-vertically with a low frequency $\omega \ll N$. The energy propagates quasi-horizontally, $\mathbf{c}_g \simeq (N/k) \mathbf{e}_x$. For large values of θ , we have internal waves with a large frequency $\omega \sim N$ and with large vertical scales and small horizontal scales. The energy propagates quasi-vertically $\mathbf{c}_g \sim (N/k)(\pi/2 - \theta) \mathbf{e}_z$. The internal gravity waves in the ocean and in the atmosphere correspond to the first type with a low aspect ratio (Garrett, Munk, 1979; Dewan et al., 1998; Lindborg, Brethouwer, 2007).

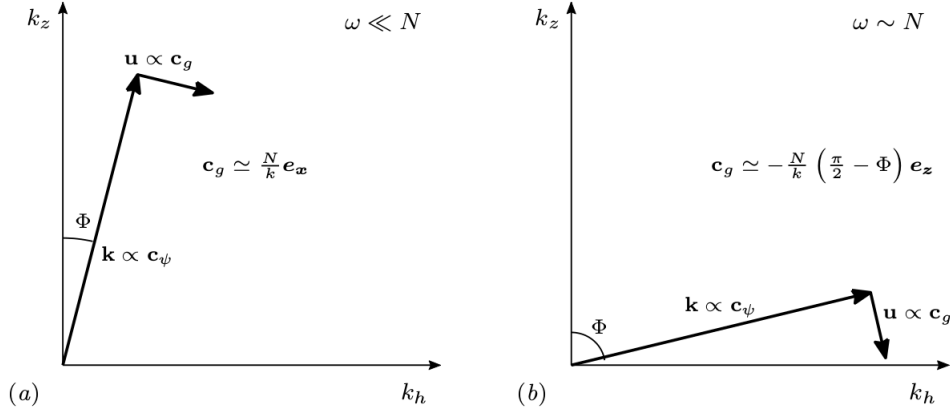


Figure 1.9: Schematic representation of two internal gravity waves: (a) wave with small frequency $\omega \ll N$. (b) wave with frequency $\omega \simeq N$. Schema extracted from (Augier, 2011).

Several non-dimensional quantities will be used in this PhD thesis in order to characterize the outcome dynamics. The first non-dimensional quantity is $F = \omega/N = \sin \theta$, which indicates the direction of propagation of internal gravity waves. The variation of the non-dimensional quantity F has been discussed in figure 1.9. Furthermore, shear instabilities and overturning might be developed in the flow. We use also a second non-dimensional parameter, the Richardson number, which compares locally the vertical shear of the velocity with the stratification and is expressed as

$$Ri = -(g/\rho_0)\partial_z\rho/|\partial_z\mathbf{u}_h|^2. \quad (1.22)$$

For $Ri < 0$, the flow is locally unstable by the gravitational instability since $\partial_z\rho_0 > 0$. For $0 < Ri < 1/4$, the flow might develop shear instabilities, also called Kelvin-Helmholtz (Miles, 1961). For $Ri > 1/4$, the flow is locally stable.

1.3 Ocean and atmosphere are turbulent flows

Atmosphere and oceans are turbulent in the sense that motions on wide range of scales, from few centimeters to thousand of kilometers, continuously cohabit and interact. They transfer energy from one scale to another scale until the energy is dissipated at small scales by the viscosity. For example, in the atmosphere, the flow is forced at scales of hundreds of kilometers (mesoscale eddies) and the dissipation acts on a scale of the order of centimeters. The mesoscales eddies are too large and fast to be affected by the dissipation. The non-dimensional number that quantifies the effect of the dissipation on the dynamics is the Reynolds number Re . It is defined as $Re = UL_h/\nu$, where U and L_h are the characteristic velocity and horizontal scale, respectively. ν is the kinematic viscosity. For large Re , the large-scale dynamics are weakly affected by the viscous dissipation. The forced hydrodynamic structures develop and transfer energy, by non-linear mechanisms (instabilities), among the scales. For instance, in homogeneous isotropic turbulence (HIT or classical turbulence), the energy is transferred from large to small scales. This transfer of energy, also called energy cascade, was first introduced by Richardson (1922). In the early forties, Kolmogorov predicted power laws for the energy cascade in homogeneous isotropic turbulence (HIT), $k^{-5/3}$ where k is the wavenumber, In this section I briefly introduce the notions of turbulence in the atmosphere and oceans. I discuss the energy repartition among the scales by means of the measured energy spectra (energy as function of a wavenumber k).

1.3.1 Atmospheric turbulence

Atmospheric turbulence is characterized by small scale and irregular air motions produced by winds that vary in speed and direction. Turbulence is important because it mixes and churns the atmosphere and causes water vapour, smoke, and other substances, as well as energy, to become distributed both vertically and horizontally. The atmospheric large-scales are weakly affected by the viscous dissipation, i.e. large Reynolds number Re . Large Re flows display a wide inertial range (scales weakly affected by the dissipation) in the energy spectra. If we consider a characteristic velocity and length scale $U \sim 10$ m/s and $L_h \sim 1000$ km, and a kinematic viscosity of the air $\nu \simeq 10^{-5}$ m²/s, a characteristic Reynolds number for the atmosphere is $Re \simeq 10^{12}$, meaning that a wide range on scales are weakly affected by the viscous dissipation.

Figure 1.10 represents the horizontal spectra (function of the horizontal wavenumber) of the zonal and meridional winds, and potential temperature near the tropopause from the Global Atmospheric Sampling Program aircraft data (Nastrom, Gage, 1985). At large scales ($L_h \geq 500$ km) the spectra follows the power law k^{-3} (see red line in figure 1.10). The dynamics is dominated by the geostrophic turbulence (pressure gradient of the equation (1.5) balanced by the Coriolis terms $f\mathbf{v}$) and is strongly affected by the stratification and Earth's rotation. One can observe a transition on the spectra from a power law k^{-3} to $k^{-5/3}$ at scales $L_h \simeq 500$ km. The $k^{-5/3}$ power-law is usually interpreted as classical 3D homogeneous and isotropic turbulence. However, the classical turbulence approach can not be used because large scales are still strongly affected by the stratification.

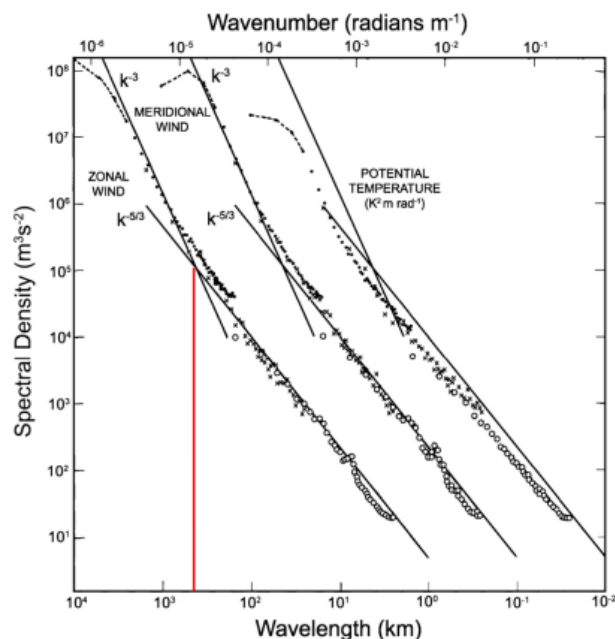


Figure 1.10: From left to right, horizontal spectra of zonal wind, meridional wind, and potential temperature near the tropopause. The spectra for meridional wind and temperature are shifted 1 and 2 decades to the right, respectively. The red vertical line displays the scale for which the transition appears. Reproduced from Nastrom, Gage (1985)

1.3.2 Ocean turbulence

Oceanic motions are forced by large-scale atmospheric winds and heat/freshwater fluxes. The first major transfer is from the large-scale currents to the mesoscale eddies (Thorpe, 2005; Zhang et al., 2014). The large-scale ocean currents are unstable and generate eddies with scales of 10 to 100 kilometers, also called mesoscale eddies. They interact and generate submesoscale turbulent filaments on scales from 10 kilometers to 100 meters. These motions are primarily horizontal constrained by the ocean stratification and rotation. Only at scales below approximately 100 meters, the turbulence is described as stratified microscale turbulence. In the ocean interior, microscale stratified turbulence develops when internal waves develop strong shears and overturn and break, much like surface gravity waves (Wunsch, Ferrari, 2004). These breaking events play a fundamental role in the ocean circulation because they carry energy and momentum to other regions of the ocean, enhancing mixing.

Two main motions cohabit together in the ocean: mesoscale eddies, and internal gravity waves. Mesoscale eddies are strongly affected by the rotation with a characteristic horizontal scale much larger than the vertical scale $L_x \gg L_z$. They have been observed by ocean buoys (Zhang et al., 2013) and satellites (Gaube et al., 2015). Furthermore, oceans support also the propagation of internal gravity waves. We have underlined that the main sources of internal wave generation are tides passing over the seafloor (Wunsch, Ferrari, 2004) and strong winds blowing over the sea surface (Dewan et al., 1998).

1.3.3 Ocean observations interpreted as a pure wave mechanism: the Garrett - Munk spectra

Despite the two main motions in the deep ocean (eddies and internal waves), the turbulent measurements are usually interpreted as the signature of a pure internal wave mechanism. Garrett, Munk (1975) presented an empirical model based on the superposition of internal gravity waves in order to explain a set of oceanic observations carried out in the 70's. The measurements used for the elaboration of the model were

- Moored spectra of the vertical displacement $F_\xi(\omega)$ based on Fofonoff (1969); Webster (1972).
- Towed spectra of the vertical displacement $F_\xi(k_x)$ based on Katz (1973).
- Dropped spectra of the vertical displacement $F_\xi(k_z)$ and of the current components $F_{u,v}(k_z)$ based on Sanford (1975).

The empirical model proposed by Garrett, Munk (1979) (Garrett and Munk spectrum) summarizes into one single energy spectrum $E(k_z, \omega)$ which scales as $E(k_z, \omega) \simeq N k_z^{-2} \omega^{-2}$, for frequencies $f < \omega < N$, where f is the Coriolis parameter, and large vertical wavenumbers k_z . Figure 1.11 displays the frequency and the vertical wavenumber spectra of the vertical displacement of the isotherms extracted from Cairns (1975) and Millard (1972), respectively. In figure 1.11 (a), we observe that the frequency spectrum displays a ω^{-2} power-law for frequencies lower than the buoyancy frequency. In figure 1.11 (b), the vertical wavenumber spectrum follows a k_z^{-2} power-law at large vertical scales. Both observations were used by Garrett, Munk (1975, 1979) to build the Garrett and Munk spectrum. More recent works have used the approach of wave turbulence to characterize the oceanic wavefield (Lvov et al., 2004; Polzin, Lvov, 2011). They proposed a spectral curve, which includes the Garrett and Munk spectrum, as a solution of the kinetic equation of a wavefield. These recent approaches will be discussed later in section 1.4.5. However ocean turbulent measurements are interpreted as a signature of only internal gravity waves, we have underlined the presence of vortical motions (eddies) interacting with the waves. In

this PhD work, we challenge the hypothesis that the ocean dynamics can be described as a pure wave mechanism. We attempt to answer the following question: are we able thereby to reproduce the wave energy spectrum model proposed by Garrett, Munk (1979) with a system only with oscillatory modes?

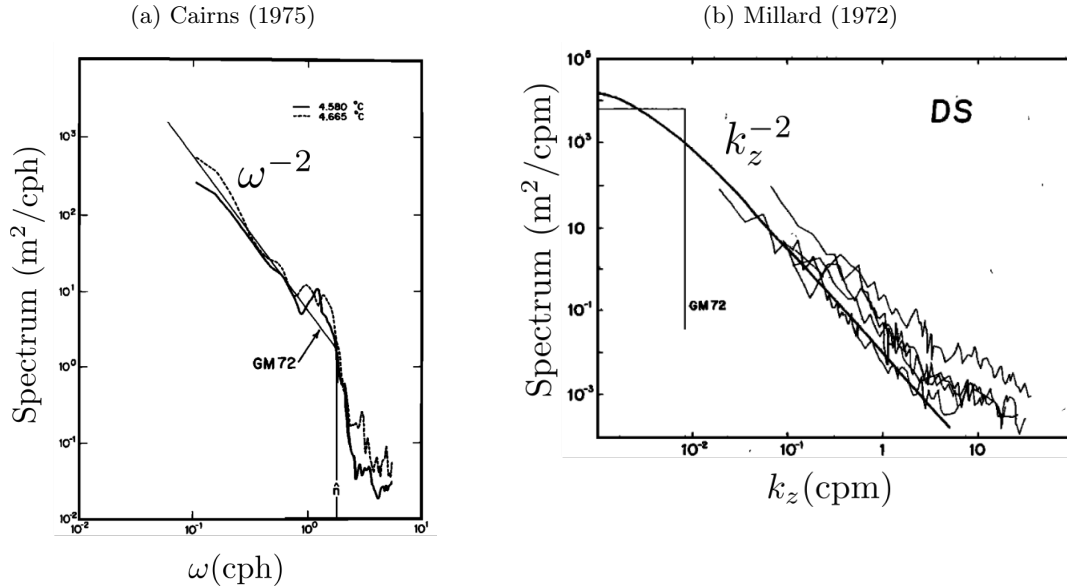


Figure 1.11: (a) Frequency spectra of the vertical displacement of the isotherms measured at $30^{\circ}20'N$, $121^{\circ}20'W$ on June 1973. The image has been extracted from Cairns (1975). (b) The dropped spectrum of the vertical displacement according to Millard (1972).

Stratified turbulence as an interpretation of oceanic observations

The energy spectra of the ocean is strongly anisotropic (Callies, Ferrari, 2013; Kunze, 2019), meaning that the horizontal and vertical energy spectra are different. This is due to the strongly anisotropy of their dynamics due to stratification and rotation effects. The anisotropy takes place mainly at large scales, whereas the small scales are mostly isotropic. This anisotropy on the large-scale dynamics, for different stratification strengths and different Reynolds numbers, will be discussed in chapter 4. Figure 1.12 displays schematically the anisotropic energy spectra observed in the ocean. The red and blue lines represent the horizontal and vertical energy spectra respectively. Both energy spectra are compensated by the power law $k^{-5/3}$. The horizontal wavenumbers are normalized by the Ozmidov wavenumber $k_o = (N^3/\epsilon)^{1/2}$, where N is the buoyancy frequency and ϵ is the mean energy dissipation rate. The vertical wavenumbers are normalized by the buoyancy wavenumber $k_b = N/U$. At large scales, the horizontal energy spectrum follows steepens as k_x^{-3} associated with a downscale enstrophy cascade of 2D turbulence. The large-scale structures contain a huge amount of energy. The dynamics are indeed quasi-geostrophic (QG turbulence) strongly influenced by the rotation. At smaller horizontal scales there is a transition of the energy spectrum, shallowing towards a $k_x^{-5/3}$ power-law as in classical turbulence (Cho, Lindborg, 2001). Nevertheless, it can not be considered as classical turbulence because, as it has been mentioned before, the large scales are still strongly affected by the stratification. We now focus on the vertical energy spectra (blue line). At large vertical space the spectrum follows k_z^{-2} before steepening with $N^2 k_z^{-3}$. The spectral break occurs at the buoyancy wavenumber $k_z/k_b \sim 1$. Small scales do not feel the effect of the stratification. The spectrum follows therefore the power law of classical turbulence

$k_z^{-5/3}$. Is part of this energy spectra a cascade of pure weakly interacting internal gravity waves?

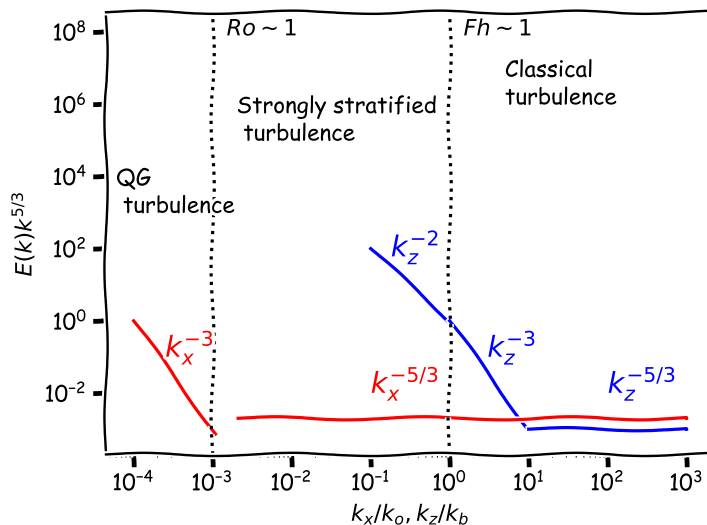


Figure 1.12: Schematic representation of the compensated energy spectra observed in the ocean. The red and blue lines represent, respectively, the horizontal and vertical components of the energy spectra. The horizontal wavenumbers are normalized by the Ozmidov wavenumber $k_o = (N^3/\varepsilon)^{1/2}$, where ε is the mean dissipation rate of energy. The vertical wavenumbers are normalized by the buoyancy wavenumber $k_b = N/U$.

1.4 Turbulence in stratified fluids

Geophysical flows such as the ocean and atmosphere are turbulent and stratified. Understanding their dynamics is crucial in the formulation of accurate parametrizations for climate and meteorological models. In the recent years, stratified turbulence has become an accurate interpretation of some geophysical observations (Riley, Lindborg, 2008). In this section, I review the stratified turbulence theory for 3D and 2D flows.

1.4.1 The Froude number in the strongly stratified turbulence regime

The Froude number is a non-dimensional parameter which represents the ratio between a characteristic buoyancy time scale and a characteristic inertial time scale. The horizontal and vertical Froude numbers are defined as

$$F_h = \frac{U}{L_h N} \quad F_v = \frac{U}{L_v N}, \quad (1.23)$$

where U is a horizontal characteristic velocity, L_h and L_v are the horizontal and vertical characteristic length scales and N is the buoyancy frequency. In the past, much of the work in stratified turbulence were based on the condition of small Froude number, $F_h \sim F_v \ll 1$. For instance, Riley et al. (1981) performed a scaling analysis of stratified turbulence under the condition of small Froude number ($F_h \sim F_v \ll 1$), and with no condition on the Reynolds number. The resulting flow was dominated by horizontally quasi-non-divergent motion with similarities with 2D dynamics. In a recent work, Billant, Chomaz (2001) performed a similarity analysis of the Boussinesq equations. They showed that the vertical Froude number is of order unity $F_v \sim 1$ in the limit of strongly stratified turbulence. This strongly non-linear regime is different to the classical $F_h \sim F_v \ll 1$ regime considered by

Riley et al. (1981). In the regime proposed by Riley et al. (1981), the horizontal layers are strongly coupled by dissipative effects with strong vertical gradients. The development of small vertical scales is not possible due to the dissipation. It prevents the flow to go towards $F_v \sim 1$. In this PhD work, we focus mainly on the strongly stratified regime ($F_h \ll 1$ and $F_v \sim 1$) due to its similarity with the regimes observed in nature.

1.4.2 Scaling analysis and the buoyancy Reynolds number

In the past, much of the work of stratified turbulence was focused on the condition of small vertical Froude number $F_v \ll 1$. Furthermore, we have underlined that these flows were indeed strongly affected by the dissipative effects and prevent the development towards regimes with $F_v \sim 1$. With the scaling analysis for inviscid fluids presented in Billant, Chomaz (2001), our understanding of the strongly stratified turbulent regime move towards the condition $F_v \sim 1$. Billant, Chomaz (2001) argued that dissipative effects can play an important role even at large Reynolds numbers due to the strong anisotropy of stratified flows. In this section, I review the scalings of 3D strongly stratified turbulence based on the scaling analysis performed by Godoy-Diana et al. (2004); Brethouwer et al. (2007).

We consider the Navier-Stokes equations with the Boussinesq approximation expressed with the equations (1.5) - (1.7) with a constant Brunt-Väisälä frequency N . Following the scalings of Brethouwer et al. (2007), the non-dimensional equations are expressed as

$$\frac{d\mathbf{u}_h}{dt} = -\nabla_h p + \frac{1}{Re\alpha^2}(\partial_{zz} + \alpha^2\nabla_h^2)\mathbf{u}_h, \quad (1.24)$$

$$F_h^2 \frac{du_z}{dt} = -\partial_z p + b + \frac{1}{Re\alpha^2}(\partial_{zz} + \alpha^2\nabla_h^2)u_z, \quad (1.25)$$

$$\frac{db}{dt} = -u_z + \frac{1}{ScRe\alpha^2}(\partial_{zz} + \alpha^2\nabla_h^2)b, \quad (1.26)$$

$$\nabla_h \cdot \mathbf{u}_h + \frac{F_h^2}{\alpha^2}\partial_z u_z = 0, \quad (1.27)$$

where the F_h is the horizontal Froude number, $Sc = \nu/\kappa$ is the Schmidt number, $\alpha = L_v/L_h$ is the aspect ratio and $d/dt = \partial_t + \mathbf{u}_h \cdot \nabla_h + (F_h/\alpha)^2 u_z \partial_z$. In the limit of $F_h \rightarrow 0$ and keeping the dominant terms, the set of equations become

$$(\partial_t + \mathbf{u}_h \cdot \nabla_h + \frac{F_h^2}{\alpha^2}u_z \partial_z)\mathbf{u}_h = -\nabla_h p + \frac{1}{Re\alpha^2}\partial_{zz}\mathbf{u}_h, \quad (1.28)$$

$$0 = -\partial_z p + b, \quad (1.29)$$

$$(\partial_t + \mathbf{u}_h \cdot \nabla_h + \frac{F_h^2}{\alpha^2}u_z \partial_z)b = -u_z + \frac{1}{Re\alpha^2}\partial_{zz}b, \quad (1.30)$$

$$\nabla_h \cdot \mathbf{u}_h + \frac{F_h^2}{\alpha^2}\partial_z u_z = 0. \quad (1.31)$$

We now compare the dissipative terms of the order $1/Re\alpha^2$ and the advective terms of the order F_h^2/α^2 . The ratio between these two quantities defines the buoyancy Reynolds number $\mathcal{R} = ReF_h^2$. The buoyancy Reynolds number can also be expressed as the ratio between two length scales $\mathcal{R} = (L_b/L_\nu)^2$, where $L_b = U/N$ is the buoyancy length scale and $L_\nu = \sqrt{\nu L_h/U}$ is the dissipative length scale of large scales. Depending on the value of \mathcal{R} , two regimes are defined in the strongly stratified limit (Brethouwer et al., 2007).

$\mathcal{R} \gg 1$: *strongly stratified turbulent regime*. The viscous and diffusive terms can be neglected compared to $\mathcal{O}(F_h^2/\alpha^2)$. The horizontal Froude number does not appear in the

equations becoming self-similar with respect to $z'N/U$, where z' is the vertical dimensional coordinate as shown in Billant, Chomaz (2001). This suggests the scaling $l_v \sim l_b \sim U/N$, where l_v is a characteristic vertical scale, and implies $\alpha \sim F_h$ and $F_v \sim 1$. Unlike the stratified regime proposed by Riley et al. (1981), the vertical advection terms contribute to the dynamics which are three-dimensional but strongly anisotropic. The scaling $l_v \sim U/N$ has been reported by simulations of stratified homogeneous turbulence (Godeferd, Staquet, 2003; Waite, Bartello, 2004). It was revealed through linear stability analysis of vortex pairs in stratified flows (Billant, Chomaz, 2000a). Experimental works of Park et al. (1994); Holford, Linden (1999) are consistent with this scaling.

$\mathcal{R} \ll 1$: *viscosity-affected stratified turbulent regime.* The vertical advection term is negligible compared to the viscous term. The vertical interaction between layers is therefore through vertical viscous shearing. Godoy-Diana et al. (2004) argued that the vertical length scale is determined by a balance between the horizontal advection term and the vertical diffusion term. This is fulfilled if $Re\alpha^2 \sim 1$ and it gives $l_v \sim L_\nu = \sqrt{\nu L_h/U}$. As it has been mentioned before, this scaling analysis was first performed by Riley et al. (1981) based on the condition of $F_h \sim F_v \ll 1$, and with no condition on the Reynolds number. In this kind of flows, the horizontal vortices dominate the dynamics with similarities to 2D dynamics. More recent works, such as Riley, Lelong (2000) among others, performed a similar scaling analysis in the limit of $F_v \ll 1$ with strong viscous effects. In the limit of $\mathcal{R} \ll 1$, the inertial cascade can not develop and the dissipation occurs predominately at large scales.

1.4.3 Coupling of the horizontal motions and internal waves

Stratified turbulent flows can be decomposed into vortical motion and internal gravity waves. In the past, theoretical studies decoupled these two dynamics (Riley et al., 1981; Lelong, Riley, 1991). For a small Froude number ($F_h \sim F_v \ll 1$), they stated that non-propagative motions (vortices) and fast propagative motions (waves) evolve over different time scales. At the lowest order, the equation of the vertical vorticity and the equation of the linear internal waves are indeed decoupled. The interactions among vortices and waves are described at higher order. A substantial amount of work has been done to describe the different types of interactions among waves and vortices (Bartello, 1995; Godeferd, Cambon, 1994). Billant, Chomaz (2001) performed a similarity analysis of the Boussinesq equations and confirmed that quasi-horizontal vortices and waves strongly interact in the strongly stratified turbulent regime. Their arguments were based on the existence of slow internal waves. In the limit of $F_h = 0$, the equations (1.24) - (1.25) contain quasi-horizontal motions and slow internal gravity waves with a frequency in the range $[0, N]$. Even if $N \gg UL_h$, there are slow internal waves with a frequency comparable to U/L_h (the corresponding dimensional vertical wavenumber $k_z = \mathcal{O}(N/U)$). The slow internal waves strongly interact with quasi-horizontal advective motions.

1.4.4 Direct energy cascade in strongly stratified turbulence

Mesoscale atmospheric spectra of the kinetic and potential energy display $k_h^{-5/3}$ and k_z^{-3} power-laws, respectively (Nastrom, Gage, 1985). Several works have been carried out with the aim to explain the observed energy spectra. In particular, Gage (1979); Lilly (1983) explained the power law $k_h^{-5/3}$ as a consequence of an inverse energy cascade (energy transfer from small to large scales) as in 2D turbulence. Herring, Métais (1989) performed numerical simulations and reported a weak inverse energy cascade. On the other hand, Dewan (1979, 1997) suggested the existence of a direct energy cascade generated by internal gravity waves. Lindborg (2006) proposed the strongly stratified turbulence approach to explain the anisotropy of the energy spectra. He assumed a forward energy cascade (energy transfer from large to small scales) along the horizontal direction, leading to the hypothesis proposed by Taylor (1935). He deduced that forward energy cascade is associated with the $k_h^{-5/3}$ and Nk_z^{-3} power laws. The horizontal kinetic and potential energy spectra of stratified turbulence are expressed as

$$E_K(k_h) = C_1 \varepsilon^{2/3} k_h^{-5/3}, \quad E_P(k_h) = C_2 \varepsilon k_h^{-5/3} / \varepsilon^{1/3}, \quad (1.32)$$

where ε and ε_P are the dissipation of the kinetic and potential energy, and C_1 and C_2 are the universal constants corresponding to Kolmogorov and the Obukhov-Corrsin of Kolmogorov turbulence. The hypothesis of Lindborg (2006) has been confirmed by later works of Brethouwer et al. (2007). They performed direct numerical simulations at larger resolution ($1024^2 \times 192$). The work concludes that the buoyancy Reynolds number $\mathcal{R} = ReF_h^2$ is the control parameter in stratified turbulence. In both numerical studies (Lindborg, 2006; Brethouwer et al., 2007), the forcing is restricted only to the horizontal vortical modes. These studies and among others (Maffioli et al., 2016) reported the apparition of the shear modes, which are modes with $k_h = 0$. A growth of energy in the shear modes is therefore interpreted as a tendency of the flow to form layers with a larger horizontal extent than the box (Lindborg, 2006). Recent studies in stratified turbulence use a vortical forcing concentrated in the vertically rotational modes with $k_z = 0$ in order to prevent the growth of the shear modes (Maffioli et al., 2016). The effects of the shear modes on the dynamics is discussed later in chapter 3.

1.4.5 Internal waves and stratified turbulence

Internal gravity waves are ubiquitous in nature. They contribute significantly to the dynamics of the ocean and atmosphere. They play an important role in the mixing of the ocean (Wunsch, Ferrari, 2004; Sutherland et al., 2019). The breaking of internal gravity waves allows the transfer of energy from large to small scales, where the energy is partly dissipated in heat and partly converted in potential energy through diapycnal mixing (Staquet, Sommeria, 2002). Recent numerical studies, such as Waite, Bartello (2006a), performed numerical simulations of forced internal gravity waves to explain the anisotropic spectra of the ocean $E(k_z) \sim N^2 k_z^{-3}$. They did not reproduce the spectra. Their energy spectra was shallower than k_z^{-3} , although they steepened towards it with increasing stratification and as long as wave breaking was resolved.

The anisotropic energy spectra of the atmosphere and ocean is observed in the presence of a variety of wave sources. It is therefore reasonable to seek an interpretation in terms of a local statistical steady state resulting from complex wave interactions (Staquet, Sommeria, 2002). Different approaches came up involving complex interactions between internal waves. Weak wave turbulence is a theoretical approach based on the non-linear interaction among small amplitude waves. The study of weakly interacting internal gravity waves was first proposed by Hasselmann (1966, 1967) and reviewed by Müller et al. (1986). In these first works, Hasselmann (1966) used only lagrangian variables implying

only wave-wave interactions. In more recent works Caillol, Zeitlin (2000) used Eulerian variables in their study, allowing the interactions with the vortex modes. Lelong, Riley (1991); Godeferd, Cambon (1994) conclude that waves-vortical mode interactions are more efficient at transferring energy than three-wave interactions. The Parametric Subharmonic Instability (PSI) is a class of resonant wave-wave interaction, which transfers the energy of a primary wave to two secondary waves with a frequency near the half of the primary frequency (Bourget et al., 2013). A detailed review of resonant interactions among the internal waves is presented in Dauxois et al. (2018). Finally, the work of Lvov et al. (2004) show that wave turbulence formalism captures much of the variability apparent in the oceanic wave field. In their work, they perform a characterization of the spectral curve, which includes the Garrett-Munk spectrum, as an exact steady solution to a kinetic equation for the evolution of the wave field. A detailed review about the characterization of the oceanic wavefield can be found in Polzin, Lvov (2011). However, the weak wave turbulence approach is questionable because the oceanic internal wave field is too energetic to be considered as an assemblage of weakly interacting waves (Holloway, 1980; Lindborg, Riley, 2007). Analogously to the ocean, recent studies on atmospheric mesoscale dynamics affirm that the weakly nonlinear wave theory cannot provide an explanation of the energy spectra in the upper troposphere and lower stratosphere (Li, Lindborg, 2018).

1.5 Problem statement

We have underlined that the ocean dynamics is composed of vortical motions (eddies) and internal gravity waves. Despite of these two motions, the ocean observations are usually interpreted as the signature of pure internal wave mechanism. Garrett, Munk (1975) proposed an empirical model based on an internal wave spectra to explain oceanic measurements without explaining the energy distribution among these waves. The first problem statement is: are we able to reproduce the empirical model proposed by Garrett, Munk (1975) with a system only with wave modes?

In the recent years, stratified turbulence has become a powerful approach to describe some geophysical turbulence measurements (Riley, Lindborg, 2008). Several attempts have been carried out to explain the anisotropy of the energy spectra observed in nature. Lindborg (2006) obtained an anisotropic energy spectra, with power laws $k_x^{-5/3}$ and k_z^{-3} , associated with a downscale energy cascade. The hypothesis of a downscale energy cascade proposed by Lindborg (2006) was later confirmed by Brethouwer et al. (2007). In the strongly stratified turbulence regime, quasi-horizontal vortical motions and internal waves strongly interact as derived in Billant, Chomaz (2001). Past works such as Lelong, Riley (1991); Godeferd, Cambon (1994) concluded that vortical-wave interactions are very efficient at transferring energy. More recent approaches, based on weak wave turbulence, attempt to describe the oceanic wavefield (Polzin, Lvov, 2011). The second problem statement is: are we able to generate turbulence driven by weakly non-linear internal gravity waves?

2D stratified turbulence: towards a pure wave system

The easiest way to obtain a system only with wave modes is to reduce the dimensions of the system from 3D to 2D. By considering a vertical section of a stratified flow, we prevent motions perpendicular to the plane. We get rid of the horizontal vortical modes represented by the vertical vorticity $\omega_z = 0$. The 2D stratified turbulence dynamics supports therefore only wave modes and shear modes. We remove the shear modes in all our simulations, implying only wave-wave interactions. Furthermore, a 2D configuration allows us to perform longer numerical simulations with a considerable lower computational cost than the 3D DNS. In the strongly stratified regime $\{F_h \ll 1, \mathcal{R} \geq 1\}$, the characteristic linear time (wave period) is significantly smaller than the characteristic non-linear time. Hence, a large number of time steps is needed before the non-linearity operates. For this reason, 2D DNS allows us to perform long numerical simulations of strongly stratified turbulent regimes.

The two main studies in 2D stratified turbulence were carried out by Boffetta et al. (2011); Kumar et al. (2017). Firstly, Boffetta et al. (2011) investigates numerically the phenomenology of the energy transfer in two-dimensional weakly stratified turbulence. They perform numerical simulations with an isotropic forcing at scales smaller than the Ozmidov scale $l_f < l_o < l_{box}$. The isotropic forcing excites all modes for a given $|\mathbf{k}_f|$, where \mathbf{k}_f is the forcing wavenumber. The forcing term appears only at the momentum equations, i.e. only kinetic energy is injected. This kinetic energy is transferred from the injection scale to large scales. This inverse cascade proceeds up to the Ozmidov scale l_o , where the effects of buoyancy are important. Kinetic energy is therefore converted to potential energy, which is transferred towards small scales following a forward cascade of energy. Boffetta et al. (2011) called flux loop to this novel energy transfer mechanism. Despite the absence of large-scale dissipation, it produces statistically stationary states in 2D turbulence. On the other hand, Kumar et al. (2017) carried out a numerical study of 2D stratified turbulence for different strengths of the stratification. They use a large-scale isotropic and random forcing. For strong stratifications, they observe the coexistence between large-scale vertically sheared horizontal flow and small scale turbulence. Both kinetic and potential energy spectra display a k^{-3} power-law associated with a direct energy cascade. They affirm that these large horizontal scales correspond to large-scale internal gravity waves.

Both numerical works use an isotropic forcing which implies the excitation of modes with all possible frequencies in the range $[0, N]$. This forcing scheme does not correspond with the forcing observed in nature. Internal waves are generated mainly by tides passing over a topography. These waves have one characteristic frequency given by the period of the tide. Furthermore, they inject energy only into the momentum equation. In this PhD work, we use a localized forcing scheme allowing us to force modes with the same frequency. We inject energy into both, momentum and buoyancy equations, allowing us to force only waves propagating towards one direction, also called prograde waves. The numerical study of Kumar et al. (2017) analyzes the energy spectra without decoupling the horizontal and vertical components. We have underlined that strongly stratified turbulence is anisotropic. It is therefore important to analyze the horizontal and vertical energy spectra to capture this anisotropy. Finally, the work of Boffetta et al. (2011) does not explain which non-dimensional parameters are relevant for 2D stratified turbulence. In this PhD work, we perform a scaling analysis of the 2D Navier-Stokes equations with the Boussinesq approximation and with hyper-viscosity coefficient. We present the different regimes of 2D stratified turbulence depending on the value of the non-dimensional parameters.

1.6 Objectives of this thesis

Several scientific issues have been raised along this introductory chapter:

- We have mentioned that the observed oceanic energy spectra is usually interpreted as the signature of only internal gravity waves (Garrett, Munk, 1975, 1979). We want therefore to check if we are able to reproduce the observed energy spectra with a system only with wave modes. The easiest way to have only wave modes is to reduce the system to a 2D configuration. Furthermore, we seek for a forcing quantity that allows us to force waves propagating towards one direction (prograde waves). This quantity is the eigenmode of the 2D Navier-Stokes equations with the Boussinesq approximation. The computation of the eigenmodes is presented in the first part of the chapter 2.
- We have underlined that geophysical flows have a large Reynolds number. They have a wide range of scales weakly affected by the viscosity before attaining the dissipative scale. In numerical simulations, two parameters control the dissipation, the numerical resolution and the viscosity coefficient. For a fixed numerical resolution, one can use the Navier-Stokes viscosity coefficient ν or an hyper-viscosity coefficient ν_m , where m is the hyper-viscosity order. The hyper-viscosity allows us to have a larger portion of the grid points assigned to the inertial range, than the Navier-Stokes viscosity. We use therefore the hyper-viscosity in all our simulations. No scaling analysis with the Navier-Stokes equations of a stratified fluid with an hyper-viscosity coefficient ν_m has been found in the bibliography. Based on the work of Brethouwer et al. (2007), a scaling analysis of the 2D Navier-Stokes equations with the Boussinesq approximation and with an hyper-viscosity coefficient ν_m is presented in the second part of the chapter 2.
- The numerical studies of 2D stratified turbulence reported in (Boffetta et al., 2011; Kumar et al., 2017) used a forcing scheme which excites modes with all frequencies in the range $[0, N]$. This type of forcing does not correspond with the forcing observed in nature. Internal waves in the ocean are mainly excited by tides passing over a topography. The time scale of the forced internal waves is similar to the period of the tides. In chapter 3, a new forcing scheme is presented, which injects energy into a localized region of the spectral space allowing us to force modes with similar characteristic time scale.
- We have seen that the horizontal Froude number F_h and the buoyancy Reynolds number \mathcal{R} control the dynamics of 3D stratified flows. However, an accurate phenomenology of 2D stratified turbulence with an hyper-viscosity coefficient has never been reported depending on the value of the non-dimensional parameters $\{F_h, \mathcal{R}\}$. In chapter 4, we perform direct numerical simulations for different stratification strengths and different Reynolds numbers. Three different regimes are finally presented in the parameter space $\{F_h, \mathcal{R}\}$
- Several numerical works involving internal waves reported internal waves at large horizontal scales in strongly stratified turbulent regime (Waite, Bartello, 2006a; Lindborg, Brethouwer, 2007). In chapter 5, an spatio-temporal analysis is carried out in order to identify the presence of internal gravity waves and to identify the modes where waves are more likely to develop.
- Similar studies on strongly stratified turbulence forcing different quantities have been performed in order to study the degree universality of the energy spectra (Waite, Bartello, 2004, 2006a). In chapter 6, we analyze the effects of the forcing on 2D

stratified turbulence. We perform numerical simulations forced on two different quantities: (i) the vorticity; and (ii) the linear mode of the 2D Navier-Stokes linear operator. Moreover, we study how the energy is distributed among the modes in the transient states.

Chapter 2

Theory of two-dimensional stratified turbulence

In this PhD work, we study 2D stratified turbulence dynamics by means of direct numerical simulations. We force the eigenmodes of the linear 2D Navier-Stokes equations with the Boussinesq approximation. We excite internal gravity waves propagating with the same direction as the wavevector \mathbf{k} , which is a simulation parameter. In the first part of this chapter, I review the notions of the Fourier transform of a real signal. This tool is useful for the computation of the linear eigenmodes of the 2D Navier-Stokes equations. In the second part, a scaling analysis on the 2D Navier-Stokes equations with an hyper-viscosity coefficient is performed based on the work of Brethouwer et al. (2007). Three different regimes can be identified: weakly stratified regime, strongly stratified turbulent regime and strongly stratified viscosity-affected regime. The resulting scaling laws from this analysis will be tested later in chapter 4.

2.1 Spectral description: the Fourier transform

In this section, we introduce the definition of the Fourier transform of a real signal, such as the horizontal velocity $u_x(\mathbf{x})$. We first consider a 1D space and periodic in the interval $[0, L_x]$. The 1D Fourier transform of the signal $u_x(x)$ can be thus expressed as

$$\hat{u}_x(k_x) = \frac{1}{L_x} \int_0^{L_x} u_x(x) e^{-ik_x x} dx. \quad (2.1)$$

In a numerical study, the wavenumber k_x is limited by the spatial resolution of the simulation. If we consider n_x the number of grid points, the maximum wavenumber is $k_{\max} = \pi n_x / L_x$. From the Fourier transform of a signal, one can compute the averaged energy of the signal E_f through the Parseval's theorem, which is expressed as

$$E_f = \langle u_x^2 / 2 \rangle = \frac{1}{2} \frac{1}{L_x} \int_0^{L_x} u_x(x)^2 dx = \sum_{k_x} |\hat{u}_x(k_x)|^2 / 2. \quad (2.2)$$

One can extend the expression (2.1) to a higher dimension space. We consider a physical space periodic in the intervals $[0, L_x]$ and $[0, L_z]$, respectively. The 2D Fourier transform of the horizontal velocity is thus expressed as

$$\hat{u}_x(\mathbf{k}) = \frac{1}{L_x L_z} \int_0^{L_x} \int_0^{L_z} u_x e^{-i\mathbf{k} \cdot \mathbf{x}} dx dz. \quad (2.3)$$

It is important to notice that the Fourier transform requires a periodic signal. It is easy to satisfy this condition when using a periodic spatial domain. All simulations presented in this manuscript are periodic in both directions. However, signals are usually not periodic in time. We use a window function to overcome this issue.

2.2 Eigenmodes of the linear 2D Navier-Stokes equations

We have underlined in section 1.3.2 that the energy transfer in the ocean is assumed to be a pure internal wave mechanism (Garrett, Munk, 1979). One of the goals of this PhD work is to check this argument by considering a system only with wave modes. We reduce thus the system from 3D to 2D configuration. The 2D system only contains wave modes and shear modes. We get rid of the shear modes. As it has been mentioned above, we are interested in forcing internal gravity waves propagating with the same direction as the wavevector \mathbf{k} . We remind that the wavevector \mathbf{k} is a simulation parameter. In order to force these coherent internal gravity waves, one needs to inject energy directly into the eigenmodes of the 2D Navier-Stokes equations.

We consider a two-dimensional domain with x - and z -directions, where the direction of gravity follows the z -wise direction. The unitary vectors are \mathbf{e}_x and \mathbf{e}_z , respectively. The velocity vector can be expressed as $\mathbf{u} = u_x \mathbf{e}_x + u_z \mathbf{e}_z$. The direction of gravity is the z -wise direction. We consider a linear density stratification characterized by the buoyancy frequency N . Neglecting the non-linear and diffusive terms, the 2D Navier-Stokes equations with the Boussinesq approximation are expressed as

$$\partial_t \mathbf{u} = -\nabla p + b \mathbf{e}_z, \quad (2.4)$$

$$\partial_t b = -N^2 u_z, \quad (2.5)$$

$$\nabla \cdot \mathbf{u} = 0. \quad (2.6)$$

Equations (2.4) and (2.5) are the time evolution of momentum and buoyancy respectively. Equation (2.6) represents the condition for an incompressible flow. Manipulating the above equations we obtain

$$\partial_t (\nabla^2 u_z) = \partial_{xx} b, \quad (2.7)$$

$$\partial_t (\partial_{xx} b) = -N^2 \partial_{xx} u_z. \quad (2.8)$$

The time evolution of the equation (2.7) and (2.8) in the spectral space is

$$\partial_t (k^2 \hat{u}_z) = k_x^2 \hat{b}, \quad (2.9)$$

$$\partial_t \hat{b} = -N^2 \hat{u}_z, \quad (2.10)$$

where \hat{u}_z and \hat{b} are the spatial Fourier transform of the vertical velocity and buoyancy, respectively.

Computation of the linear dispersion relation

At this point, one can compute the linear dispersion relation of internal gravity waves. Applying the time derivative to the equation (2.9), one obtains

$$\partial_{tt} (k^2 \hat{u}_z) = k_x^2 \partial_t \hat{b}. \quad (2.11)$$

We apply now the time evolution of the buoyancy given in (2.10) into the equation (2.11), which is expressed as

$$\partial_{tt} (k^2 \hat{u}_z) = -k_x^2 N^2 \partial_{tt} \hat{u}_z. \quad (2.12)$$

The Fourier transform of the time derivative operator is $\partial_{tt} = i^2\omega = -\omega$. The equation (2.12) is expressed as

$$\omega^2 = N^2 \frac{k_x^2}{\mathbf{k}^2}, \quad (2.13)$$

which is the linear dispersion relation of internal gravity waves. It gives a relation between the frequency of the wave and its direction of propagation.

Computation of eigenvalues and eigenmodes.

We consider a new variable \hat{u}'_z , such that $\hat{u}'_z = N^2 \hat{u}_z$, the above system of equations becomes

$$\tilde{\partial}_t(\hat{u}'_z) = \omega_k^2 \hat{b}, \quad (2.14)$$

$$\tilde{\partial}_t \hat{b} = -\hat{u}'_z. \quad (2.15)$$

We consider the variables \hat{u}_z and \hat{b} plane wave solutions. Hence, we can express them as

$$u_z(\mathbf{x}, t) = \hat{U}_z e^{i(\mathbf{k}\mathbf{x} - \omega t)}, \quad (2.16)$$

$$b(\mathbf{x}, t) = \hat{B} e^{i(\mathbf{k}\mathbf{x} - \omega t)}, \quad (2.17)$$

where \hat{U}_z and \hat{B} are the amplitudes of the wave. The phase $\mathbf{k}\mathbf{x} - \omega t$ propagates in the same direction as the wavevector \mathbf{k} when $\omega > 0$. Analogously, the phase propagates in the opposite direction as the wavevector \mathbf{k} when $\omega < 0$. We can see that $-i\omega$ is an eigenvalue of the time derivative operator as

$$\tilde{\partial}_t \hat{u}'_z = -i\omega \hat{u}'_z,$$

$$\tilde{\partial}_t \hat{b} = -i\omega \hat{b}.$$

The equations (2.14) and (2.15) can be written in a matrix form

$$\tilde{\partial}_t \begin{bmatrix} \hat{u}'_z \\ \hat{b} \end{bmatrix} = \begin{bmatrix} 0 & \omega_k^2 \\ -1 & 0 \end{bmatrix} \begin{bmatrix} \hat{u}'_z \\ \hat{b} \end{bmatrix}, \quad (2.18)$$

$$\partial_t V = JV = \lambda V, \quad (2.19)$$

where λ is an eigenvalue of the operator J . To find the eigenvalues of the operator we need to solve the equation $|J - \lambda \mathcal{I}| = 0$ as

$$\begin{vmatrix} -\lambda & \omega_k^2 \\ -1 & -\lambda \end{vmatrix} = 0. \quad (2.20)$$

The two eigenvalues of the system are $\lambda_{\pm} = \mp i\omega_k$. They are given by the linear dispersion relation of the internal gravity waves. The eigenmodes are a linear combination of the variables of the system $\hat{a}_{\pm} = A\hat{u}'_z + B_{\pm}\hat{b}$, where A and B_{\pm} are constants. We choose a constant $A = 1$. We compute the constant B_{\pm} as

$$\tilde{\partial}_t \hat{a}_{\pm} = \mp i\omega_k \hat{a}_{\pm} = \mp i\omega_k \hat{u}'_z \mp i\omega_k B_{\pm} \hat{b}, \quad (2.21)$$

$$\tilde{\partial}_t \hat{a}_{\pm} = \tilde{\partial}_t \hat{u}'_z \pm B_{\pm} \tilde{\partial}_t \hat{b} = \omega_k^2 \hat{b} \mp B_{\pm} \hat{u}'_z. \quad (2.22)$$

By the identification of the equations (2.21) and (2.22), we obtain

$$\hat{b}(\omega_k^2 \pm i\omega_k B_{\pm}) = (\pm i\omega_k \mp B_{\pm}) \hat{u}'_z. \quad (2.23)$$

The above expression needs to be true for all values of \hat{b} and \hat{u}'_z , thus $(\omega_k^2 \pm i\omega_k B_{\pm}) = 0$ and $(\pm i\omega_k \mp B_{\pm}) = 0$. We obtain $B_{\pm} = \pm i\omega_k$. The eigenmode \hat{a}_{\pm} can be written as

$$\hat{a}_{\pm} = N^2 \hat{u}_z \pm i\omega_k \hat{b}. \quad (2.24)$$

One can observe that the eigenmodes \hat{a}_\pm are a linear combination of the vertical velocity \hat{u}_z and the buoyancy \hat{b} . The horizontal velocity \hat{u}_x does not appear in the expression of the eigenmodes. The horizontal velocity \hat{u}_x is indeed coupled to the vertical velocity through the continuity equation $k_x \hat{u}_x + k_z \hat{u}_z = 0$. Furthermore, the direction of propagation of the forced internal gravity waves depends whether we force the positive part of the linear mode $\hat{a}_+ = N^2 \hat{u}_z + i\omega_k \hat{b}$ or the negative part of the linear mode $\hat{a}_- = N^2 \hat{u}_z - i\omega_k \hat{b}$. The positive part of the linear mode excites waves propagating with the same direction as the wavevector \mathbf{k} (prograde waves). The negative part of the linear mode forces waves propagating with the opposite direction as the wavevector \mathbf{k} (retrograde waves). All simulations in chapter 4 are forced on the positive component of the linear modes \hat{a}_+ . At this point, we can compute back the physical variables from the equation (2.24). The vertical velocity \hat{u}_z and buoyancy \hat{b} are expressed as

$$\hat{u}_z = \frac{1}{2N^2}[\hat{a}_+ + \hat{a}_-], \quad (2.25)$$

$$\hat{b} = \frac{1}{2i\omega_k}[\hat{a}_+ - \hat{a}_-]. \quad (2.26)$$

2.3 Scaling analysis of 2D stratified turbulence with an hyper-viscosity coefficient ν_n

Similar to the analysis carried out by Brethouwer et al. (2007) for the 3D case, I performed a scaling analysis of the 2D Navier-Stokes equations with the Boussinesq approximation and for a generalized hyper-viscosity and hyper-diffusivity terms of order n . The resulting non-dimensional quantities, such as the Reynolds number and buoyancy Reynolds number, depend on the order of the hyper-viscosity and -diffusivity terms. Nevertheless, all simulations presented in this manuscript are computed with $n = 8$.

Governing equations

The two-dimensional equations of motion of a stratified, incompressible flow under the Boussinesq approximation are

$$\frac{\partial u'_x}{\partial t'} + u'_x \frac{\partial u'_x}{\partial x'} + u'_z \frac{\partial u'_x}{\partial z'} = -\frac{\partial p'}{\partial x'} + \nu_n \left(\frac{\partial^n u'_x}{\partial x'^n} + \frac{\partial^n u'_x}{\partial z'^n} \right) \quad (2.27)$$

$$\frac{\partial u'_z}{\partial t'} + u'_x \frac{\partial u'_z}{\partial x'} + u'_z \frac{\partial u'_z}{\partial z'} = -\frac{\partial p'}{\partial z'} + b + \nu_n \left(\frac{\partial^n u'_z}{\partial x'^n} + \frac{\partial^n u'_z}{\partial z'^n} \right), \quad (2.28)$$

$$\frac{\partial b'}{\partial t'} + u'_x \frac{\partial b'}{\partial x'} + u'_z \frac{\partial b'}{\partial z'} = -N^2 u'_z + \kappa_n \left(\frac{\partial^n b'}{\partial x'^n} + \frac{\partial^n b'}{\partial z'^n} \right), \quad (2.29)$$

$$\frac{\partial u'_x}{\partial x'} + \frac{\partial u'_z}{\partial z'} = 0, \quad (2.30)$$

where u'_x is the horizontal velocity, u'_z is the vertical velocity, p' is the pressure, $\rho_0 = \langle \bar{\rho}(z) \rangle$ is the average density and $\bar{\rho}(z)$ is the linear density profile, ν_n and κ_n are the hyper-viscosity and hyper-diffusivity terms of order n . The buoyancy is defined as $b = -g\rho'/\rho_0$, where ρ' is the fluctuation of density from the linear density profile $\bar{\rho}(z)$, and g is the acceleration of gravity. The Brunt-Väisälä frequency is expressed as $N = \sqrt{-(g/\rho_0)\partial\bar{\rho}/\partial z'}$.

Scaling of the equations

For a characteristic horizontal velocity and length scale U_x and l_x , we can introduce the horizontal Froude number $F_h = U_x/(l_x N)$ and the aspect ratio $\alpha = l_z/l_x$, where l_z is the vertical length scale. Equating the inertial terms with the pressure gradient in the horizontal momentum equation (2.27) gives a characteristic pressure $p' \sim U_x^2$. Since $F_h \ll 1$, the only way to balance the vertical pressure gradient is by density perturbations through hydrostatic equilibrium (Billant, Chomaz, 2001). The buoyancy scales therefore as $b' \sim U_x^2/l_z$ and the horizontal advection of buoyancy scales as $N^2 U_z$. Hence, the characteristic vertical velocity is $U_z \sim U_x^3/(N^2 l_x l_z)$. With these characteristic length scales we define unprimed dimensionless variables

$$\begin{aligned} u'_x &= U_x u_x & u'_z &= \frac{U_x^3}{N^2 l_x l_z} u_z & b' &= \frac{U_x^2}{l_z} b & p' &= U_x^2 p, \\ x' &= l_x x & z' &= l_z z & t' &= \frac{l_x}{U_x} t, \end{aligned}$$

and we obtain the dimensionless system

$$\frac{\partial u_x}{\partial t} + u_x \frac{\partial u_x}{\partial x} + \frac{F_h^2}{\alpha^2} u_z \frac{\partial u_x}{\partial z} = -\frac{\partial p}{\partial x} + \frac{1}{Re_n} \left[\frac{\partial^n u_x}{\partial x^n} + \frac{1}{\alpha^n} \frac{\partial^n u_x}{\partial z^n} \right], \quad (2.31)$$

$$F_h^2 \left[\frac{\partial u_z}{\partial t} + u_x \frac{\partial u_z}{\partial x} + \frac{F_h^2}{\alpha^2} u_z \frac{\partial u_z}{\partial z} \right] = -\frac{\partial p}{\partial z} + b + \frac{F_h^2}{Re_n} \left[\frac{\partial^n u_z}{\partial x^n} + \frac{1}{\alpha^n} \frac{\partial^n u_z}{\partial z^n} \right], \quad (2.32)$$

$$\frac{\partial b}{\partial t} + u_x \frac{\partial b}{\partial x} + \frac{F_h^2}{\alpha^2} u_z \frac{\partial b}{\partial z} = -u_z + \frac{1}{Re_n Sc_n} \left[\frac{\partial^n b}{\partial x^n} + \frac{1}{\alpha^n} \frac{\partial^n b}{\partial z^n} \right], \quad (2.33)$$

$$\frac{\partial u_x}{\partial x} + \frac{F_h^2}{\alpha^2} \frac{\partial u_z}{\partial z} = 0, \quad (2.34)$$

where the generalized Reynolds number is $Re_n = U_x l_n^{n-1} / \nu_n$ and the generalized Schmidt number is $Sc_n = \nu_n / \kappa_n$. One can identify three different regimes depending on the value of the horizontal Froude number F_h and the generalized Reynolds number Re_n : weakly stratified flows ($F_h \sim 1$ and large Re_n), viscosity-affected strongly stratified flows ($F_h \rightarrow 0$ and low Re_n), and strongly stratified turbulence ($F_h \rightarrow 0$ and large Re_n). Geophysical flows such as the atmosphere and oceans belong to the strongly stratified turbulence regime, $F_h \rightarrow 0$ and large Re (see figure 18 of Brethouwer et al. (2007)).

2.3.1 Weakly stratified flows $F_h \sim 1$

In the limit of weak stratification, the dynamics are isotropic, i.e. $\alpha \sim 1$, $F_h \sim 1$ and $Re_n \gg 1$. The dimensionless equations can be simplified in:

$$\frac{\partial u_x}{\partial t} + u_x \frac{\partial u_x}{\partial x} + u_z \frac{\partial u_x}{\partial z} = -\frac{\partial p}{\partial x}, \quad (2.35)$$

$$\frac{\partial u_z}{\partial t} + u_x \frac{\partial u_z}{\partial x} + u_z \frac{\partial u_z}{\partial z} = -\frac{\partial p}{\partial z} + b, \quad (2.36)$$

$$\frac{\partial b}{\partial t} + u_x \frac{\partial b}{\partial x} + u_z \frac{\partial b}{\partial z} = -u_z, \quad (2.37)$$

$$\frac{\partial u_x}{\partial x} + \frac{\partial u_z}{\partial z} = 0, \quad (2.38)$$

representing the motion of an active scalar (buoyancy) advected by the flow. The scalar fields in 2D turbulence have been largely studied theoretically (Moffatt, 1999; Celani et al., 2010) and numerically (Celani et al., 2004; Lapeyre et al., 1999).

2.3.2 Strongly stratified flows $F_h \rightarrow 0$

In the limit of strong stratification, i.e. $F_h \rightarrow 0$ and $Re_n \gg 1$, the dimensionless equations are

$$\frac{\partial u_x}{\partial t} + u_x \frac{\partial u_x}{\partial x} + \frac{F_h^2}{\alpha^2} u_z \frac{\partial u_x}{\partial z} = -\frac{\partial p}{\partial x} + \frac{1}{Re_n} \frac{1}{\alpha^n} \frac{\partial^n u_x}{\partial z^n}, \quad (2.39)$$

$$0 = -\frac{\partial p}{\partial z} + b, \quad (2.40)$$

$$\frac{\partial b}{\partial t} + u_x \frac{\partial b}{\partial x} + \frac{F_h^2}{\alpha^2} u_z \frac{\partial b}{\partial z} = -u_z + \frac{1}{Re_n Sc_n} \frac{1}{\alpha^n} \frac{\partial^n b}{\partial z^n}, \quad (2.41)$$

$$\frac{\partial u_x}{\partial x} + \frac{F_h^2}{\alpha^2} \frac{\partial u_z}{\partial z} = 0. \quad (2.42)$$

We can distinguish two different regimes depending on the relative magnitude of the vertical advection term, which is $\mathcal{O}(F_h^2/\alpha^2)$, and the diffusion terms, which are of order $\mathcal{O}(1/(Re_n \alpha^n))$. The state of the flow is determined by the ratio of these two quantities

$$\mathcal{R}_n = Re_n F_h^2 \alpha^{n-2},$$

where \mathcal{R}_n is the buoyancy Reynolds number of order n . If $n = 2$ we obtain $\mathcal{R}_2 = ReF_h^2$, as in 3D case (Brethouwer et al., 2007).

$\mathcal{R}_n \gg 1$: Strongly stratified turbulence regime. The viscous and diffusive terms can be neglected compared to the vertical advection terms. Analogously to the work of Billant, Chomaz (2001), we do not make any assumption on the magnitude of $\alpha = l_z/l_x$. The aspect ratio α will be determined by the dominant balance principle. Billant, Chomaz (2001) proposed a group of invariance suggesting the existence of self-similarity respect to the $z'N/U_x$, where z' is the vertical dimensional coordinate. The group of invariances implies that the characteristic vertical scale of the flow is inversally proportional to the buoyancy frequency N . When N increases, the vertical scale decreases as $l_z \propto 1/N$. By dimensional considerations the characteristic vertical scale of the flow is $l_z = U_x/N$, leading to $F_v = 1$. A vertical Froude number order of unity $F_v = 1$ implies that $F_h \sim \alpha$. The equations of the strongly stratified turbulence regime are expressed as

$$\frac{\partial u_x}{\partial t} + u_x \frac{\partial u_x}{\partial x} + u_z \frac{\partial u_x}{\partial z} = -\frac{\partial p}{\partial x}, \quad (2.43)$$

$$0 = -\frac{\partial p}{\partial z} + b, \quad (2.44)$$

$$\frac{\partial b}{\partial t} + u_x \frac{\partial b}{\partial x} + u_z \frac{\partial b}{\partial z} = -u_z, \quad (2.45)$$

$$\frac{\partial u_x}{\partial x} + \frac{\partial u_z}{\partial z} = 0. \quad (2.46)$$

The buoyancy Reynolds number in the strongly stratified turbulence regime is

$$\mathcal{R}_n = Re_n F_h^n. \quad (2.47)$$

$\mathcal{R}_n \ll 1$: Viscosity-affected stratified flow regime. The vertical advection term is negligible compared to the viscous terms. Godoy-Diana et al. (2004) argued that the vertical length scale can only be determined by the balance between the horizontal advection term and the vertical diffusion term

$$\frac{1}{Re_n \alpha^n} \sim 1 \rightarrow l_z \sim l_x Re_n^{-1/n}. \quad (2.48)$$

The non-dimensional equations of the viscosity-affected stratified turbulence regime are expressed as

$$\frac{\partial u_x}{\partial t} + u_x \frac{\partial u_x}{\partial x} = -\frac{\partial p}{\partial x} + \frac{\partial^n u_x}{\partial z^n}, \quad (2.49)$$

$$0 = -\frac{\partial p}{\partial z} + b, \quad (2.50)$$

$$\frac{\partial b}{\partial t} + u_x \frac{\partial b}{\partial x} = -u_z + \frac{1}{Sc_n} \left[\frac{\partial^n b}{\partial z^n} \right], \quad (2.51)$$

$$\frac{\partial u_x}{\partial x} = 0. \quad (2.52)$$

Chapter 3

Numerical setup and description of a characteristic simulation

In this chapter, I present the solver used to perform Direct Numerical Simulations (DNS) of 2D stratified turbulence. In particular, I focus on my contributions as developer of the solver `fluidsim.solvers.ns2d.strat` (`ns2d.strat`). In the second part of the chapter, I describe a characteristic simulation using the existing and new outputs developed during this thesis.

3.1 `ns2d.strat`: 2D Boussinesq equations solver

This PhD work has been done with the Computational Fluid Dynamics (CFD) framework FluidSim (Mohanani et al., 2019b), which is part of the wider project FluidDyn (Augier et al., 2019). All developments during this thesis have been done in the FluidSim solver `ns2d.strat`. All solvers in FluidSim are parallel High-Performance Computing (HPC) codes with a scientific Python and C++ ecosystem. FluidSim solvers are defined by the equations solved and the numerical methods used. A solver also contains code to save, process and plot output data. FluidSim is a very general framework so few assumptions on the numerical methods are done in the core of the package. Some FluidSim solvers use other CFD codes like Dedalus and Basilisk. However, the most mature FluidSim solvers are based on spectral methods taking advantage of Fast Fourier Transform libraries (Mohanani et al., 2019a). It has been demonstrated that these solvers are highly efficient compared to more traditional HPC fluid mechanics codes, and they can be run in parallel on many cores with MPI communications.

The solver used during this thesis, `ns2d.strat`, solves the 2D Navier-Stokes equations under the Boussinesq approximation with periodic boundary conditions (equations 1.5 - 1.7) in the following form:

$$\partial_t \hat{\xi} = -\widehat{\mathbf{u} \cdot \nabla} \xi - ik_x \hat{b} + \hat{f}_\xi - \nu_m |\mathbf{k}|^m \hat{\xi}, \quad (3.1)$$

$$\partial_t \hat{b} = -\widehat{\mathbf{u} \cdot \nabla} b + N^2 \hat{u}_z + \hat{f}_b - \kappa_m |\mathbf{k}|^m \hat{b}. \quad (3.2)$$

The vorticity $\hat{\xi}$ rather than the momentum equation is used for performance reasons. The horizontal and vertical components of the velocity in the spectral space are expressed as \hat{u}_x and \hat{u}_z respectively. The vertical component of the velocity \hat{u}_z can be expressed as a function of the vorticity $\hat{\xi}$ as $\hat{u}_z = (\hat{\xi} + k_z \hat{u}_x)/k_x$. \hat{f}_ξ and \hat{f}_b are the forcing terms for the vorticity and buoyancy equations. ν_m and κ_m are, respectively, the hyper-viscosity and hyper-diffusivity coefficients of order m . Hyper-viscosity is used in order to get an inertial-range weakly affected by the viscosity. It has been demonstrated that a bottleneck can appear when using hyper-viscosity instead of the Navier-Stokes viscosity (Lamorgese et al.,

2005). The bottleneck is a bump in the energy spectra between the inertial range and the dissipative range. All simulations in this thesis are computed with $m = 8$. Moreover, the bottleneck tends to be larger with higher-order hyperviscosity. The time integration of the non-linear terms is carried out using a fourth-order Runge-Kutta scheme. Full dealiasing according to the 2/3-rule is used in all simulations.

3.2 Forcing scheme

In this section, I present the forcing scheme used in the solver `ns2d.strat`. One can force two forcing regions in Fourier space (see figure 3.1): ring-shaped or rectangular region. Two quantities can be forced at each region: vorticity ξ and linear mode \hat{a}_+ . Forcing the vorticity, one injects only kinetic energy. On the other hand, forcing the linear mode injects kinetic and potential energy. Furthermore, forcing the linear mode \hat{a}_+ allows us to excite internal gravity waves propagating with the same direction as the wavenector \mathbf{k} . These waves are called prograde waves. The wavenector \mathbf{k} is a parameter of the simulation.

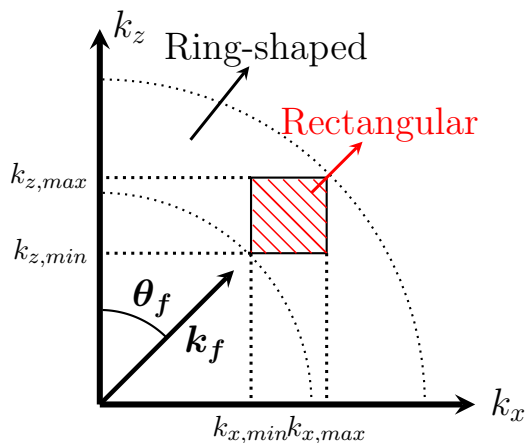


Figure 3.1: Forcing regions in the spectral space: ring-shaped (black) and rectangular (red). At the ring-shaped region, we impose only a forcing wavenumber k_f . At the rectangular region, we impose a forcing wavenumber k_f , and a direction given by the angle θ_f .

3.2.1 About the forcing region: ring-shaped versus rectangular

All previous numerical studies on 2D stratified turbulence used a ring-shaped forcing region (see works of Boffetta et al. (2011) and Kumar et al. (2017)). Furthermore, they force only the momentum equation on modes with all possible directions in the Fourier space. The linear dispersion of internal gravity waves relates the frequency of wave propagation with its direction (see equation (1.19)). By exciting all possible modes in all possible directions, one excites all time scales τ_l comprised between $\tau_l \sim [0, N^{-1}]$. The forcing is not localized in one frequency.

In the ocean, internal gravity waves are often excited with a similar time scale. For example, tides passing over a topography excite waves with periods τ_l similar to the tidal period $\tau_l \sim T_{tide}$. We are interested in forcing waves with similar time scale. I have developed a new forcing scheme for the solver `ns2d.strat`, which allows us to force modes in a rectangular region of the spectral space in order to excite waves with a similar time scale. Figure 3.1 represents the two different forcing regions: ring-shaped (black) and rectangular (red). With the ring-shaped forcing region, we impose only a forcing wavenumber k_f . With the rectangular forcing region, we impose a forcing wavenumber

k_f , and a direction given by the angle θ_f . By forcing a ring-shaped region, we excite all possible modes with a wavenumber similar to the forcing wavenumber $k \sim k_f$. We excite thus all possible directions. By forcing the rectangular region, we inject energy at modes with $k \sim k_f$ and with one direction given by the angle θ_f , i.e. one frequency $\omega_f = N \sin \theta_f$. We excite only one possible direction of propagation.

New forcing scheme for the solver ns2d.strat

We have developed a new class `TimeCorrelatedRandomPseudoSpectralAnisotropic` in the solver `NS2D.strat`. The caption 3.1 displays the two added parameters. The parameter, `angle`, corresponds to the angle θ_f . The parameter is set to `angle=45` by default. It means that waves will propagate with 45 degrees with the vertical direction. The second parameter, `kz_enable`, allows us to force modes with negative vertical wavenumber k_z . When forcing waves in the first quadrant $k_z > 0$ of the spectral space, we force waves in the third quadrant as well, i.e. the linear mode is a real field. When forcing in the first and second quadrant, we force therefore waves in all four quadrants of the spectral space. By default, `kz_enable=False`, we force only modes with positive vertical wavenumber.

Listing 3.1: Class `TimeCorrelatedRandomPseudoSpectralAnisotropic`

```
class TimeCorrelatedRandomPseudoSpectralAnisotropic(
    TimeCorrelatedRandomPseudoSpectral
):
    """Random normalized anisotropic forcing.

    .. inheritance-diagram:: TimeCorrelatedRandomPseudoSpectralAnisotropic
        """

    tag = "tcrandom_anisotropic"

    @classmethod
    def _complete_params_with_default(cls, params):
        """This static method is used to complete the *params* container.
        """

        params.forcing._set_child(
            "tcrandom_anisotropic", {"angle": "45", "kz_negative_enable": False}
        )
```

3.2.2 About the forcing quantity: vorticity $\hat{\xi}$ versus linear mode \hat{a}_+

In the solver ns2d.strat, one can force two quantities: vorticity $\hat{\xi}$ and the linear mode \hat{a}_+ . When forcing the vorticity, only the equation (3.1) is excited through the term \hat{f}_ξ . When forcing the linear mode \hat{a}_+ , both equations (equation (3.1) and (3.2)) are excited through the forcing terms \hat{f}_ξ and \hat{f}_b . We focus now on the mathematical relation between the vorticity $\hat{\xi}$ and the linear mode \hat{a}_+ . The vorticity can be expressed as a function of the linear modes \hat{a}_+ and \hat{a}_- as

$$\hat{\xi} = \frac{1}{2N^2} \left(\frac{k_x^2 + k_z^2}{k_x} \right) (\hat{a}_+ + \hat{a}_-). \quad (3.3)$$

We see that the vorticity depends on both linear modes \hat{a}_+ and \hat{a}_- . It means that both linear modes are excited when forcing the vorticity (see figure 3.2 (a)). It excites thus prograde and retrograde waves. Prograde waves propagate in the same direction as \mathbf{k} . Retrograde waves propagate in the opposite direction to \mathbf{k} .

One of the scopes of this PhD work is to investigate whether the dynamics is dominated by a wave energy cascade or not. In chapter 4, we perform DNS of 2D stratified turbulence forced by internal gravity waves, i.e. only the linear mode \hat{a}_+ is forced. We excite only prograde waves (figure 3.2 (b)). In the past, several studies of 3D stratified turbulence forced the vortical and wave modes. They attempted to explain the anisotropy of the energy spectra observed in the nature. Waite, Bartello (2004) performed numerical simulations of vortically forced stratified turbulence. In the work of Waite, Bartello (2006a), they force randomly internal gravity waves in 3D stratified turbulence. They attempt to reproduce the saturation energy spectrum $E(k_z) \sim N^2 K_z^{-3}$. In both studies, the resulting vertical energy spectrum is shallower than the typical observations in the atmosphere and ocean.

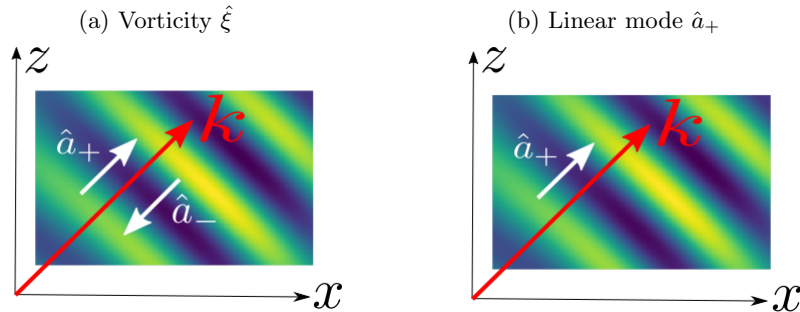


Figure 3.2: Schema of forcing the vorticity $\hat{\xi}$ (a) and linear mode \hat{a}_+ (b). The red arrow \mathbf{k} represents the wavevector of the forced modes. By forcing the vorticity $\hat{\xi}$ (a), we force both prograde \hat{a}_+ and retrograde \hat{a}_- waves. By forcing the linear mode \hat{a}_+ (b), we only excite prograde waves.

3.2.3 Normalization of the forcing in the solver ns2d.strat

In the above section, we have seen that one can force two quantities: vorticity $\hat{\xi}$ and the linear mode \hat{a}_+ . The rates of injection of these quantities are expressed as P_ξ (for the vorticity) and P_a (for the linear mode), respectively. The quadratic quantity of the vorticity is the enstrophy. The units of the injection rate of enstrophy $P_\xi = [T]^{-3}$, where $[T]$ is a characteristic time scale. The units of the injection rate of the quadratic quantity for the linear mode are $P_a = [L]^2[T]^{-7}$, where $[L]$ is a characteristic length scale.

The solver ns2d.strat normalizes the forcing terms \hat{f}_ξ and \hat{f}_b of the equations (3.1) and (3.2). The forcing terms are initially normalized such that the average over a time step of the injection rate of the quadratic quantity be constant and equal to P_ξ (when forcing vorticity $\hat{\xi}$) or to P_a (when forcing the linear mode \hat{a}_+). In the following, I explain the normalization of the forcing term for the case of the vorticity. We force the vorticity $\hat{\xi}$ with a forcing term \hat{f}_ξ . We can thus express the evolution of the vorticity as

$$\partial_t \hat{\xi} = \hat{f}_\xi. \quad (3.4)$$

We normalize now the forcing term \hat{f}_ξ such that the averaged injection rate P_ξ of the quadratic quantity of the vorticity is constant over a time step δt . One can write the evolution of the quadratic quantity of the vorticity such as

$$\partial_t |\hat{\xi}|^2 = \partial_t \hat{\xi}^* \hat{\xi} = \hat{\xi}^* \hat{f}_\xi, \quad (3.5)$$

where $\hat{\xi}^*$ is the complex conjugate of the vorticity $\hat{\xi}$. Considering the equation (3.5) of the quadratic quantity of the vorticity, the average of the injection rate P_ξ over a time step δt is given by

$$P_\xi = \int_0^{\delta t} \frac{dt}{\delta t} \sum_{\mathbf{k}} \frac{\partial_t |\hat{\xi}|^2}{2} = \int_0^{\delta t} \frac{dt}{\delta t} \sum_{\mathbf{k}} \hat{\xi}^* \hat{f}_\xi. \quad (3.6)$$

At this point, we consider a first-order approximation for the value of the vorticity at a given time t such as

$$\hat{\xi}(t) \simeq \hat{\xi}(t=0) + \hat{f}_\xi t. \quad (3.7)$$

Considering the first-order approximation, the expression of the injection of the quadratic quantity, equation (3.6), becomes

$$P_\xi \simeq \sum_{\mathbf{k}} \hat{\xi}^*(t=0) \hat{f}_\xi + \sum_{\mathbf{k}} \frac{|\hat{f}_\xi|^2}{2} \delta t. \quad (3.8)$$

The forcing term \hat{f}_ξ is proportional to the random forcing \hat{f}_r as

$$\hat{f}_\xi = R \hat{f}_r. \quad (3.9)$$

Finally, one obtains the following quadratic equation

$$\left(\sum_{\mathbf{k}} \frac{|\hat{f}_r|^2}{2} \delta t \right) R^2 + \left(\sum_{\mathbf{k}} \hat{\xi}^*(t=0) \hat{f}_r \right) R - P_\xi = 0, \quad (3.10)$$

which gives the value of the coefficient R for which the injection rate P_ξ is constant. The fact that the two different forcing terms (vorticity \hat{f}_ξ and the linear mode \hat{f}_a) are normalized by different quantities, it does not allow us to compare the two dynamics. In order to overcome this issue, the forcing is now normalized by the total energy injection rate P_E . The units of the energy injection rate are $P_E = [L]^2[T]^3$. The forcing terms in all simulations of this manuscript are normalized by the energy injection rate P_E .

3.3 Time scales of the problem

We can compute three different frequencies (inverse of the time scale) in the problem: (1) frequency of the forced waves; (2) frequency computed from the amplitude of the forcing; (3) frequency of the time correlation of the forcing.

(1) Frequency of the forced waves. The new forcing scheme allows to set the angle θ_f (see figure 3.1). It is the angle between the wavevector \mathbf{k}_f and the vertical direction. It sets the direction of propagation of the forced waves. We consider the linear dispersion relation of internal gravity waves expressed in the equation (1.19). One can thus relate the frequency of the waves to their direction of propagation. We can compute the characteristic time scale of the forced waves as

$$\omega_l = N \sin \theta_f, \quad (3.11)$$

where N is the Brunt-Väisälä frequency.

(2) Frequency of the forcing amplitude. In addition to the forcing angle θ_f , there are two other parameters which need to be specified: the injection rate P and the forcing wavevector \mathbf{k}_f . As it is mentioned above, the forcing is normalized by the total energy injection rate P_E . We can then compute the time scale of the amplitude of the forcing as

$$\omega_{af} = (P_E k_f^2)^{1/3}. \quad (3.12)$$

(3) Frequency of the time correlation of the forcing. The forcing is correlated in time with a frequency of correlation given by

$$\omega_{cf} = \frac{2\pi}{\tau_{cf}}, \quad (3.13)$$

where τ_{cf} is the time correlation of the forcing. The time correlation is chosen by the user. For all the simulations in the present work, I set the time correlation of the forcing to be the same as the period of the forced waves, $\omega_{cf} = \omega_l$.

Summary of the time scales

| Forced waves | Amplitude forcing | Correlation forcing |
|------------------------------|-----------------------------------|--------------------------|
| $\omega_l = N \sin \theta_f$ | $\omega_{af} = (P_E k_f^2)^{1/3}$ | $\omega_{cf} = \omega_l$ |

Table 3.1: Summary of the time scales of the solver ns2d.strat

Non-dimensional parameters

From the time scales presented above, one can build two non-dimensional parameters. We define the non-dimensional quantity F as the ratio between the time scale of the forced waves ω_l and the Brunt-Väisälä frequency N

$$F = \frac{\omega_l}{N} = \sin \theta_f. \quad (3.14)$$

It indicates the direction of propagation of the forced waves. The non-dimensional parameter F is within the range $[0, 1]$. All simulations presented in this thesis are computed with $F = 0.7$ ($\theta_f = 45^\circ$). The forced waves have similar vertical and horizontal scale, which is the simplest case we found to study turbulence driven by internal waves. Furthermore, we build the non-dimensional parameter γ as the ratio between the time scale of the forced waves ω_l and the time scale of the amplitude of forcing

$$\gamma = \frac{\omega_l}{\omega_{af}}. \quad (3.15)$$

It indicates the intensity of the stratification in comparison to the forcing strength. Low values of γ indicate that the dynamics is weakly stratified and strongly non-linear. The flow feels little the effects of stratification. In the limit $\gamma \rightarrow 0$, the dynamics can be considered as quasi 2D turbulence with a passive scalar (buoyancy) advected by the flow. On the other hand, the dynamics is strongly stratified and weakly non-linear for large γ . The effects of stratification are important in comparison to the forcing. The direction of gravity becomes a preferential direction. Strongly stratified flows are expected to be strongly anisotropic. Geophysical flows such as the atmosphere and oceans are characterized for being strongly stratified flows (Riley, Lindborg, 2008). In stratified turbulence, the horizontal Froude number F_h is commonly used to characterize the influence of the stratification on the flow dynamics. The horizontal Froude number can be expressed as

$$F_h = \frac{U}{NL_h}, \quad (3.16)$$

where U is a characteristic velocity, N is the Brunt-Väisälä frequency and L_h is a characteristic horizontal scale. For low values of horizontal Froude number $F_h \ll 1$, the flow is strongly influenced by the stratification. Moreover, one can express the horizontal Froude number F_h in terms of the input non-dimensional parameters F (geometry of the forcing) and γ (intensity of the stratification). The new horizontal Froude number is denoted as $F_{h,f}$. It can be interpreted as a forcing horizontal Froude number. One can express the Brunt-Väisälä frequency as $N = \omega_l/F$. The characteristic velocity is expressed as $U \sim \omega_{af}/k_f$. One can thus express the forcing horizontal Froude number $F_{h,f}$ as

$$F_{h,f} = \frac{F}{\gamma}. \quad (3.17)$$

We can compute a forcing Reynolds number $Re_{8,f}$ from the the forcing parameters P (energy injection rate) and \mathbf{k}_f (wavevector associated with the forced modes)

$$Re_{8,f} = \frac{1}{\nu_8} \left(\frac{P_E}{|\mathbf{k}_f|^{22}} \right)^{1/3}. \quad (3.18)$$

ν_8 is the hyper-viscosity coefficient. We use hyper-viscosity in order to localize the dissipation at small scales. Hence, we have less grid points dedicated to the dissipative range and more to the inertial range. Note that due to the use of hyper-viscosity, numerical values of

the $Re_{8,f}$ should not be compared to usual values of the real Reynolds number. The computation of the hyper-viscosity coefficient is presented later in section 3.6. To conclude, the ratio between the hyper-viscosity ν_8 and diffusivity κ_8 is the Schmidt number

$$Sc_8 = \frac{\nu_8}{\kappa_8}. \quad (3.19)$$

For all simulations presented in this PhD work, the Schmidt number is order of unity $Sc_8 = 1$.

Summary of the non-dimensional parameters

| Geometry | Stratification strength | Forcing Froude | Forcing Reynolds | Schmidt |
|-------------------|---|------------------------------|--|-------------------------------------|
| $F = \sin \theta$ | $\gamma = \frac{\omega_l}{\omega_{af}}$ | $F_{h,f} = \frac{F}{\gamma}$ | $Re_{8,f} = \frac{1}{\nu_8} \left(\frac{P_E}{ k_f ^{22}} \right)^{1/3}$ | $Sc_8 = \frac{\nu_8}{\kappa_8} = 1$ |

Table 3.2: Summary of the non-dimensional parameters.

Scaling analysis of the 2D Navier-Stokes equations for the forced large-scale waves

In this section, we have introduced the three different time scales associated with the forcing scheme: forced waves, amplitude forcing and time correlation of the forcing. Furthermore, two non-dimensional parameters $\{F, \gamma\}$, built from these time scales, have been presented. At this point, it is therefore important to update the scaling analysis performed in chapter 2 for the case of forced large-scale waves, including the non-dimensional parameters of our forcing scheme $\{F, \gamma\}$.

We consider the set of equations in the dimensionless form (see equations (2.31) - (2.34)) with an hyper-viscosity coefficient of order n . We consider now the aspect ratio α scales as the ratio of the forced vertical and horizontal length scales $\alpha = k_{fx}/k_{fz}$. We can thus express the α as function of the angle of propagation F as

$$\sin^2 \theta = \frac{k_{fx}^2}{k_{fx}^2 + k_{fz}^2} \rightarrow \alpha^2 = \frac{F^2}{1 - F^2}.$$

At this point, we attempt to express the horizontal Froude number $F_h = U_x/l_x N$ as function of the two non-dimensional parameters $\{F, \gamma\}$ as

$$F_h = \frac{U_x}{l_x N} \simeq \frac{F}{\omega_l} P_E^{1/3} k_{f,x}^{2/3} = \frac{\omega_{af}}{\omega_l} \sin \theta = \frac{F}{\gamma},$$

where P_E is the energy injection rate, ω_{af} is the characteristic frequency of the forcing amplitude, ω_l is the characteristic frequency of the forced waves and $\gamma = \omega_l/\omega_{af}$ is the ratio between the characteristic the two characteristic frequencies. The non-dimensionless

equations can be expressed as

$$\frac{\partial u_x}{\partial t} + u_x \frac{\partial u_x}{\partial x} + \frac{1 - F^2}{\gamma^2} u_z \frac{\partial u_x}{\partial z} = -\frac{\partial p}{\partial x} + \frac{1}{Re_n} \left[\frac{\partial^n u_x}{\partial x^n} + \frac{(1 - F^2)^{n/2}}{F^n} \frac{\partial^n u_x}{\partial z^n} \right], \quad (3.20)$$

$$\frac{F^2}{\gamma^2} \left[\frac{\partial u_z}{\partial t} + u_x \frac{\partial u_z}{\partial x} + \frac{1 - F^2}{\gamma^2} u_z \frac{\partial u_z}{\partial z} \right] = -\frac{\partial p}{\partial z} + b + \frac{F^2}{\gamma^2 Re_n} \left[\frac{\partial^n u_z}{\partial x^n} + \frac{(1 - F^2)^{n/2}}{F^n} \frac{\partial^n u_z}{\partial z^n} \right] \quad (3.21)$$

$$\frac{\partial b}{\partial t} + u_x \frac{\partial b}{\partial x} + \frac{1 - F^2}{\gamma^2} u_z \frac{\partial b}{\partial z} = -u_z + \frac{1}{Re_n Sc_n} \left[\frac{\partial^n b}{\partial x^n} + \frac{(1 - F^2)^{n/2}}{F^n} \frac{\partial^n b}{\partial z^n} \right], \quad (3.22)$$

$$\frac{\partial u_x}{\partial x} + \frac{1 - F^2}{\gamma^2} \frac{\partial u_z}{\partial z} = 0. \quad (3.23)$$

The different regimes depend thereby on the relative magnitude of the vertical advection term $\mathcal{O}(1 - F^2/\gamma^2)$ and the diffusion terms $\mathcal{O}((1 - F^2)^{n/2}/Re_n F^n)$. We thus consider an order for the hyper-viscosity coefficient $n = 8$. We can thus express the ratio between the vertical advection terms and the diffusion terms as

$$\mathcal{R}_{w,8} = \frac{F^8 Re_8}{\gamma^2 (1 - F^2)^3}. \quad (3.24)$$

$\mathcal{R}_{w,8}$ can be interpreted as a modified buoyancy Reynolds number for the case of forced large-scale waves. Unlike the scaling analysis presented by Brethouwer et al. (2007), we have three relevant non-dimensional parameters $\{F, \gamma, Re_8\}$ when forcing with large-scale waves: (1) the direction of propagation of these waves, (2) the relative magnitude of the amplitude of forcing with the forced waves, and (3) the modified Reynolds number by the hyper-viscosity coefficient ν_8 .

3.4 Output modules of the solver ns2d.strat

In this section, I present all output modules of the solver ns2d.strat. I list the existing modules and the new modules developed during this thesis. As mentioned in section 3.1, each output module is a postprocessing tool with saving, loading and plotting functionalities.

Existing output modules:

- Print output file:
 Module: `fluidsim/solvers/ns2d/strat/output/print_stdout.py`
 Class: `PrintStdOutNS2DStrat`
 It saves the mean energy, time elapsed and time-step of the simulation.
- Physical fields:
 Module: `fluidsim/solvers/ns2d/strat/output/phys_fields.py`
 Class: `PhysFields2DStrat`
 It saves the instantaneous velocity and buoyancy fields.
- Spatial averaged energy $\langle E \rangle$ and enstrophy $\langle Z \rangle$:
 Module: `fluidsim/solvers/ns2d/strat/output/spatial_means.py`
 Class: `SpatialMeansNS2DStrat`
 It saves the time evolution of averaged energy, enstrophy, energy and enstrophy injection rates and dissipation. This output is used to determine whether a simulation has reached stationarity or not.

- Horizontal $E(k_x)$ and vertical $E(k_z)$ energy spectra:
Module: `fluidsim/solvers/ns2d/strat/output/spectra.py`
Class: `SpectraNS2DStrat`
It is used to study how the energy is distributed among the scales.
- Horizontal and vertical spectral energy budget:
Module: `fluidsim/solvers/ns2d/strat/output/spect_energy_budget.py`
Class: `SpectralEnergyBudgetNS2DStrat`
It saves the horizontal $\Pi(k_x)$ and vertical $\Pi(k_z)$ flux of energy $\Pi(k)$, the spectral dissipation in both directions $D(k_x)$ and $D(k_z)$, and the spectral conversion term $B(k_x)$ and $B(k_z)$.

New output modules developed during this PhD:

- Two-dimensional energy spectra $E(k_x, k_z)$:
Module: `fluidsim/solvers/ns2d/strat/output/spectra_multidim.py`
Class: `SpectraMultiDimNS2DStrat`
It illustrates how the energy is distributed among horizontal and vertical scales. I have developed this output in order to study the effects of forcing different quantities, vorticity $\hat{\xi}$ and linear mode \hat{a}_+ , from the transitory to steady state (see chapter 6).
- Spatio-temporal energy spectra $E(k_x, k_z, \omega)$:
Module: `fluidsim/solvers/ns2d/strat/output/spatio_temporal_spectra.py`
Class: `SpatioTempSpectra`
It returns 4-D array with the energy spectra in the two-directions of the space and the temporal dimension. It illustrates how the energy is distributed, simultaneously, in space and time. I have developed this output in order to identify internal gravity waves (see chapter 5).
- Frequency energy spectra $F(\omega)$:
Module: `fluidsim/solvers/ns2d/strat/output/frequency_spectra.py`
Class: `FrequencySpectra`
It returns the frequency energy spectra of the linear modes \hat{a}_+ and \hat{a}_- . I have developed the output in order to identify internal gravity waves peaks (see chapter 5). Furthermore, it allows us to compare to ocean and atmospheric temporal spectra. Both outputs, spatio-temporal and frequency energy spectra, require saving a considerable number of fields in time.

3.5 Description of a characteristic simulation

In this section, I describe an example of a simulation carried out by the solver `ns2d.strat`. The numerical resolution is 1920×480 . The non-dimensional parameters of the simulation are

$$F = \sin \theta_f = 0.7 \qquad \gamma = \frac{\omega_l}{\omega_{af}} = 2. \qquad (3.25)$$

By setting $F = 0.7$ ($\theta_f = 45^\circ$), the forced waves will propagate with an angle 45° respect to the vertical direction. $\gamma = 2$ indicates that the effects of stratification are strong.

3.5.1 With or without shear modes?

In most of simulations on forced stratified turbulence, a large amount of energy accumulates in horizontally invariant and vertically sheared modes ($k_x = 0, k_z$). They are called "shear modes". The dynamics of these modes is still not well understood and different attempts have been done in order to explain their presence. Smith, Waleffe (2002) explains the growth of the shear mode energy by resonant three wave interactions. Lindborg, Brethouwer (2007) argues that the continuous increase of energy is due to the viscous effects. In previous numerical studies (Waite, Bartello (2004, 2006a); Maffioli et al. (2016); Herbert et al. (2016)), it has been observed that a substantial amount of energy often accumulates in these shear modes. In many cases, this accumulation continues through the whole simulation, so that a time stationary state is not reached (Lindborg, Brethouwer, 2007). Augier et al. (2014) states that these shear modes influence the whole cascade due to non-local interactions.

In order to study the influence of the shear modes on the dynamics, I have carried out two simulations with the same non-dimensional parameters: (a) I allow energy to go to the shear modes (*with shear modes*). (b) I prevent energy to go to the shear modes (*without shear modes*). We prevent energy to go to the shear modes by setting to zero the amplitude of energy of these modes at each time step of the simulation. Hence, there is no flux of energy towards the shear modes without inducing a sink of energy.

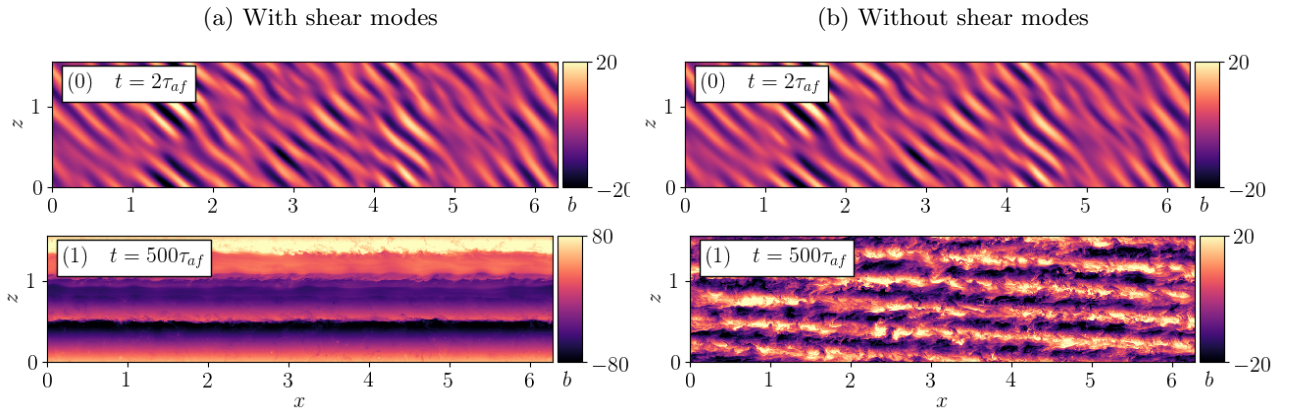


Figure 3.3: Snapshots of the buoyancy field for two simulations: (a) with shear modes ; (b) without shear modes. The buoyancy fields are displayed at two different times of the simulation: (0) $t = 2\tau_{af}$; (1) $t = 500\tau_{af}$.

Figure 3.3 shows the instantaneous buoyancy fields for the simulation with shear modes (figure 3.3 (a)) and without shear modes (figure 3.3 (b)). Two different times are displayed: at the beginning of the simulation ($0, t = 2\tau_{af}$); the end of the simulation ($1, t = 500\tau_{af}$). At the beginning of the simulation ($t = 2\tau_{af}$), we can notify the forced waves propagating at 45° respect to the vertical direction. The dynamics are similar for both simulations (with and without shear modes). At the end of the simulation ($t = 500\tau_{af}$), we clearly see different dynamics. The simulation with shear modes (figure 3.3 (a.1)), we see large horizontal scales with a size equals to the horizontal size of the box L_x , which means that the energy is concentrated at the shear modes. It has to be noted the large magnitude of the buoyancy, meaning that the energy is accumulating on these modes. When we prevent energy to go to shear modes (figure 3.3 (b.1)), we can see also large horizontal layers with small dissipative vertical scales. The horizontal layers are slightly inclined due to the interdiction of energy to go to the shear modes.

Figure 3.4 displays the time evolution of the energy (top) and energy dissipation (bottom) for both simulations: with shear modes (figure 3.4 (a)) and without shear modes (figure 3.4 (b)). The energy dissipation is normalized by the energy injection rate P . The orange lines represent the kinetic energy E_K and kinetic energy dissipation ϵ_K . The blue lines represent the potential energy E_A and potential energy dissipation ϵ_A . For the simulation with the shear modes (figure 3.4 (a)), both blue and orange lines increase along the whole simulation. It means that energy increases without being dissipated. This fact is due to the accumulation of the energy at the shear modes. In the simulation without shear modes (figure 3.4 (b)), the blue and orange lines converge around a constant values meaning that a stationary state is reached. At the beginning, the energy increases linearly with time. At $t \sim 200\tau_{af}$, the energy stops increasing meaning that the energy is being dissipated. The energy has been transferred from the injection scale to dissipative scales. At $t > 400\tau_{af}$, we can see that blue and orange lines start oscillating out of phase. It means that there is an exchange of energy between the kinetic energy E_K (orange line) and potential energy E_A (blue line). This exchange of energy is likely due to the waves with large horizontal scales observed in the figure 3.3 (b.1).

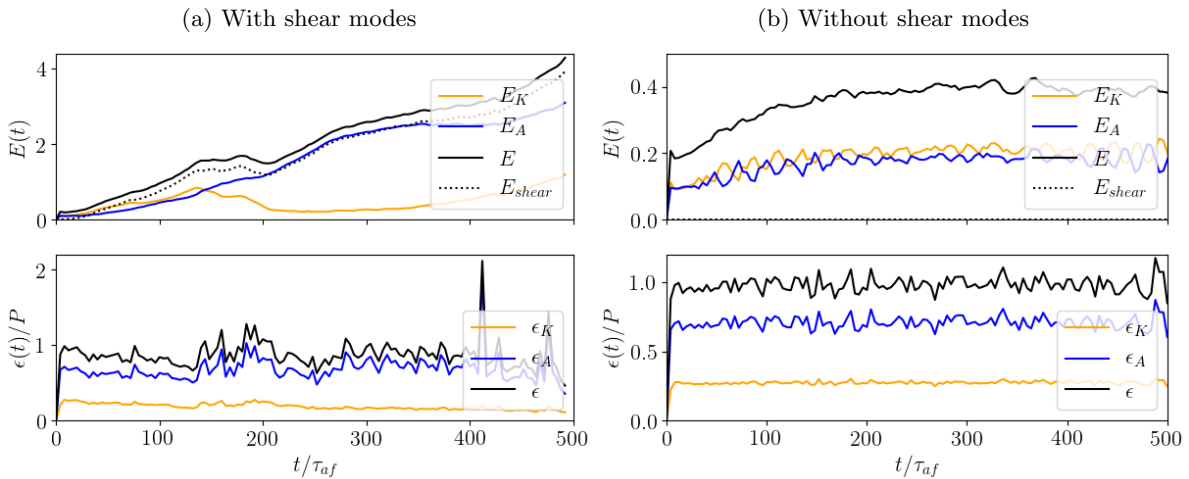


Figure 3.4: Time evolution of the total energy E (top, black solid line), kinetic energy E_K (top, orange line), potential energy E_A (top, blue line), energy of the shear modes E_{shear} (top, black dotted line), total energy dissipation ϵ (bottom, black line), kinetic energy dissipation ϵ_K (bottom, orange line) and potential energy dissipation ϵ_A (bottom, blue line). The energy dissipation is normalized by the energy injection rate P .

Performing numerical simulations with a pseudo-spectral code with periodic boundary conditions enhances the accumulation of the energy at the shear modes. The continuous increasing of energy at these modes does not allow us to reach a stationary state. The shear modes engender a non-physical state out of the scope of this PhD work. I prevent thus the energy to go to shear modes in all simulations presented in this thesis.

3.5.2 How is the structure of the flow?

One-dimensional energy spectra $E(k)$. I focus on the energy distribution among the different scales in the flow. Thus, I compute the horizontal $E(k_x)$ and vertical $E(k_z)$ energy spectra. The one-dimensional (1D) kinetic energy spectra $E_K(k)$ can be expressed as

$$E_K(k_x) = \frac{1}{2} \frac{1}{\delta k_x} \sum_{k_z} |\hat{\mathbf{u}}(k_x, k_z)|^2, \quad (3.26)$$

$$E_K(k_z) = \frac{1}{2} \frac{1}{\delta k_z} \sum_{k_x} |\hat{\mathbf{u}}(k_x, k_z)|^2, \quad (3.27)$$

where $\delta k_x = 2\pi/L_x$, $\delta k_z = 2\pi/L_z$ and $\hat{\mathbf{u}}(k_x, k_z)$ is the Fourier transform of the velocity. The 1D potential energy spectra $E_A(k)$ is computed as

$$E_A(k_x) = \frac{1}{2N^2} \frac{1}{\delta k_x} \sum_{k_z} |\hat{\mathbf{b}}(k_x, k_z)|^2, \quad (3.28)$$

$$E_A(k_z) = \frac{1}{2N^2} \frac{1}{\delta k_z} \sum_{k_x} |\hat{\mathbf{b}}(k_x, k_z)|^2, \quad (3.29)$$

where $\hat{\mathbf{b}}(k_x, k_z)$ are the Fourier transform of the buoyancy.

Figure 3.5 shows the horizontal (a) and vertical (b) compensated energy spectra. The orange lines correspond to the kinetic energy spectra $E_K(k)$. The blue lines correspond to the potential energy spectra $E_A(k)$. The horizontal energy spectra has been compensated by $k^{5/3}$. The vertical energy spectra has been compensated by k^3 . The grey vertical band represents the forcing wavenodes. The vertical dotted lines indicate the wavenumbers k_b and k_o corresponding to the buoyancy and Ozmidov length scales, respectively. The buoyancy length scale l_b represents the distance that a fluid particle, with a characteristic velocity U , can be displaced in a fluid with a background stratification N . It is also related to the thickness of the large horizontal layers observed in figure 3.3 (b.1). The wavenumber k_b associated with the buoyancy length scale is expressed dimensionally as

$$k_b = \frac{N}{U}. \quad (3.30)$$

The buoyancy wavenumber k_b can be expressed in terms of the non-dimensional parameters of the problem F (geometry forcing) and γ (stratification intensity) as

$$k_b \sim \frac{\gamma}{F} |\mathbf{k}_f|. \quad (3.31)$$

The Ozmidov scale l_o is also very used in stratified turbulence studies. It is the largest scale that can overturn in a stratified flow. For larger scale than the Ozmidov scale $l > l_o$, overturning is inhibited by the stratification. The wavenumber associated with the Ozmidov scale k_o can be expressed as

$$k_o = \left(\frac{N^3}{\epsilon} \right)^{1/2}, \quad (3.32)$$

where ϵ is the mean energy dissipation. In the stationary state, we can consider that the mean dissipation rate equals the energy injection rate $\epsilon \sim P_E$. Analogously to the buoyancy wavenumber, we can express the Ozmidov wavenumber k_o in terms of the non-dimensional parameters

$$k_o = \left(\frac{F}{\gamma}\right)^{3/2} k_f. \quad (3.33)$$

We first focus on the horizontal energy spectra (figure 3.5, (a)). The orange (kinetic energy spectrum) and blue (potential energy spectrum) lines are superposed for wavenumbers lower than the forcing wavenumbers $k < k_f$. This equipartition suggests waves are present at scales larger than the forcing scale. It has also to be noticed that there is a peak in the spectra at $k_x = 1\delta k_x$. It corresponds to the energy contained at the large horizontal layers observed in figure 3.3 (b.1). It should be a mechanism to transfer the energy from the injection scale to larger scales. We will see that this mechanism is due to the two-dimensional configuration. At scales smaller than the forcing scale $k > k_f$, blue and orange lines form a plateau. It means that there is a certain scale-scale energy transfer. At large enough wavenumbers the energy is dissipated. For the vertical energy spectra (figure 3.5 (b)), the blue and orange line have a peak within the grey vertical band. This peak of energy corresponds to the vertical forcing scale. At scales larger than the forcing scales $k < k_f$, there is no much energy. Energy is transferred directly towards small scales where it is dissipated. The adequate tools to validate these scenarios are the energy fluxes. The computation of these quantities are discussed later in section 3.5.3.

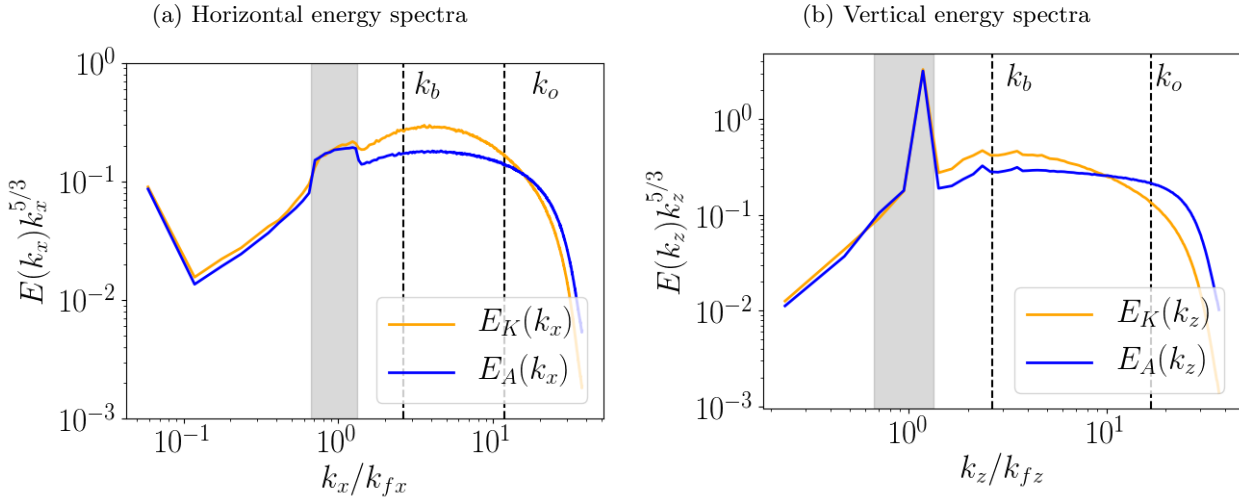


Figure 3.5: Horizontal (a) and vertical (b) one-dimensional energy spectra for $\gamma = 2.0$, $F = 0.7$ and forced on the vorticity $\hat{\xi}$. The energy spectra are compensated by the power law $k^{-5/3}$. The horizontal axes are normalized by the horizontal k_{fx} (left) and vertical forcing wavenumbers k_{fz} (right). The orange line represents the kinetic energy spectra. The blue line represents the potential energy spectra. The grey band represents the forcing region. The vertical dotted lines represent the buoyancy k_b and Ozmidov k_o wavenumbers respectively.

Two-dimensional energy spectra $E(\mathbf{k}_x, \mathbf{k}_z)$. We now want to analyze how the energy is distributed simultaneously along both, vertical and horizontal, directions. One can compute the two-dimensional energy spectra. The two-dimensional (2D) energy spectra is computed at each time step. The time decimation of the output can be specified by the user. The output computes the 2D energy spectra for the linear modes \hat{a}_+ and \hat{a}_- . It allows us to study the distribution of the quadratic quantity of both linear modes \hat{a}_+ and \hat{a}_- at different times of the simulation. In order to compute the 2D energy spectra, one has to compute first the 2D Fourier Transform of the linear eigenmode a_\pm as

$$\hat{a}_\pm(k_x, k_z) = \frac{1}{L_x} \frac{1}{L_z} \int_0^{L_x} \int_0^{L_z} a_\pm(\mathbf{x}) e^{-i\mathbf{k}\mathbf{x}} dx dz. \quad (3.34)$$

The energy of each Fourier mode is expressed as

$$\hat{E}_a(k_x, k_z) = \frac{1}{2} |\hat{a}_\pm(k_x, k_z)|^2. \quad (3.35)$$

The energy spectrum in the spectral space (k_x, k_z) is then

$$E_a(k_x, k_z) = \frac{1}{2} \frac{1}{\delta k_x} \frac{1}{\delta k_z} |\hat{a}_\pm(k_x, k_z)|^2, \quad (3.36)$$

where $\delta k_x = 2\pi/L_x$ and $\delta k_z = 2\pi/L_z$.

Figure 3.6 displays the 2D energy spectra for both linear modes \hat{a}_+ (figure 3.6 (top)) and \hat{a}_- (figure 3.6 (bottom)). It is displayed at three different times of the simulation: at the beginning $t = 0.2\tau_{af}$ (figure 3.6 (a)); at the transitory state $t = 2\tau_{af}$ (figure 3.6 (b)); at the steady state $t > 500\tau_{af}$ (figure 3.6 (c)). The colormap is the logarithm in base 10 of the energy spectra. The white rectangular regions represent the forcing regions. At the beginning of the simulation (figure 3.6 (a)), we can see highlighted white squares. It means that the energy is concentrated around the forcing region at early times. We can see that both linear modes \hat{a}_+ and \hat{a}_- are filled. It is due to the fact that the simulation is forced on the vorticity $\hat{\xi}$. Forcing the vorticity, we excite both linear modes (see equation (3.3)). At the transitory state (figure 3.6 (b)), we see regions with wavenumbers smaller than the forcing wavenumber $k < k_f$ highlighted, meaning that the energy has been transferred from the forcing scale to large scales through an inverse cascade mechanism. It has to be noticed that there is also a region with $k > k_f$ highlighted. This fact means that there is simultaneously a forward cascade mechanism that carries energy from forcing scales towards small scales. At the statistically stationary state (figure 3.6 (c)), a wide part of the spectral space is filled with energy. The energy has been spread out through all scales. It has to be noticed the existence of highlighted vertically aligned squares.

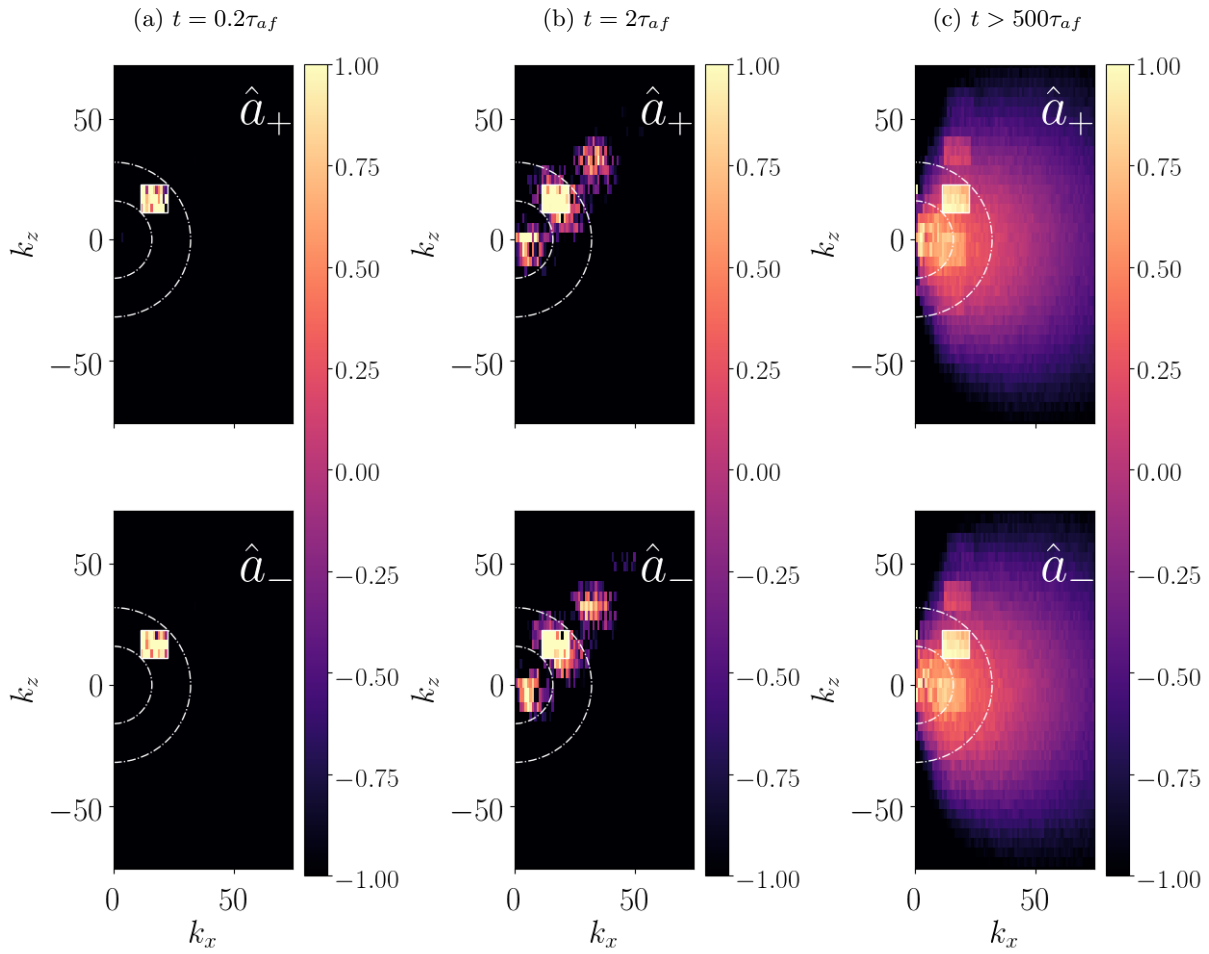


Figure 3.6: 2D energy spectra of the linear modes \hat{a}_+ and \hat{a}_- , and for three different times: (a) begin of the simulation $t = 0.2\tau_{af}$; (b) transient state $t = 2\tau_{af}$; (c) steady state $t > 500\tau_{af}$. The colormap represents the logarithm in base 10 of the energy spectra. The white square represents the forcing region. For $\gamma = 2.0$; Forced on vorticity $\hat{\xi}$; $k_z > 0$

3.5.3 Energy transfer mechanisms

In this section, I explain how the energy is transferred among the scales in the flow. We need to compute the spectral energy budget. The evolution equations of the kinetic $\hat{E}_K(\mathbf{k}) = |\hat{\mathbf{u}}|^2/2$ and potential $\hat{E}_A(\mathbf{k}) = |\hat{b}|^2/(2N^2)$ energies of a wavenumber \mathbf{k} can be expressed as

$$\frac{d\hat{E}_K(\mathbf{k})}{dt} = \hat{T}_K - \hat{b} - \hat{D}_K + \hat{F}_K, \quad (3.37)$$

$$\frac{d\hat{E}_A(\mathbf{k})}{dt} = \hat{T}_A + \hat{b} - \hat{D}_A + \hat{F}_A, \quad (3.38)$$

where $\hat{T}_K = -\mathbb{R}[\hat{\mathbf{u}}^*(\mathbf{k}) \cdot (\mathbf{u} \cdot \widehat{\nabla} \mathbf{u}(\mathbf{k}))]$ and $\hat{T}_A = -\mathbb{R}[\hat{b}^*(\mathbf{k}) \cdot (\mathbf{u} \cdot \widehat{\nabla} b(\mathbf{k}))]$ are the kinetic and potential nonlinear transfers, $\hat{D}_K(\mathbf{k}) = \nu_8 |\mathbf{k}|^{16} |\hat{\mathbf{u}}|^2$ and $\hat{D}_A(\mathbf{k}) = \kappa_8 |\mathbf{k}|^{16} |\hat{b}|^2$ are the kinetic and potential mean energy dissipation, $\hat{b}(\mathbf{k}) = \mathbb{R}[\hat{b}^*(\mathbf{k}) \hat{u}_z(\mathbf{k})]$ is the buoyancy flux from kinetic to potential energy, \hat{F}_K and \hat{F}_A are the Fourier transformed forcing terms. When the equations (3.37) and (3.38) are summed over horizontal and vertical wavenumbers in spectral space, we obtain,

$$\frac{dE_K(k)}{dt} = \Pi_K(k) - B(k) - \epsilon_K(k) + P_K(k), \quad (3.39)$$

$$\frac{dE_A(k)}{dt} = \Pi_A(k) + B(k) - \epsilon_A(k) + P_A(k). \quad (3.40)$$

where $E_K(k) = \sum_{k_x, k_z \leq k} \hat{E}_K(\mathbf{k})$. $\Pi_K(k)$ and $\Pi_A(k)$ is the kinetic and potential energy flux going outside of the wavenumber k , $\epsilon_K(k)$ and $\epsilon_A(k)$ are the kinetic and potential energy dissipations within $[0, k]$, $B(k)$ represents the flux of energy going from kinetic to potential energies, and $P_K(k)$ and $P_A(k)$ are the kinetic and potential energy injection rate by the forcing within the range $[0, k]$. Total quantities are unsubscripted, i.e. $\Pi = \Pi_K + \Pi_A$.

Figure 3.7 displays the energy fluxes and dissipation rates in the horizontal (figure 3.7 (a)) and vertical (figure 3.7 (b)) directions. All curves have been averaged over the time interval $600 \leq t \leq 850$, i.e. in the statistically stationary regime (see figure 3.4). The kinetic $\Pi_K(k)$ and potential $\Pi_A(k)$ are represented by the orange and blue lines respectively. They are normalized by the total mean dissipation rate ϵ . The black dotted line is the total energy flux computed as $\Pi(k) = \Pi_K(k) + \Pi_A(k)$. The green line is the cumulative dissipation $D(k)$. Since it is normalized by the mean dissipation rate ϵ , it should be equal to the unity at the smallest scales. In both horizontal and vertical, the black dotted line is positive for wavenumbers larger than the forcing wavenumber $k > k_f$. It means that in both cases, we have a forward cascade of energy, i.e. the energy is transferred from large to smaller scales. This transfer is forced by the fact that dissipation is only present at small scales. This energy transfer is dominated by the potential energy (blue line). We can see that the orange line is negative. It means that the kinetic energy flux Π_K is negative. The kinetic energy transfers its energy from small scales to large scales through an inverse cascade. For low wavenumbers $k < k_f$, the black dotted line is equal to zero, meaning that there is no flux of energy $\Pi(k) = 0$. It has to be noticed that dissipation ($D(k)$, green line) acts over the whole inertial range, indicating that our dynamics is affected by viscosity. This fact is due to the low resolution of this first simulation. As described in the next paragraph, the resolution imposes indeed a lower bound on the viscosity. This simulation has been performed to describe the essentials of the analysis of stratified turbulence dynamics. Later on this manuscript, I present simulations with larger resolutions to study strongly stratified flows weakly dominated by viscosity.

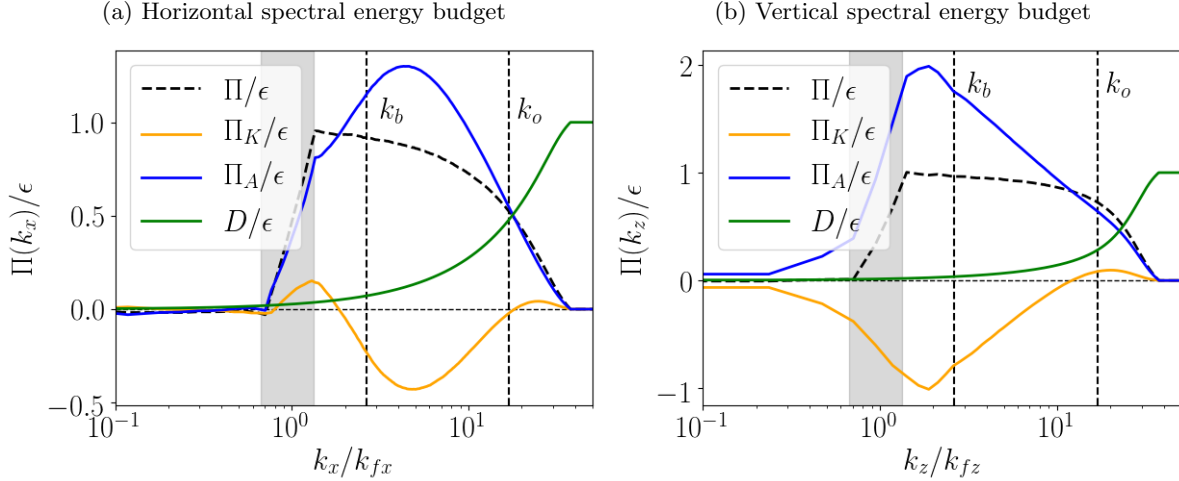


Figure 3.7: Horizontal (a) and vertical (b) spectral energy fluxes and dissipation for $\gamma = 2.0$, $F = 0.7$ and forced on the vorticity $\hat{\xi}$. The flux and dissipation are normalized by the mean dissipation rate of energy ϵ . The orange line represents the flux of kinetic energy Π_K . The blue line represents the flux of potential energy Π_A . The black dotted line represents the flux of the total energy Π . The green line represents the dissipation of total energy D .

3.6 Computation of the hyper-viscosity coefficient ν_8

Geophysical flows such as the atmosphere and the oceans have a large Reynolds number Re and small horizontal Froude number F_h (Brethouwer et al., 2007). They have indeed a wide range of scales (inertial regime) weakly affected by the dissipation. The aim of this PhD work is to investigate numerically the dynamics of the strongly stratified turbulence regime. We use the hyper-viscosity to localize the dissipation at small scales. We assign thus a larger proportion of grid points to the inertial range and less to the dissipative range than by using the Navier-Stokes viscosity. Several numerical studies of stratified turbulence adopted this approach in order to mimic large Reynolds number flows (Waite, Bartello, 2006b; Lindborg, 2006; Lindborg, Brethouwer, 2007; Brethouwer et al., 2007; Augier et al., 2015; Maffioli et al., 2016). In this section, I explain how the hyper-viscosity coefficient ν_m (see equation 3.1) is computed in the solver. The generalized dissipation operators are expressed as

$$D_K = \nu_n (-1)^{n+1} \nabla^{2n}, \quad (3.41)$$

$$D_A = \kappa_n (-1)^{n+1} \nabla^{2n}, \quad (3.42)$$

respectively, where ν_n and κ_n are the hyper-viscosity and hyper-diffusivity coefficients. All simulations of this thesis are computed with $n = 8$. As it has been presented above (see table 3.2), the ratio between the viscosity and diffusivity coefficients is given by the Schmidt number, $Sc_8 = \nu_8/\kappa_8 = 1$. It is chosen of order unity for simplicity, i.e. the hyper-viscosity and -diffusivity coefficients are equal.

The computation of the hyper-viscosity ν_8 for a given resolution is carried out through an iterative method. This method consists of performing short simulations, where ν_8 is updated in each simulation depending on the location of the spectral dissipation peak of the simulation. This peak should be at the highest possible wavenumber k , i.e. smallest possible scale. Figure 3.8 is a schematic representation of the spectral dissipation $D(k)$ of a simulation. After each simulation, we check the curve of the spectral dissipation $D(k)$. If the dissipation peak is located at too low wavenumbers, we decrease the coefficient ν_8 . On the other hand, if the dissipation peak is located at too large wavenumbers, we increase the coefficient ν_8 . We perform this iterative process until the coefficient ν_8 reaches a constant value and a steady state is achieved.

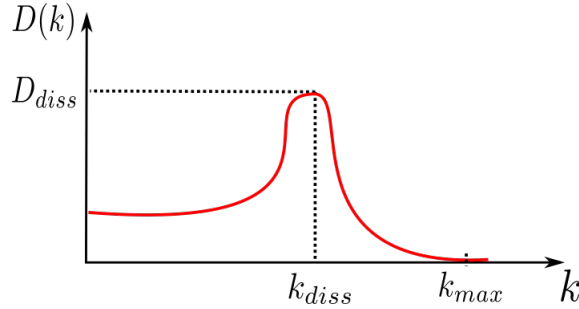


Figure 3.8: Representation of the spectral dissipation $D(k)$ of a simulation. We perform short simulations. In each simulation, the coefficient ν_8 is updated. We check the spectral dissipation peak of the simulation: (i) if the dissipation peak is located at too low wavenumbers, we decrease the coefficient ν_8 ; (ii) if the dissipation peak is located at too large wavenumbers, we increase the coefficient ν_8 .

The computation of the hyper-viscosity coefficient ν_8 has to be done for all stratification strengths, i.e. γ , and all numerical resolutions. However, this iterative process is considerable long for large resolutions. Hence, we have only computed ν_8 for three resolutions $[240 \times 60, 480 \times 120, 960 \times 240]$. We have fitted the points with a curve where we can extrapolate the coefficient for larger numerical resolutions $[1920 \times 480, 3840 \times 960]$. Figure 3.9 shows the hyper-viscosity coefficient ν_8 as function of the numerical resolution for three different stratification strengths, i.e. γ . The fit for each γ is indicated in the legend.

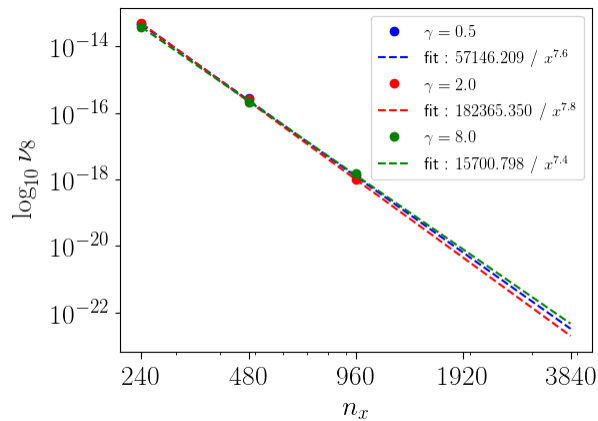


Figure 3.9: Hyper-viscosity coefficient ν_8 (logarithmic scale) as a function of the resolution for different values of $\gamma = 0.5$ (blue), $\gamma = 2.0$ (red) and $\gamma = 8.0$ (green). The coefficient ν_8 for larger resolutions have been computed by doing a fit of the data.

| Chapter | $n_x \times n_z$ | ν_8 | $\theta_f (^\circ)$ | γ | $F_{h,f}$ | Forced key | k_z |
|---|--------------------|----------|---------------------|----------|-------------|---------------|-----------|
| Chapter 3. Numerical setup | 1920 \times 480 | 4.48e-21 | 45 | 2.0 | 0.35 | $\hat{\xi}_+$ | $k_z > 0$ |
| | 1920 \times 480 | 4.48e-21 | 45 | 2.0 | 0.35 | $\hat{\xi}_+$ | $k_z > 0$ |
| Chapter 4. Effects of varying stratification | 15360 \times 960 | 4.30e-27 | 45 | 4.0 | 0.18 | \hat{a}_+ | $k_z > 0$ |
| | 15360 \times 960 | 2.50e-27 | 45 | 8.0 | 0.09 | \hat{a}_+ | $k_z > 0$ |
| | 15360 \times 960 | 2.30e-27 | 45 | 12.0 | 0.06 | \hat{a}_+ | $k_z > 0$ |
| | 7680 \times 480 | 8.51e-26 | 45 | 4.0 | 0.18 | \hat{a}_+ | $k_z > 0$ |
| | 7680 \times 480 | 2.78e-25 | 45 | 8.0 | 0.09 | \hat{a}_+ | $k_z > 0$ |
| | 7680 \times 480 | 2.56e-25 | 45 | 12.0 | 0.06 | \hat{a}_+ | $k_z > 0$ |
| | 3840 \times 960 | 2.55e-23 | 45 | 0.2 | 3.54 | \hat{a}_+ | $k_z > 0$ |
| | 3840 \times 960 | 2.82e-23 | 45 | 0.3 | 2.36 | \hat{a}_+ | $k_z > 0$ |
| | 3840 \times 960 | 3.05e-23 | 45 | 0.4 | 1.77 | \hat{a}_+ | $k_z > 0$ |
| | 3840 \times 960 | 3.28e-23 | 45 | 0.5 | 1.41 | \hat{a}_+ | $k_z > 0$ |
| | 3840 \times 960 | 3.45e-23 | 45 | 0.6 | 1.18 | \hat{a}_+ | $k_z > 0$ |
| | 3840 \times 960 | 3.82e-23 | 45 | 0.8 | 0.88 | \hat{a}_+ | $k_z > 0$ |
| | 3840 \times 960 | 4.07e-23 | 45 | 1.0 | 0.71 | \hat{a}_+ | $k_z > 0$ |
| | 3840 \times 960 | 2.01e-23 | 45 | 2.0 | 0.35 | \hat{a}_+ | $k_z > 0$ |
| | 3840 \times 960 | 2.14e-23 | 45 | 3.0 | 0.24 | \hat{a}_+ | $k_z > 0$ |
| | 3840 \times 960 | 2.03e-23 | 45 | 4.0 | 0.18 | \hat{a}_+ | $k_z > 0$ |
| | 3840 \times 960 | 1.70e-23 | 45 | 5.0 | 0.14 | \hat{a}_+ | $k_z > 0$ |
| | 3840 \times 960 | 1.60e-23 | 45 | 6.0 | 0.12 | \hat{a}_+ | $k_z > 0$ |
| | 3840 \times 960 | 1.39e-23 | 45 | 7.0 | 0.10 | \hat{a}_+ | $k_z > 0$ |
| | 3840 \times 960 | 4.70e-23 | 45 | 8.0 | 0.09 | \hat{a}_+ | $k_z > 0$ |
| | 3840 \times 960 | 4.32e-23 | 45 | 12.0 | 0.06 | \hat{a}_+ | $k_z > 0$ |
| | 3840 \times 960 | 5.40e-23 | 45 | 16.0 | 0.04 | \hat{a}_+ | $k_z > 0$ |
| | 1920 \times 480 | 5.31e-21 | 45 | 0.2 | 3.54 | \hat{a}_+ | $k_z > 0$ |
| | 1920 \times 480 | 6.37e-21 | 45 | 0.5 | 1.41 | \hat{a}_+ | $k_z > 0$ |
| | 1920 \times 480 | 7.37e-21 | 45 | 1.0 | 0.71 | \hat{a}_+ | $k_z > 0$ |
| | 1920 \times 480 | 4.48e-21 | 45 | 2.0 | 0.35 | \hat{a}_+ | $k_z > 0$ |
| | 1920 \times 480 | 4.76e-21 | 45 | 3.0 | 0.24 | \hat{a}_+ | $k_z > 0$ |
| | 1920 \times 480 | 4.85e-21 | 45 | 4.0 | 0.18 | \hat{a}_+ | $k_z > 0$ |
| | 1920 \times 480 | 4.05e-21 | 45 | 5.0 | 0.14 | \hat{a}_+ | $k_z > 0$ |
| | 1920 \times 480 | 3.83e-21 | 45 | 6.0 | 0.12 | \hat{a}_+ | $k_z > 0$ |
| | 1920 \times 480 | 3.32e-21 | 45 | 7.0 | 0.10 | \hat{a}_+ | $k_z > 0$ |
| | 1920 \times 480 | 7.93e-21 | 45 | 8.0 | 0.09 | \hat{a}_+ | $k_z > 0$ |
| 1920 \times 480 | 7.29e-21 | 45 | 12.0 | 0.06 | \hat{a}_+ | $k_z > 0$ | |
| 1920 \times 480 | 8.51e-21 | 45 | 16.0 | 0.04 | \hat{a}_+ | $k_z > 0$ | |
| 960 \times 240 | 1.06e-18 | 45 | 0.2 | 3.54 | \hat{a}_+ | $k_z > 0$ | |
| 960 \times 240 | 1.28e-18 | 45 | 0.5 | 1.41 | \hat{a}_+ | $k_z > 0$ | |
| 960 \times 240 | 1.25e-18 | 45 | 1.0 | 0.71 | \hat{a}_+ | $k_z > 0$ | |
| 960 \times 240 | 1.01e-18 | 45 | 2.0 | 0.35 | \hat{a}_+ | $k_z > 0$ | |
| 960 \times 240 | 1.01e-18 | 45 | 4.0 | 0.18 | \hat{a}_+ | $k_z > 0$ | |
| 960 \times 240 | 1.50e-18 | 45 | 8.0 | 0.09 | \hat{a}_+ | $k_z > 0$ | |
| 960 \times 240 | 1.49e-18 | 45 | 12.0 | 0.06 | \hat{a}_+ | $k_z > 0$ | |
| 960 \times 240 | 1.71e-18 | 45 | 16.0 | 0.04 | \hat{a}_+ | $k_z > 0$ | |

Table 3.3: List of the numerical simulations presented in the chapters 3 and 4. n_x and n_z are the horizontal and vertical numerical resolutions. ν_8 is the hyper-viscosity coefficient. $\gamma = \omega_l / \omega_{af}$ represents the ratio between the frequency of the forced waves ω_l and the frequency computed from the forcing amplitude ω_{af} . The forcing horizontal Froude number is expressed as $F_{h,f} = F / \gamma$, where $F = \sin \theta_f$ indicates the direction of propagation of the forced waves. Each simulation can be forced either on the vorticity $\hat{\xi}$ or on the linear mode \hat{a}_+ . The forcing can be applied on modes with positive vertical wavenumbers $k_z > 0$, or modes with both positive and negative vertical wavenumbers $k_z \gtrless 0$.

Chapter 4

Effects of varying the stratification and the Reynolds number

In this chapter, I discuss the effect of varying the stratification strength and the Reynolds number on 2D stratified turbulence. In section 4.1, I present numerical simulations with different stratification strength for a given Reynolds number. In section 4.2, I vary the Reynolds number for a fixed stratification strength. I quantify the isotropy at both large and small scales for the different regimes. The instability mechanism of the flow is analyzed qualitatively for different stratification strengths and Reynolds numbers. In section 4.4, a phenomenology of 2D stratified turbulence is presented with three different regimes. Finally, in section 4.5, I describe flows with large Reynolds number and small horizontal Froude, which are expected to be similar to the flows observed in nature.

In section 1.4, we have mentioned that two non-dimensional parameters control the dynamics of 3D stratified turbulence: (i) the horizontal Froude number F_h , and (ii) the Reynolds number Re . Nevertheless, these two non-dimensional quantities need to be updated in order to include the use of an hyperviscosity coefficient and the forcing of prograde internal gravity waves carried out in this PhD work. In section 3.3, two new non-dimensional quantities are presented as the parameters responsible to control the dynamics of 2D stratified turbulence. These two quantities are the forcing horizontal Froude number $F_{h,f}$ and the forcing Reynolds number $Re_{8,f}$. The latter one has been adapted with the hyper-viscosity coefficient ν_8 . The forcing horizontal Froude number quantifies the strength of the stratification. The Reynolds number $Re_{8,f}$ estimates the effect of the viscosity on the dynamics. The expressions of these two quantities have been derived in equations (3.17) and (3.18) as

$$F_{h,f} = \frac{F}{\gamma} \qquad Re_{8,f} = \frac{1}{\nu_8} \left(\frac{P}{k_f^{22}} \right)^{1/3}. \quad (4.1)$$

All numerical simulations are performed with the solver `ns2d.strat` presented in section 3.1. In this chapter, all simulations are forced on the linear mode \hat{a}_+ on only positive vertical wavenumbers $k_z > 0$, and with forcing angle is $\theta_f = 45^\circ$ (see section 3.2.2 for a reminder of the forcing quantities). We excite therefore prograde waves, which are waves propagating towards the same direction as the wavevector \mathbf{k}_f . The forcing scale is given by the band in the spectral space $4\delta k < |\mathbf{k}_f| < 8\delta k$, where $\delta k = 2\pi/L_z$. Furthermore, the forcing injects energy at a constant rate P . In order to avoid energy accumulation as observed in figure 3.3 (a), we prevent the energy in the shear modes $E(k_x = 0, k_z) = 0$ without a sink of energy. The time step of the simulations is limited by the Courant-Friedrichs-Levy (CFL) condition.

4.1 Effects of varying the stratification strength

In this section, I study the effects of varying the stratification strength $F_{h,f} = F/\gamma$ for a given value of the Reynolds number $Re_{8,f}$. We consider an anisotropic domain such that $L_x = 4L_z$, where $L_x = 2\pi$, and with a numerical resolution 3840×960 . The simulations have been initialized with the last state of a simulation with a lower resolution in order to reach faster the statistically stationary state. Figure 4.1 summarizes all numerical simulations in the parameter space $[F_{h,f}, Re_8]$. The simulations analyzed in this section are displayed in green. The marker shape represents the different numerical resolutions. Note that the markers do not follow a perfect horizontal line for a fixed numerical resolution. In section 3.6, I explained the procedure to compute the hyper-viscosity coefficient ν_8 . The coefficient ν_8 depends on each simulation. Nevertheless, we are rather interested in the order of magnitude of ν_8 than its value itself.

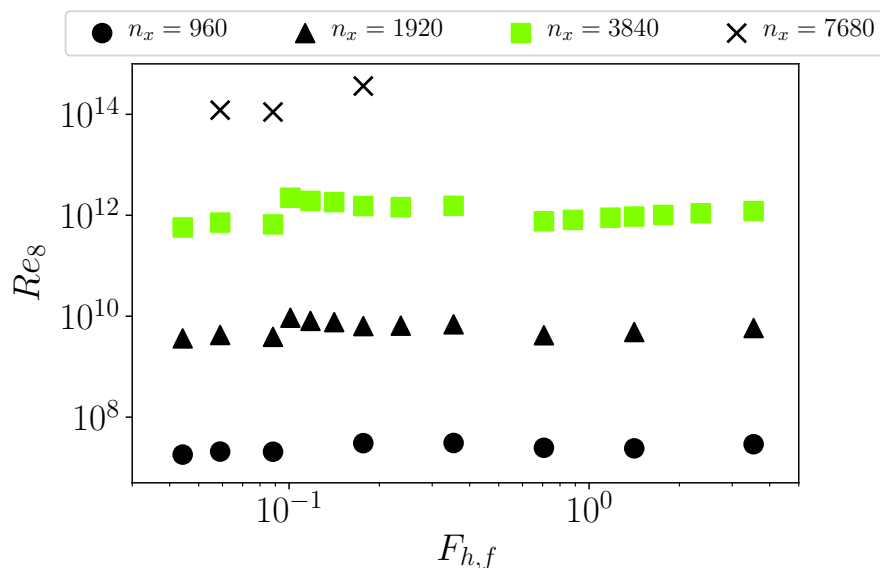


Figure 4.1: Summary of all runs in the parameter space $[F_{h,f}, Re_8]$. The marker shape represent the different resolutions: circle ($n_x = 960$); triangle ($n_x = 1920$); square ($n_x = 3840$); cross ($n_x = 7680$); diamonds ($n_x = 15360$). The simulations analyzed in this section are displayed in green.

Table 4.1 summarizes the numerical and physical parameters of all simulations in this section. In chapter 3, we have introduced the buoyancy k_b and Ozmidov k_o wavenumbers, respectively. As a reminder, the buoyancy scale $l_b = k_b^{-1}$ is interpreted as the displacement of a fluid particle with a characteristic velocity U in a background stratification characterized by N . The Ozmidov wavenumber k_o indicates the largest wavenumber influenced by the buoyancy. In all simulations, buoyancy scale is larger than the Ozmidov scale $k_o/k_b > 1$.

| γ | $F_{h,f}$ | $Re_{8,f}$ | ν_8 | $k_b/k_{f,z}$ | $k_o/k_{f,z}$ | k_o/k_b |
|----------|-----------|------------|----------|---------------|---------------|-----------|
| 0.2 | 3.54 | 1.2e+12 | 2.55e-23 | 0.2 | 0.5 | 2 |
| 0.3 | 2.36 | 1.1e+12 | 2.82e-23 | 0.4 | 1.0 | 2 |
| 0.4 | 1.77 | 1.0e+12 | 3.05e-23 | 0.6 | 1.5 | 2 |
| 0.5 | 1.41 | 9.4e+11 | 3.28e-23 | 0.8 | 2.1 | 3 |
| 0.6 | 1.18 | 9.0e+11 | 3.45e-23 | 1.0 | 2.8 | 3 |
| 0.8 | 0.88 | 8.1e+11 | 3.82e-23 | 1.2 | 4.3 | 3 |
| 1.0 | 0.71 | 7.6e+11 | 4.07e-23 | 1.1 | 6.0 | 5 |
| 2.0 | 0.35 | 1.5e+12 | 2.01e-23 | 1.4 | 16.9 | 12 |
| 3.0 | 0.24 | 1.4e+12 | 2.14e-23 | 1.7 | 31.0 | 18 |
| 4.0 | 0.18 | 1.5e+12 | 2.03e-23 | 2.0 | 47.7 | 24 |
| 5.0 | 0.14 | 1.8e+12 | 1.70e-23 | 2.2 | 66.7 | 31 |
| 6.0 | 0.12 | 1.9e+12 | 1.60e-23 | 3.1 | 87.6 | 28 |
| 7.0 | 0.10 | 2.2e+12 | 1.39e-23 | 2.7 | 110.4 | 41 |
| 8.0 | 0.09 | 6.6e+11 | 4.70e-23 | 3.3 | 134.9 | 41 |
| 12.0 | 0.06 | 7.2e+11 | 4.32e-23 | 4.3 | 247.8 | 57 |
| 16.0 | 0.04 | 5.7e+11 | 5.40e-23 | 5.9 | 381.6 | 64 |

Table 4.1: Overview of the physical and numerical parameters of the simulations for all simulations presented in this section. We vary the stratification strength $F_{h,f}$, i.e. γ , for a fixed forcing Reynolds number $Re_{8,f}$ with an hyper-viscosity coefficient ν_8 . k_b , k_o and $k_{f,z}$ are the buoyancy, Ozmidov and vertical forcing wavenumbers, respectively.

Figure 4.2 (left) shows the time evolution of the energy for different γ . The energy has been normalized by the quantity P/ω_{af} , which is the energy injected in one forcing period τ_{af} . The colors represent the value of the stratification strength γ , i.e. $F_{h,f}$. The error bars represent the standard deviation of the energy $\sigma_E = \sqrt{\langle(\bar{E} - E)^2\rangle_t}$. We see that the energy for all simulations seems to fluctuate around a value. This means that the energy at large scales has reached an statistically quasi-stationary state, for which the energy injection rate equals the mean dissipation rate $P \simeq \bar{\epsilon}$. Unlike 2D homogeneous turbulence, where no stationary state can be reached and with only small-scale dissipation, 2D stratified turbulence supports a mechanism to transfer energy from the forcing scale to small dissipative scales. For low values of $\gamma \in [0.2, 0.5]$, the statistically stationary state is reached considerably fast. When the stratification is increased, the stationary state is reached slowly. Furthermore, simulations with large γ present large fluctuations at the steady state (see red line in figure 4.2 corresponding to $\gamma = 8.0$). Figure 4.2 (right) displays the averaged energy at the steady state as function of the forcing horizontal Froude number $F_{h,f} = F/\gamma$. For large stratification strengths (brown and purple lines), the averaged energy is substantially large. In average, more energy is needed to transfer the energy to small scales. For $\gamma \in [4, 5, 6, 7, 8]$ (cyan, dark blue, orange, green and red lines), one can observe a flat zone, implying that the energy needed to transfer to small scales does not depend on the stratification. It has to be noticed that the minimum of energy is reached for $F_{h,f} \sim 1$. For the limit $\gamma \rightarrow 0$, the dynamics becomes similar to classical 2D turbulence with a passive scalar advected by the flow.

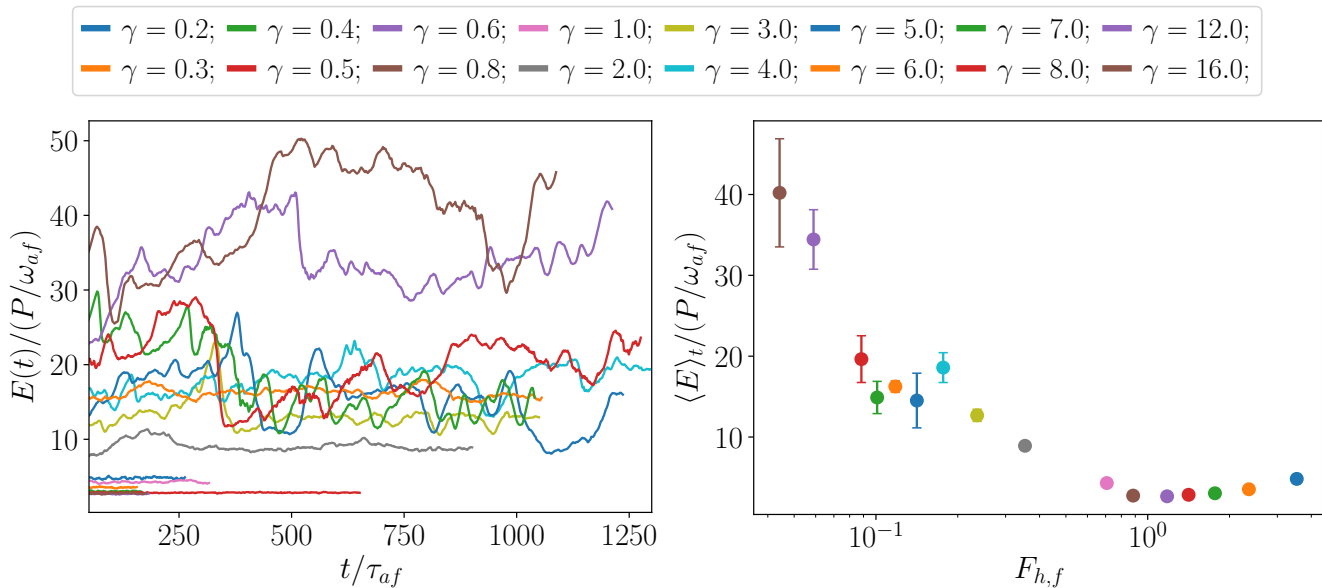


Figure 4.2: Time evolution of the averaged energy (left) and averaged energy as function of the horizontal forcing horizontal Froude number (right). In both graphs, the energy is normalized by P/ω_{af} , which is the injected energy in a forcing period τ_{af} . The colors represent the different values of the stratification strength γ . The error bars of the right plot represent the standard deviation of the energy $\sigma_E = \sqrt{\langle (\bar{E} - E)^2 \rangle_t}$

We have underlined that some studies of stratified turbulence used the horizontal Froude number F_h , which is the ratio between the stratification and non-linear time scales expressed as

$$F_h = \frac{U}{L_h N} \simeq \frac{P}{U^2 N}, \quad (4.2)$$

where U is the root mean square of the horizontal velocity and L_h is a characteristic horizontal scale. It is important to study how the forcing horizontal Froude number $F_{h,f} = F/\gamma$ scales with the original horizontal Froude number F_h . The ratio between both Froude numbers is expressed as

$$\frac{F_{h,f}}{F_h} = \frac{F U^2 N}{\gamma P}. \quad (4.3)$$

We consider that the averaged energy scales as the square of the velocity as $\langle E \rangle \sim U^2$, where U is a characteristic velocity. We can thus obtain the characteristic frequency of the forcing as $\omega_{af} = NF/\gamma$. We can express the equation (4.3) as

$$\frac{F_{h,f}}{F_h} \simeq \frac{\langle E \rangle}{P/\omega_{af}}. \quad (4.4)$$

The ratio of the Froude numbers $F_{h,f}/F_h$ is thus the normalized averaged energy displayed in figure 4.2 (right). Figure 4.3 displays the ratio $F_{h,f}/F_h$ as function of the forcing horizontal Froude number $F_{h,f}$. One can observe that $F_{h,f}$ scales as the original Froude number F_h for $\gamma \in [4, 5, 6, 7, 8]$. As mentioned above, at these stratification strengths, the averaged energy does not depend on the stratification strength (see figure 4.2, right). We need, in average, the same quantity of energy to transfer the energy to dissipative scales. For large values of γ , the scaling of equation 4.4 does not work, which might be due to too strong dissipation.

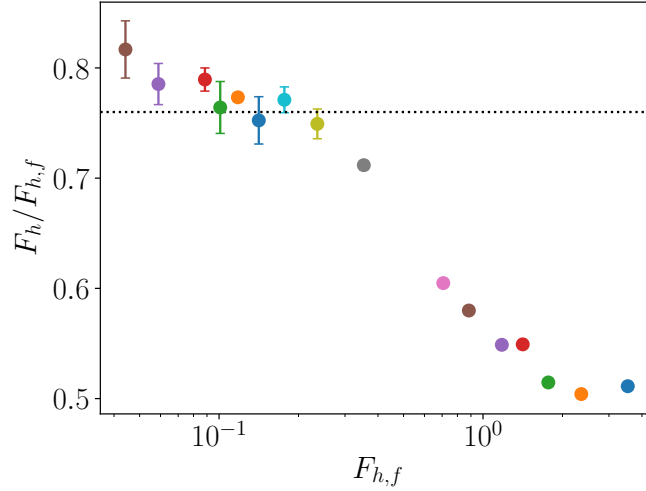


Figure 4.3: Ratio between the Froude numbers $F_h/F_{h,f}$ as function of the forcing horizontal Froude number $F_{h,f}$ for different stratification strengths γ . The horizontal black dotted line indicates where $F_h/F_{h,f}$ is constant.

Buoyancy fields at the steady state. Figure 4.4 displays the instantaneous fields of the quantity b/N at the statistically stationary state for six simulations: (a) $\gamma = 0.2$; (b) $\gamma = 0.5$; (c) $\gamma = 1.0$; (d) $\gamma = 2.0$; (e) $\gamma = 4.0$; (f) $\gamma = 8.0$. For low stratification strengths $\gamma \leq 1$, we observe the presence of scales with the same horizontal and vertical size, implying that the dynamics is isotropic. Furthermore, small scales are present in the flow. As it has been mentioned before, 2D stratified turbulence supports a transfer of energy towards small scale. Increasing the stratification strength γ , large horizontal layers emerge in the flow with small scales. Furthermore, the thickness of the horizontal layers decreases when we increase the stratification strength. For large stratification strengths $\gamma = 8$, the structures are considerably smoother with few small scales.

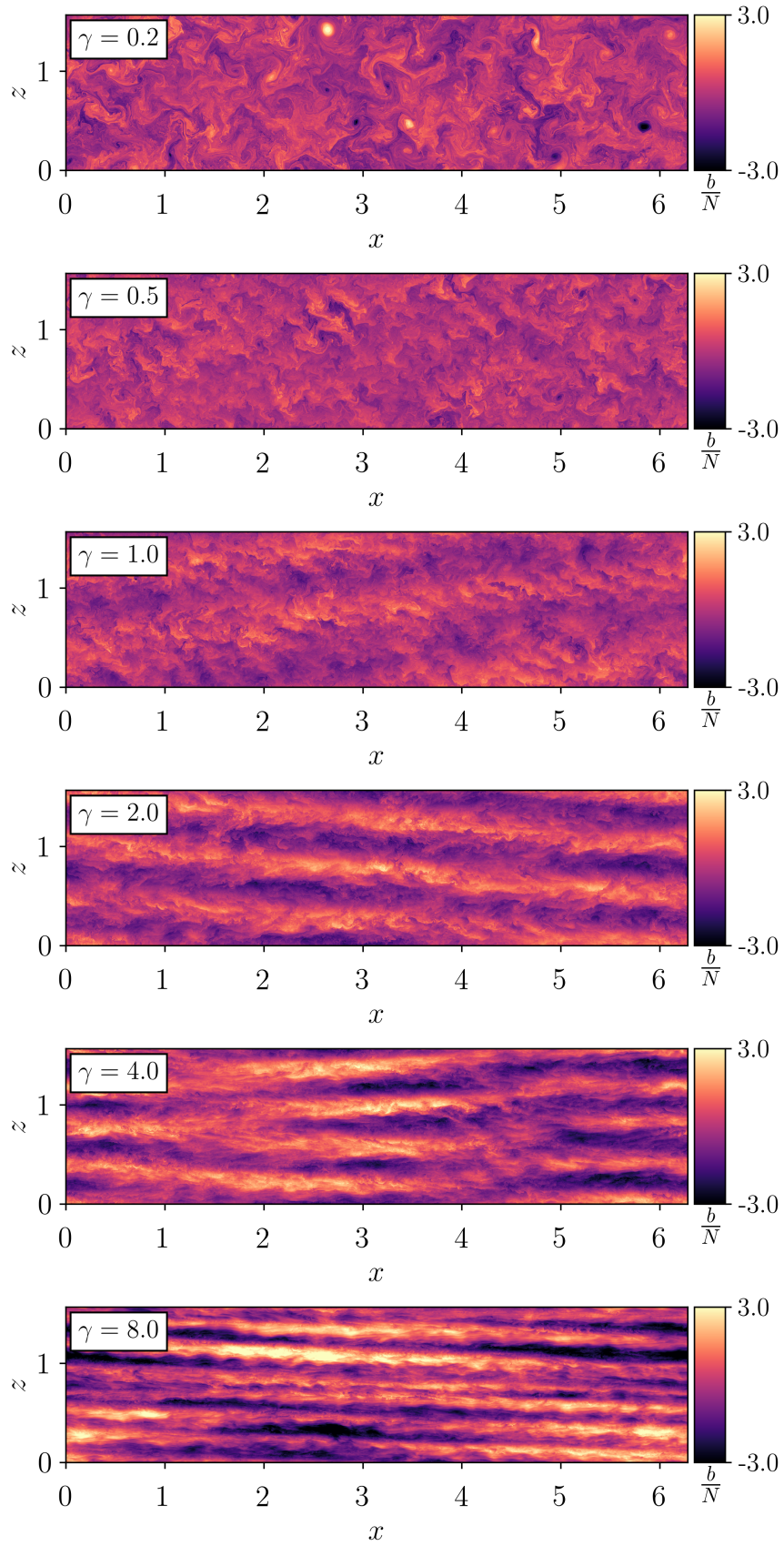


Figure 4.4: Snapshots of the quantity b/N in the statistically stationary state for six different values of γ .

Quantification of the large scale isotropy

In figure 4.4 and for low stratification strengths $\gamma \in [0.2, 0.5]$, we have seen scales with the same horizontal and vertical size, which means that the dynamics is isotropic. For a large stratification strength (see figure 4.4 for $\gamma \in [4.0, 8.0]$), the dynamics becomes layered with large horizontal scales and small vertical scales. The dynamics for large stratification strengths is indeed anisotropic. In order to quantify, in a simple way, the isotropy at large scales, I built an isotropy index \mathcal{I}_E defined as

$$\mathcal{I}_E = 4 \left(\frac{E_{K,x}}{E_K} - 1 \right)^2, \quad (4.5)$$

where $E_{K,x}$ is the horizontal component of the kinetic energy and E_K is the total kinetic energy. The value of the isotropy index is within the range $\mathcal{I}_E \in [0, 1]$. For isotropic flows the quantity $\mathcal{I}_E = 1$. For strongly anisotropic flows such as observed in figure 4.4 for $\gamma = 8$, the quantity $\mathcal{I}_E \simeq 0$. Figure 4.5 displays the isotropy index \mathcal{I}_E against the forcing horizontal Froude number $F_{h,f}$. The colors represent different values of the stratification strength γ . The error bars of \mathcal{I}_E are computed as $\delta\mathcal{I}_E \sim 2(\delta E_{K,x} + \delta E_K)$, where $\delta E_{K,x}$ and δE_K are the standard deviation of the horizontal kinetic energy and total kinetic energy respectively. For small γ , \mathcal{I}_E is constant of order unity. It means that for weak stratification strengths, the dynamics is isotropic at large scales, which is in agreement as observed in figure 4.4 for $\gamma \in [0.2, 0.5]$. At $\gamma \sim 0.8$ (brown dot), there is a transition on the value \mathcal{I}_E which starts decreasing, which means that the flow starts becoming anisotropic at large scales. This anisotropy at large scale is associated with the apparition of large horizontal layers observed in figure 4.4 for $\gamma = 1.0$. The quantity \mathcal{I}_E decreases with the stratification strength γ (see $\gamma \in [0.8, 1, 2]$ corresponding to brown, grey dots). For $\gamma \in [3, 4, 5]$ (corresponding to yellow, cyan and blue dots), we see that \mathcal{I}_E becomes constant. For large values of $\gamma \in [8, 12, 16]$ (corresponding to red, purple and brown dots), the quantity \mathcal{I}_E decreases with the stratification strength. It decreases faster than for $\gamma \in [0.8 - 2]$, which may be due to the effect of viscous dissipation. Flows with strong stratification, i.e. $\gamma \in [8, 12, 16]$ may be affected by the dissipation even for large horizontal scales. Viscosity damps vertical motions and enhances anisotropy at large scales.

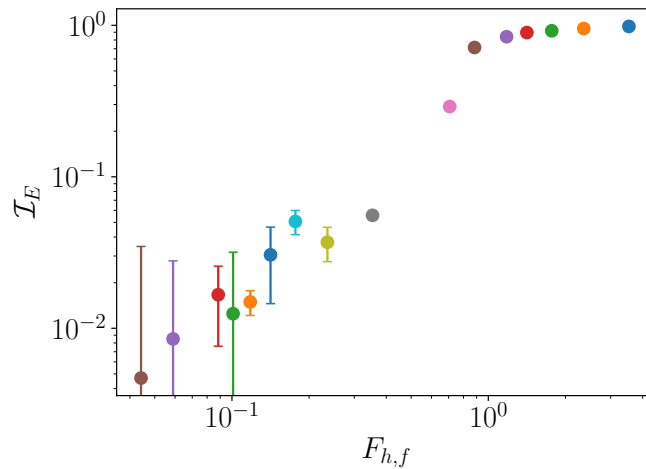
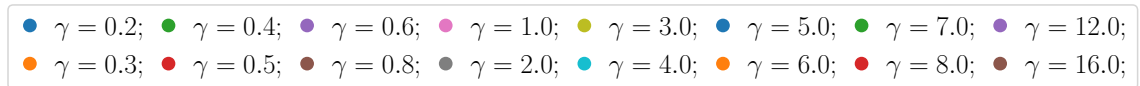


Figure 4.5: Isotropy index \mathcal{I}_E against the forcing horizontal Froude number $F_{h,f}$. The colors represent different stratification strengths γ .

Structure of the flow

We have seen in figure 4.5 that the flows become anisotropic when the stratification increases. It is therefore natural to study how the energy is distributed among the scales. Moreover, it is interesting to investigate if the energy is shared in the same way in the horizontal and vertical directions. In this section, I discuss the repartition of the energy among the scales by means of the horizontal and vertical energy spectra for different stratification strengths. We have seen in section 1.3.2 that the energy in the ocean is distributed differently in the horizontal and vertical directions, meaning that observed oceanic energy spectra are strongly anisotropic. Figure 4.6 displays the horizontal and vertical energy spectra for three different stratification strengths: weakly stratified flows $\gamma = 0.5$ (figure 4.6 (a)), intermediate stratified flows $\gamma = 2.0$ (figure 4.6 (b)) and strongly stratified flows $\gamma = 8.0$ (figure 4.6 (c)). The energy spectra are compensated by the power law $k^{-5/3}$. The kinetic and potential energy are represented by the orange and blue lines, respectively. The solid lines represent the horizontal energy spectra and the dashed lines represent the vertical energy spectra. The dashed black lines represent the power laws $k^{-5/3}$ and k^{-3} . The red dashed line displays the model $C_1 UN k_z^{-2}$, where $C_1 = 0.02$. This scaling will be discussed later in figure 4.7. The dotted vertical lines correspond to the buoyancy k_b and the Ozmidov k_o wavenumbers. The vertical grey band shows the forcing region.

For weakly stratified flows $\gamma = 0.5$ (figure 4.6 (a)), we see that the solid lines superpose the dotted lines. It means that the horizontal and vertical energy spectra are similar, which confirms that the flow is isotropic. For low γ , the forcing horizontal Froude number $F_{h,f}$ is of order of the unity. For scales smaller than the forcing scale $k \gg k_f$, one can observe that the potential energy (blue lines) dominates over the kinetic energy (orange lines). For moderate stratification strengths $\gamma = 2.0$ (figure 4.6 (a)), one can notice that the horizontal (solid lines) and vertical (dashed lines) energy spectra are not superposed. This confirms that the dynamics is anisotropic as observed in figures 4.4 and 4.5. For the horizontal energy spectra, we observe a peak at the first horizontal mode $k_x = \delta k_x$, where $\delta k_x = 2\pi/L_x$, which corresponds to the size of the large horizontal layers observed in figure 4.4 for $\gamma = 2.0$. In chapter 3, it has been mentioned that we prevent the energy to go to the shear modes ($k_x = 0, k_z$) in order to avoid concentration of energy in the shear modes. The energy is thus transferred to the first horizontal mode $k_x = \delta k_x$. Furthermore, at low wavenumbers $k_x < k_{f,x}$, there is an equipartition of kinetic (orange solid line) and potential energies (blue solid line). In the vertical energy spectra (dashed lines), we observe a peak within the forcing region, which might correspond to the thickness of the large horizontal scales. The potential energy is transferred following a power law slightly shallower than k_x^{-2} . It has to be noticed, in both vertical and horizontal spectra, that there is a transition at the Ozmidov wavenumber $k \sim k_o$. At scales smaller than the Ozmidov scale $k > k_o$, the potential energy (blue lines) predominate over the kinetic energy (orange lines).

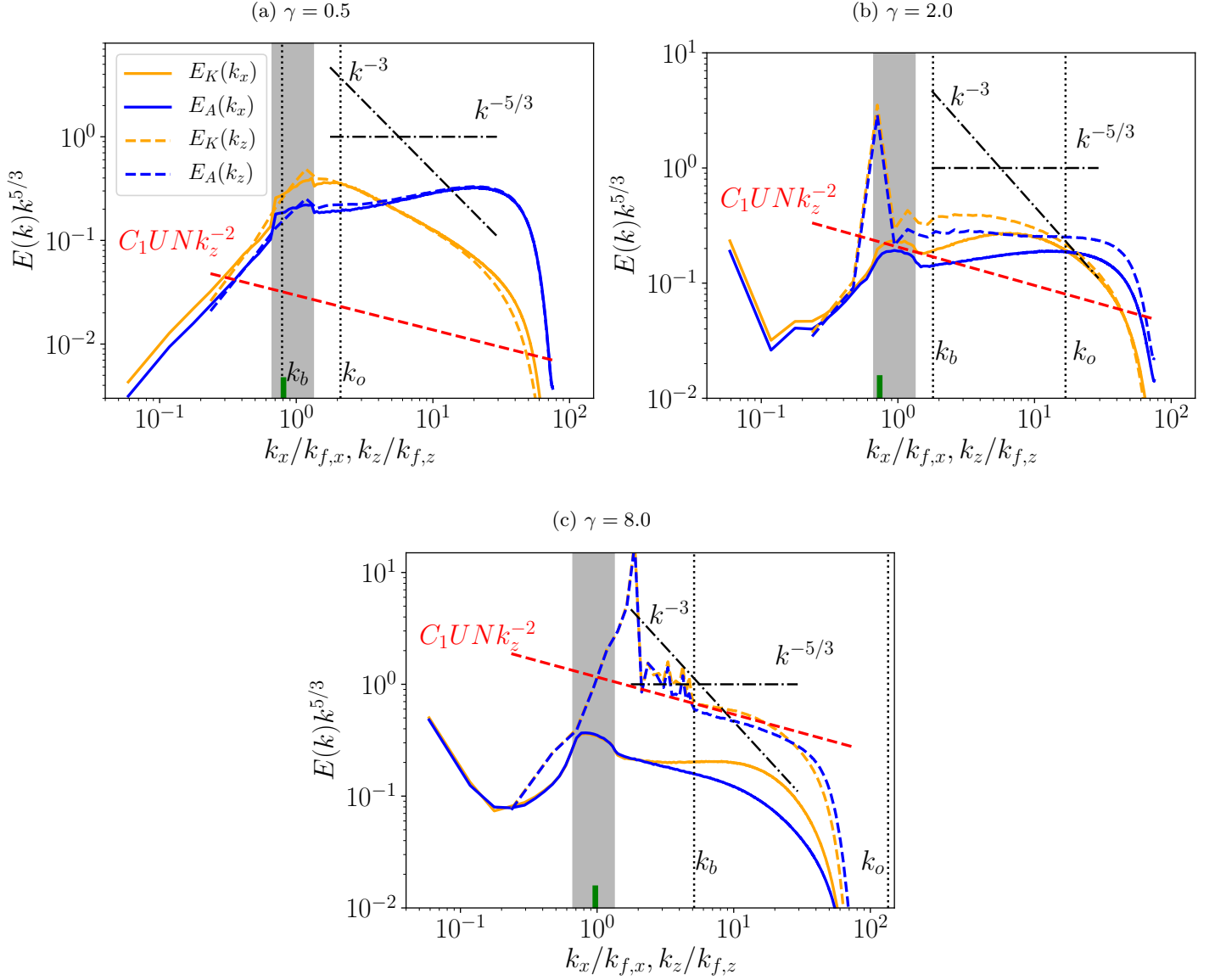


Figure 4.6: Horizontal (solid-line) and vertical (dashed-line) energy spectra for three different stratifications: (a) $\gamma = 0.5$; (b) $\gamma = 2.0$; $\gamma = 8.0$. The numerical resolution of the simulations is 3840×960 . The energy spectra is compensated by a power law $k^{5/3}$. The orange line represents the kinetic energy spectra. The blue line represents the potential energy spectra. The dashed black lines represents the power laws $k^{-5/3}$, k^{-2} and k^{-3} . The dotted vertical lines are the buoyancy k_b and the Ozmidov k_o wavenumbers. The vertical grey band represents the forcing region. The red dashed line is the represents the analytical expression of $E(k_z) = C_1 UN k_z^{-2}$, where $C_1 = 0.02$. The small vertical green line corresponds to the characteristic vertical wavenumber.

For large stratification strengths $\gamma = 8$ (figure 4.6 (c)), we see that the horizontal and vertical energy spectra are substantially different, which means that the flow is strongly anisotropic. In the horizontal energy spectra, we observe an equipartition of the kinetic (orange solid line) and potential (blue solid line) energies at large scales observed in figure 4.6 (b). It suggests the presence of internal gravity waves with a large horizontal scale. For $k_x > k_{f,x}$, both kinetic and potential energy spectra seem to decay as the power law k_x^{-2} , suggesting a transfer of energy carried by waves. For large k_x , the kinetic energy spectrum seems to follow a $k_x^{-5/3}$ power law. We now focus on the vertical energy spectra (dashed lines). The peak of the vertical energy spectra is on the right of the forcing scale $k > k_{f,z}$. As it has been mentioned before, the peak corresponds to the thickness of these horizontal layers which decreases when the stratification strength increases. However, the vertical energy spectra seem to decay as the power-law k_z^{-2} , we do not see a clear break on its slope. It might be due to the fact that the dynamics is strongly affected by the viscosity. We may need a larger Reynolds number simulations in order to increase the width of the inertial range. Larger Reynolds flows are discussed later in section 4.5.

As it has been mentioned above, the vertical energy spectra for large stratification strengths follows a k_z^{-2} power law (figure 4.6 (c)). It is therefore interesting to built an expression for the decrease of the vertical energy spectra in the strongly stratified regime. By dimensional arguments, the vertical energy spectra scales as $E(k_z) = C_1 UN k_z^{-2}$, where the constant C_1 is obtained by fitting the expression with the vertical energy spectra for $\gamma = 8.0$. The value of the constant obtained is $C_1 = 0.02$. In figure 4.7, we test the expression of the vertical energy spectra for different stratification strengths. One can observe that the analytical expression only works for $\gamma \in [4, 5, 6, 7]$. For a low stratification strength $\gamma = 3.0$, the analytical expression does not work. It may be explained by the fact the flow is weakly affected by the stratification. For a large stratification strength $\gamma = 12.0$, the analytical scaling does not work, which may be explained by the fact that the flow is strongly affected by the dissipation.

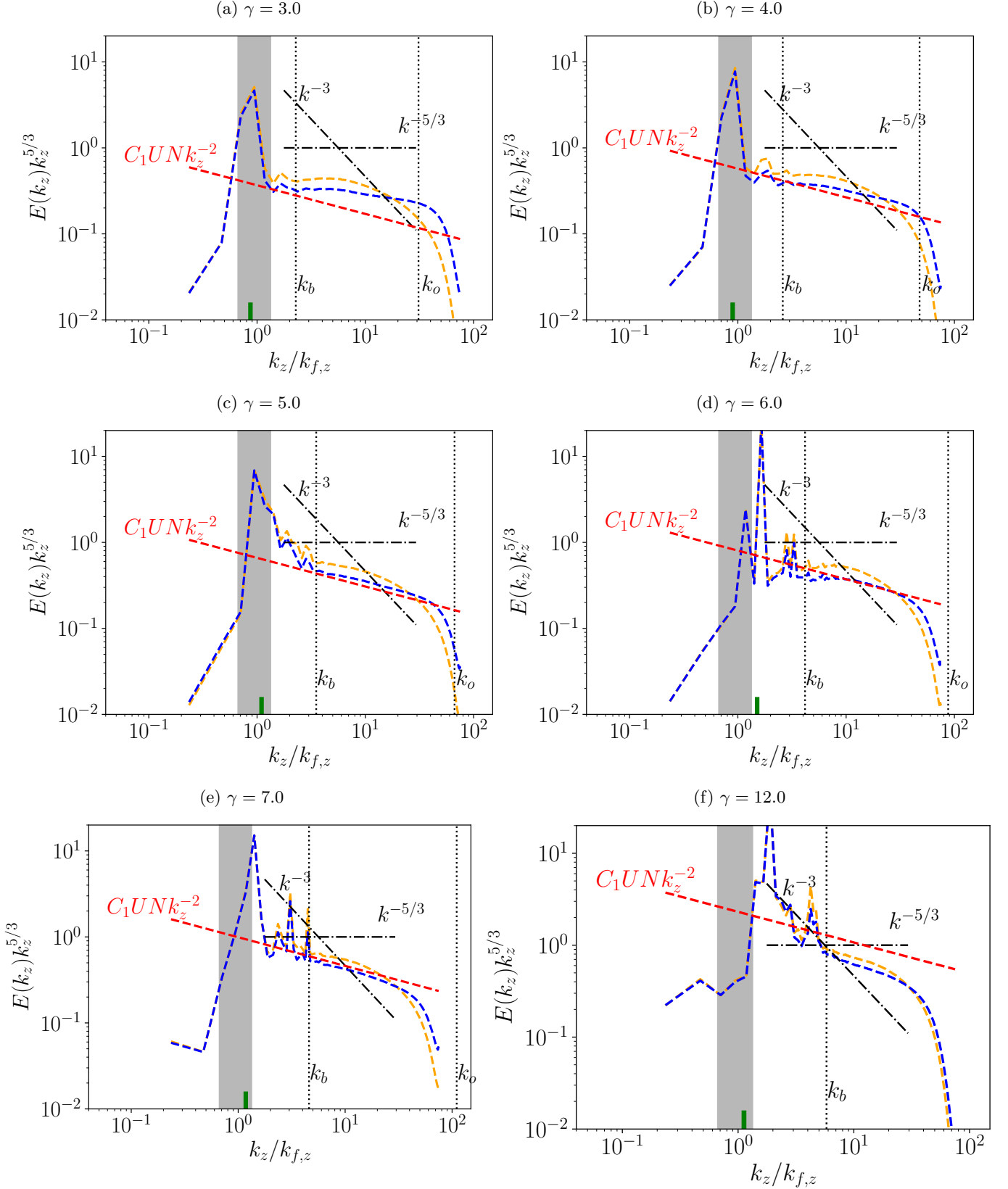


Figure 4.7: Vertical energy spectra for six different stratification strengths: (a) $\gamma = 3.0$, (b) $\gamma = 4.0$, (c) $\gamma = 5.0$, (d) $\gamma = 6.0$, (e) $\gamma = 7.0$ and (f) $\gamma = 12.0$. The orange line is the kinetic energy spectrum. The blue line is the potential energy spectrum. The red dashed line is the represents the analytical expression of $E(k_z) = C_1 UN k_z^{-2}$, where $C_1 = 0.02$. The dashed black lines represents the power laws $k^{-5/3}$, k^{-2} and k^{-3} . The dotted vertical lines are the buoyancy k_b and the Ozmidov k_o wavenumbers. The vertical grey band represents the forcing region.

Spectral energy budget

In this section, we study the energy transfer mechanisms by means of the spectral energy budget. I have computed the spectral energy fluxes for three stratification strengths: $\gamma = 0.5$, $\gamma = 2.0$ and $\gamma = 8.0$. Figure 4.8 displays the horizontal (left) and vertical (right) spectral energy budget. The flux $\Pi(k)$ is normalized by the mean energy dissipation ϵ . The orange and blue lines represent the kinetic Π_K and potential Π_A energy fluxes, respectively. The black dotted line represents the total energy flux $\Pi = \Pi_K + \Pi_A$. The green line represents the spectral dissipation.

For weakly stratified flows (figure 4.8, (a) and (b)), we see that the horizontal (a) and vertical (b) fluxes are similar. For wavenumbers larger than the forcing wavenumber $k > k_f$, the black dotted and blue lines are positive, and orange line is negative. This fact means that energy is transferred from the injection scale to smaller scales. The fact that the configuration is 2D, the kinetic energy carries energy from smaller scales to larger scales. This type of dynamics generates a flux loop already observed in Boffetta et al. (2011). For moderate and strongly stratified flows (figures 4.8 (c), (d), (e) and (f)) the mechanism of energy transfer is different. We observe that horizontal and vertical components of the spectral energy budget are different, which confirms that the flow is anisotropic. We now focus on the horizontal energy flux (figures 4.8 (c) and (e)). For modes with wavenumber smaller than the forcing wavenumber $k < k_f$, the potential (blue) and kinetic (orange) fluxes are the same with opposite sign. This fact means that when injecting energy, a first loop at large scales is created. The kinetic energy is transferred from the injection scale to large scales. At large scales there is a conversion to potential energy that carries energy to smaller scales. For wavenumbers larger than the forcing wavenumber $k > k_f$, the orange line becomes positive in a small region of the spectral space. Analogously as the weak stratified flows, a second flux loop is created for wavenumbers larger than the forcing wavenumbers $k > k_f$. The energy is transferred to smaller scales by the potential energy (blue line). The kinetic energy transfers back the energy from small to large scales (blue line). It has to be noticed that for strongly stratified flows, i.e. $\gamma = 8.0$, the black dotted line can not reach an horizontal plateau, which means that the dynamics is strongly affected by the viscosity and the Reynolds number is too low to develop a clear inertial range on the horizontal direction. Thus, the horizontal resolution must be further increased. In the vertical energy flux (figures 4.8 (d) and (f)), the transfer of energy is similar as of the weakly stratified flows. There is a direct cascade of energy from the injection scale to dissipative scales. The cascade of energy is dominated by the potential energy. A flux loop is also present. The kinetic energy is pumping back energy to large scales.

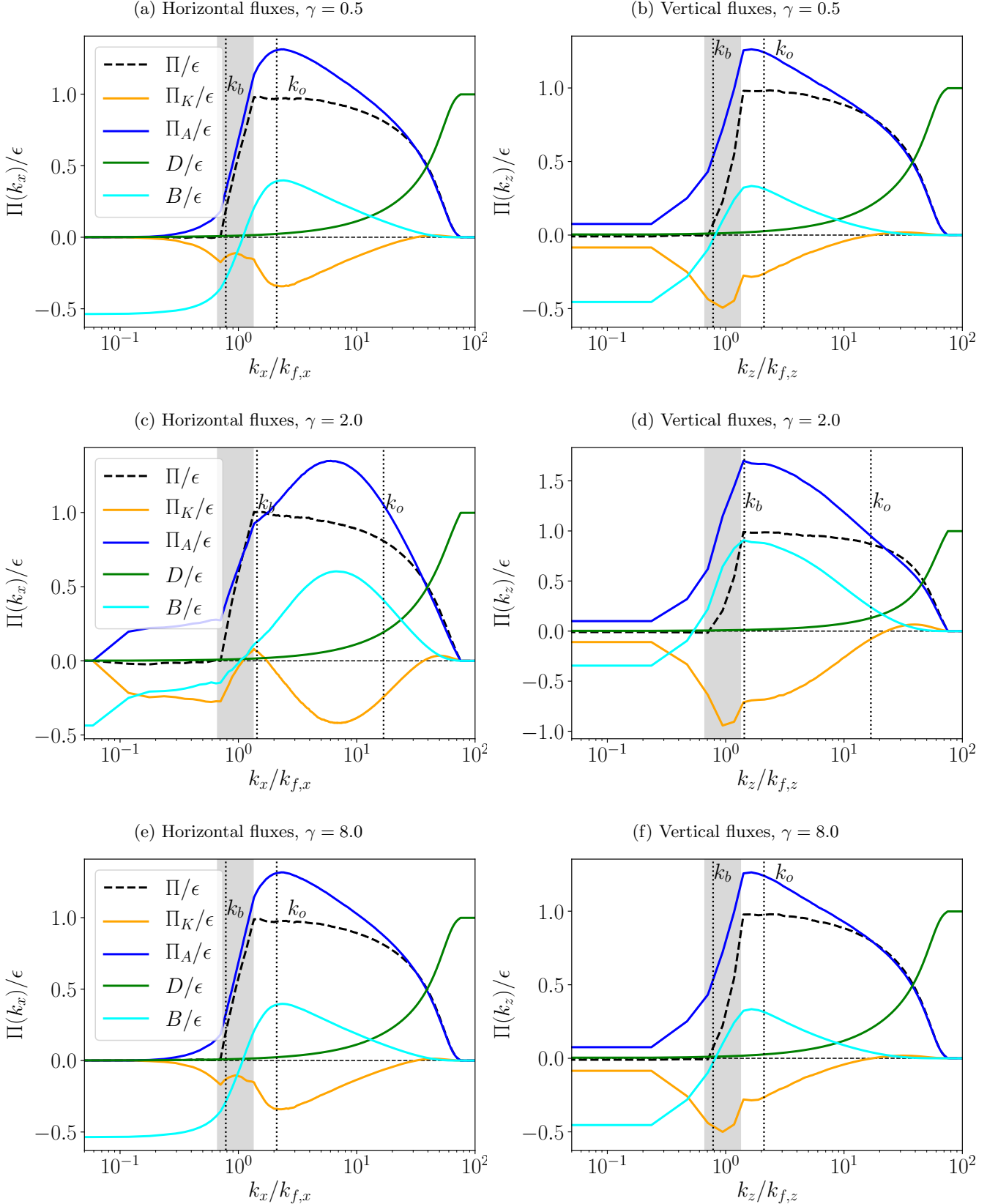


Figure 4.8: Horizontal (b) and vertical (b) spectral energy fluxes and dissipation for $\gamma = 0.5$, $\gamma = 2$ and $\gamma = 8$. The flux and dissipation are normalized by the mean dissipation rate of energy ϵ . The orange line represents the flux of kinetic energy Π_K . The blue line represents the flux of potential energy Π_A . The black dotted line represents the flux of the total energy Π . The green line represents the dissipation of total energy D . The cyan line represents the conversion from kinetic to potential energy B . The vertical grey band represents the forcing region.

Quantification of the isotropy at dissipative scales

In figures 4.8 (e) and (f), we have seen that the dynamics were strongly affected by the dissipation for $\gamma = 8.0$. For strongly stratified flows, the dissipation occurs at large horizontal scales and small vertical scales, meaning that it is strongly anisotropic. In order to quantify the isotropy of the dissipative scales, we have build a non-dimensional quantity \mathcal{I}_d computed as

$$\mathcal{I}_d = \frac{k_{1/2,x}}{k_{1/2,z}}, \quad (4.6)$$

where $k_{1/2,x}$ and $k_{1/2,z}$ are the wavenumbers at which the dissipation is half of the total dissipation in the horizontal and vertical directions respectively. For flows with $\mathcal{I}_d \sim 1$ means that half of the dissipation occurs at the same wavenumber for horizontal and vertical directions. In this case, the dissipation is isotropic. For flows with $\mathcal{I}_d \sim 0$, half of the dissipation operates at vertical wavenumbers larger than at the horizontal wavenumbers. This means that the dissipation is anisotropic. In figure 4.9, the isotropy of the dissipation \mathcal{I}_d is displayed against the forcing horizontal Froude number $F_{h,f}$. We first focus on large values of $F_{h,f}$, i.e. weakly stratified flows. The quantity \mathcal{I}_d is constant and is of order of the unity. It means that the dissipation is isotropic at flows weakly affected by the stratification. A transition appears for a value of $\gamma = 0.8$ corresponding to the brown dot. The isotropy of the dissipation starts decreasing as the $F_{h,f}$ decreases. When we increase the stratification strength, the flow develops into large horizontal layers. As it has been observed in figure 4.4 for $\gamma = 4.0$, the flows contains large horizontal layers coupled with small vertical scales. These small vertical scales might be produced due the strong shear between the horizontal layers. For strongly stratified flows, $F_{h,f} < 10^{-1}$ corresponding to red, purple and brown dots, the \mathcal{I}_d decays faster than for weaker stratifications when decreasing $F_{h,f}$. The dissipation in strongly stratified flows enhances the anisotropy of the dissipation. It has to be noticed that there are three different scalings for the quantity \mathcal{I}_d : stratified flows affected by the dissipation, stratified flows weakly affected by the dissipation and weakly stratified flows.

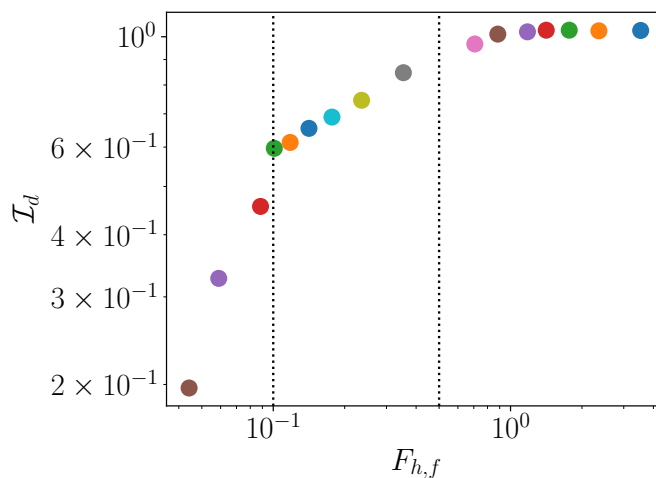
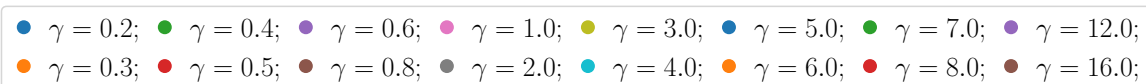


Figure 4.9: Isotropy of the dissipation \mathcal{I}_d against the forcing horizontal Froude number $F_{h,f}$. The numerical resolution of the simulations is 3840×960 . The dotted vertical lines indicate the break of the slope of \mathcal{I}_d .

Vertical structure of the strongly stratified flows

In the limit of the strong stratification, the vertical scale of the flow has two different scalings (see chapter 2). Flows weakly affected by the viscosity develop layers with a thickness proportional to the buoyancy length scale. Flows strongly affected by the viscosity develop a vertical scale proportional to the Reynolds number. In this section, the two scalings are tested for different stratification strengths.

Characteristic horizontal and vertical scales of the flow

The characteristic horizontal and vertical scales of the flow is computed following the work of Brethouwer et al. (2007) as

$$l_x = \left[\frac{\int_0^\infty E_K(k_x) dk_x}{\int_0^\infty k_x^m E_K(k_x) dk_x} \right]^{1/m} \quad l_v = \left[\frac{\int_0^\infty E_K(k_z) dk_z}{\int_0^\infty k_z^m E_K(k_z) dk_z} \right]^{1/m}, \quad (4.7)$$

where $E_K(k_x)$ and $E_K(k_z)$ are the horizontal and vertical kinetic energy spectra respectively. I make the choice of $m = 1$, which requires that $E_K(k_z)$ falls faster than k_z^{-2} (see appendix B of Brethouwer et al. (2007)). For strongly stratified flows, i.e. large γ , I expect the vertical kinetic energy spectra $E_K(k_z)$ to fall off faster than k_z^{-2} (see figure 4.6 (c)).

A. Scaling for turbulent stratified flows

Billant, Chomaz (2001) proposed a scaling for the layer thickness for strongly stratified inviscid flows. They argued that, in the limit of strong stratification $F_h \rightarrow 0$, the flow adjusts its vertical length scale to the buoyancy length scale $l_v \sim l_b \sim U/N$, where l_v and l_b are the vertical and buoyancy length scales respectively, U is a characteristic horizontal velocity and N is the Brunt-Väisälä frequency.

B. Scaling for viscosity-affected stratified flows

For strongly viscosity-affected flows, Godoy-Diana et al. (2004) argued that the vertical length scale is determined by the balance between the horizontal advection term and the vertical diffusion term of the equation (2.39). The vertical length scale can thus be expressed as $l_v \sim l_{\nu_8} \sim l_h Re_8^{-1/8}$, where l_h is the horizontal characteristic scale and Re_8 is the Reynolds number with the hyper-viscosity coefficient ν_8 .

Test of the two scalings

Figure 4.10 (a) displays the vertical wavenumber $k_v \sim 1/l_v$, (b) the buoyancy wavenumber $k_b = N/U$, (c) the compensated vertical wavenumber k_v with the viscosity scaling $k_{\nu_8} \sim 1/l_{\nu_8}$ and (d) the compensated vertical wavenumber k_v with the buoyancy wavenumber k_b for different values of stratification strength, i.e. F_h . We now focus on figure 4.10 (a). For small values of F_h , its vertical characteristic wavenumber is relatively large. Indeed strongly stratified flows have a small characteristic vertical scale (see $\gamma = 8.0$ of figure 4.4). One can notice that the characteristic vertical wavenumber k_v decreases when decreasing the stratification strength $F_{h,f} > 1$. When decreasing the stratification, the dynamics starts becoming isotropic. Its vertical scale starts increasing and becomes similar to the characteristic horizontal scale (see figure 4.10 (b)). We now test the two scalings proposed for strongly stratified flows: viscosity-affected stratified flows (figure 4.10 (c)) and strongly turbulent stratified flows (figure 4.10 (d)). In figure 4.10 (c), we see that for values $F_{h,f} < 10^{-1}$, the values of k_v are aligned around the value $k_v/k_{\nu_8} \sim 2 \times 10^{-2}$ although the scaling is not very clear. It means that the viscous scaling works for flows

with strong stratification. At this numerical resolution, strong stratified flows are still highly dissipative. One can notice that when decreasing stratification, i.e large values of F_h , the scaling is not valid. For weak stratifications, the flows become isotropic and strongly non-linear. They are not affected by the viscosity. We now focus on figure 4.10 (d). For values $F_{h,f} \sim 0.3$, the compensated vertical wavenumber k_v/k_b is constant and of order of $k_v/k_b \sim 0.4$. The strongly stratified and turbulent scaling only works in this range of flows at this fixed numerical resolution 3840×960 . When increasing the stratification, i.e lower values $F_{h,f}$, the scaling does not work any longer. It is due to the viscosity effects. The flows are strongly affected by the viscosity effects. They can only develop layers with a thickness larger than the buoyancy length scale $l_b = U/N$.

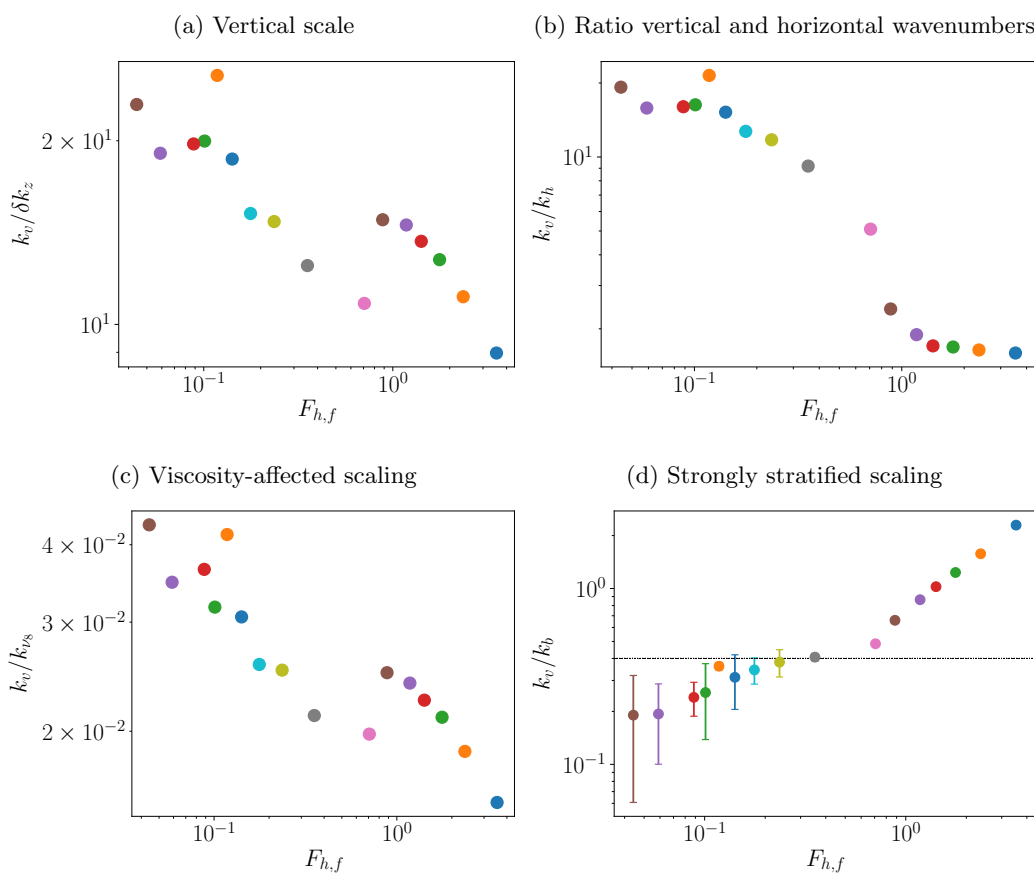
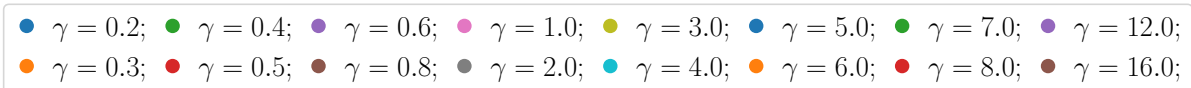


Figure 4.10: (a) Characteristic vertical wavenumber k_v computed as Brethouwer et al. (2007); (b) characteristic buoyancy wavenumber $k_b = N/U$; (c) compensated vertical wavenumber k_v with the viscosity-affected wavenumber $k_{\nu 8}$; (d) compensated vertical wavenumber k_v with the buoyancy wavenumber k_b . All the quantities are plotted as function of the forcing horizontal Froude number $F_{h,f}$. The colors represent the strength of stratification γ . The numerical resolution of all simulations is 3840×960 .

Instability mechanism and the Richardson number

In figure 4.4 for $\gamma \in [4.0, 8.0]$, we have seen that the dynamics is strongly anisotropic. Large horizontal layers are coupled with small vertical scales. The production of these small vertical scales might be due to the strong shear between the horizontal layers. It is therefore important to quantify the development of shear instabilities in the flow. The shear instability, also called Kelvin-Helmholtz (KH) instability, is the overturning of a shear layer. The non-dimensional number that quantifies the KH instability locally is the Richardson number Ri . It locally compares the shear the vertical shear with the stratification. It is defined as

$$Ri = \frac{-\frac{g}{\rho_0} \frac{\partial \rho}{\partial z}}{|\partial_z u_x|^2}. \quad (4.8)$$

It has to be noticed that the flow is unstable for $Ri < 0$ by gravitational instability. The flow potentially develop shear instabilities for $0 < Ri < 1/4$ (Miles, 1961). For $Ri > 1/4$, the stratification damps the shear of the flow. Figures 4.11 display snapshots of the Richardson number Ri for $\gamma = 0.2$ and $\gamma = 0.5$, i.e. weakly stratified flows. The top figure shows the Richardson number Ri for the whole domain size. The bottom figure displays the Richardson number of a zoomed region. The colorbar has been fixed in the range where a shear instability potentially can develop $0 < Ri < 1/4$. In figure 4.11, the critical Richardson number $Ri < 1/4$ is reached everywhere. For weakly stratified flows, the strength of the stratification is not enough to damp the shear produced by the vorticity field.

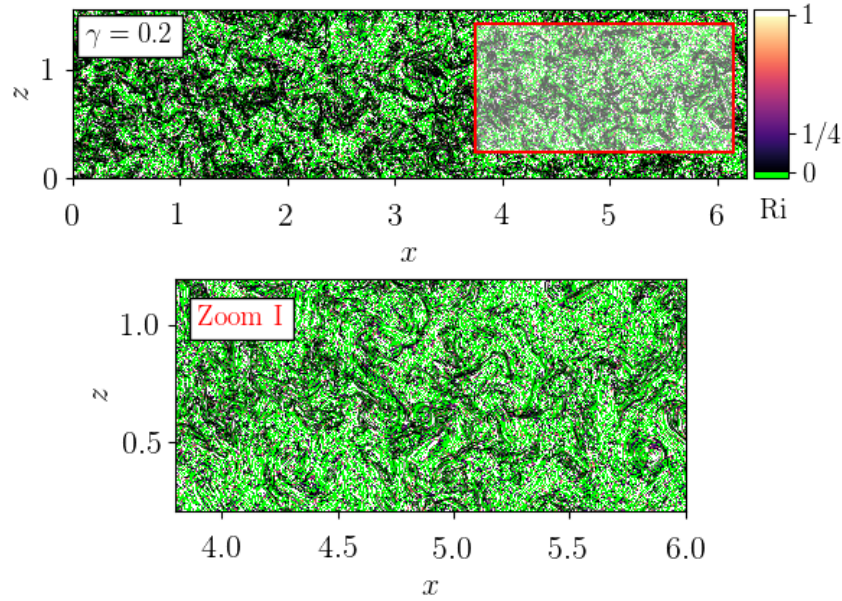


Figure 4.11: Local Richardson number Ri for $\gamma = 0.2$. The green color displays the unstable regions with $Ri < 0$. The red rectangle shows the zoom region. The numerical resolution is 3840×960 .

Figure 4.12 displays the Richardson number Ri for $\gamma = 1.0$. We have seen that for $\gamma = 1.0$ the flow starts showing in large horizontal layers (see figure 4.4 for $\gamma = 1.0$). We see that the critical Richardson number $0 < Ri < 1/4$ is disposed in horizontal layers. These layers where the Richardson number is critical correspond to the interface between the horizontal layers observed in figure 4.4 for $\gamma = 1.0$.

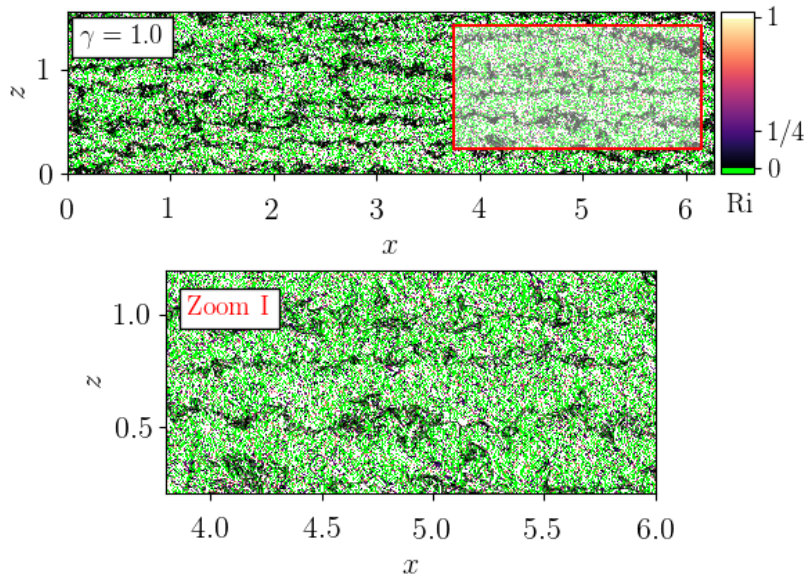


Figure 4.12: Same as figure 4.11 for $\gamma = 1.0$

For strongly stratified flows, figures 4.13- 4.14, the Richardson number is disposed in horizontal layers with a thickness smaller than for $\gamma = 1.0$. It is due to the fact that the horizontal layers in the physical fields decreases with the stratification. This fact has been already observed in figure 4.4 for $\gamma = 8.0$. The critical Richardson number $0 < Ri < 1/4$ appears again at the interface of these large horizontal layers. A strong shear appears at the interface of these horizontal layers developing shear instabilities.

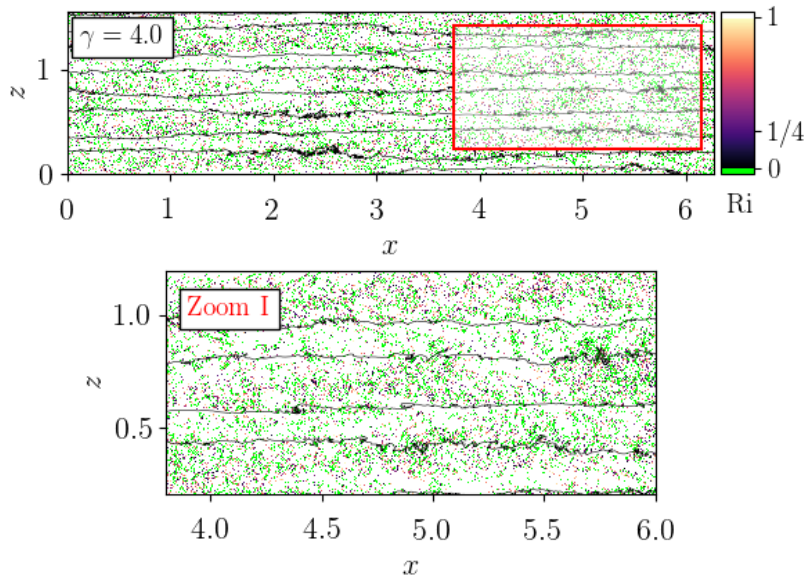


Figure 4.13: Same as figure 4.11 for $\gamma = 4.0$

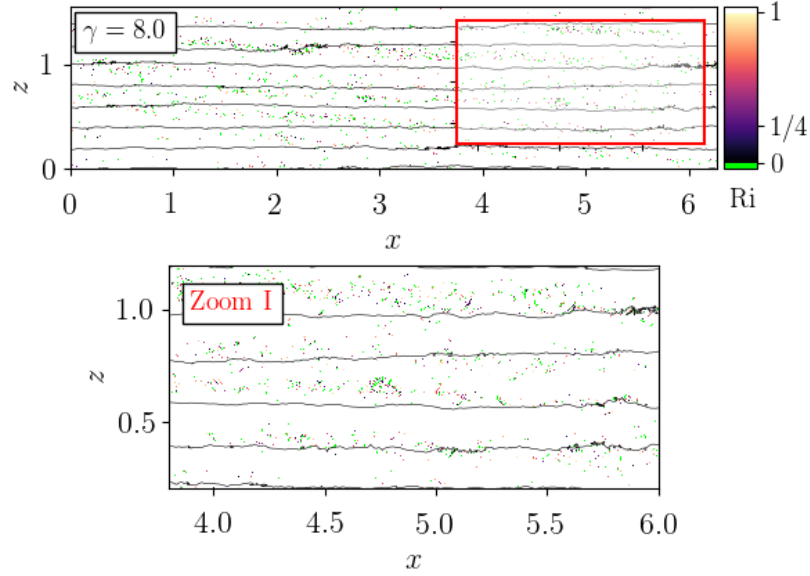


Figure 4.14: Same caption as figure 4.11 for $\gamma = 8.0$

Summary of 4.1: effects varying the stratification strength

In this section, we have performed numerical simulations of 2D stratified turbulence with different stratification strengths for a fixed Reynolds number. We have observed three different regimes depending on the value of the forcing horizontal Froude number $F_{h,f}$. The three regimes are listed in the following:

- $F_{h,f} \geq 0.5$. Isotropic stratified turbulence with a forward energy cascade towards small scales. There is only one flux loop at small scales.
- $0.1 \leq F_{h,f} < 0.5$. Anisotropic stratified turbulence with horizontal scales weakly affected by the viscosity. Its vertical scale is of order the buoyancy scale $l_v \sim l_b$. Two flux loops are observed at large and small scales respectively.
- $F_{h,f} < 0.1$. Anisotropic stratified turbulence with horizontal scales strongly affected by the viscous dissipation.

Geophysical flows such as the atmosphere and the oceans are strongly stratified flows, i.e. with low horizontal Froude number. We need thus to increase the Reynolds number in order to investigate the dynamics of these flows. In the following section, we study the dynamics of stratified turbulence for different Reynolds numbers by varying the numerical resolution.

4.2 Effects of varying the Reynolds number

Increasing the Reynolds number of the flow results in a dynamics less affected by the viscosity. We increase the Reynolds number by increasing the horizontal numerical resolution n_x , which decreases the optimal hyper-viscosity coefficient ν_8 . The dependency of the hyper-viscosity coefficient ν_8 and the horizontal numerical resolution has been already discussed in section 3.6. In this section, I discuss the effect on the dynamics of varying the Reynolds number $Re_{8,f}$ for a given stratification strength $F_{h,f}$. We present numerical simulations with four different numerical resolutions $n_x \in [960, 1920, 3840, 7680]$. I choose those simulations with a large stratification strength $\gamma = 8.0$. Furthermore, simulations with $n_x \in [960, 1920, 3840]$ have a domain size $L_x = 4L_z$. The anisotropy of the domain for simulations $n_x = 7680$ is $L_x = 16L_z$. Figure 4.15 displays the parameter space $[F_{h,f}, Re_{8,f}]$ for all runs. The numerical simulations with a value $\gamma = 8.0$ are displayed in green. The table 4.2 summarizes the numerical and physical parameters of all simulations presented in this section.

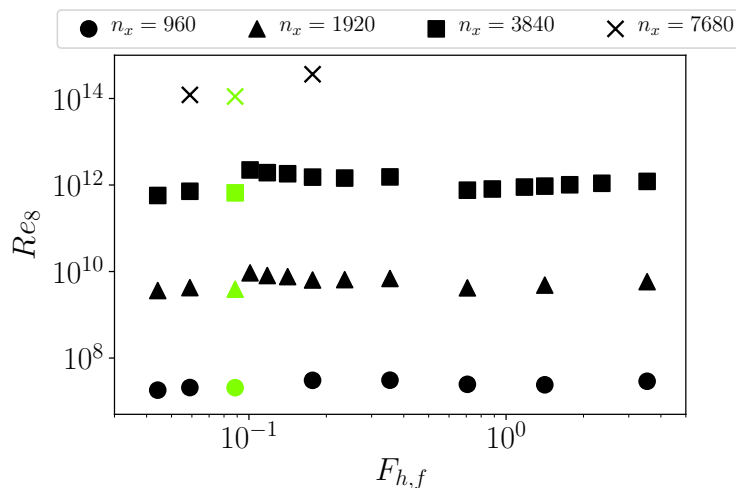


Figure 4.15: Same as figure 4.1. In this section, I analyze the effect of varying the Reynolds number $Re_{8,f}$ for a given stratification strength $F_{h,f} = 0.09$ ($\gamma = 8.0$). The simulations analyzed in this section are displayed in green.

| $n_x \times n_z$ | $Re_{8,f}$ | ν_8 | γ | $F_{h,f}$ | $k_b/k_{f,z}$ | $k_o/k_{f,z}$ | k_o/k_b |
|------------------|------------|----------|----------|-----------|---------------|---------------|-----------|
| 960 × 240 | 2.1e+07 | 1.50e-18 | 8.0 | 0.09 | 3.1 | 135 | 44 |
| 1920 × 480 | 3.9e+09 | 7.93e-21 | 8.0 | 0.09 | 3.3 | 135 | 41 |
| 3840 × 960 | 6.6e+11 | 4.70e-23 | 8.0 | 0.09 | 3.3 | 135 | 41 |
| 7680 × 480 | 1.1e+14 | 2.78e-25 | 8.0 | 0.09 | 4.7 | 135 | 29 |

Table 4.2: Overview of the physical and numerical parameters of the simulations with a fixed stratification strength $\gamma = 8.0$. I vary the Reynolds number $Re_{8,f}$. The forcing horizontal Froude number is expressed as $F_{h,f}$. $Re_{8,f}$ is forcing Reynolds number. ν_8 is the hyper-viscosity coefficient. k_b , k_o and $k_{f,z}$ are the buoyancy, Ozmidov and vertical forcing wavenumbers respectively.

Figure 4.16 displays instantaneous fields of the quantity b/N for different numerical resolutions. At the lowest numerical resolution 960×240 (figure 4.16, top), the horizontal layers are thicker than their analogous regimes with larger Reynolds number with less small scales. At this Reynolds number, the effect of the dissipation is strong, preventing the development of small scales in the flow. For 1920×480 and 3840×960 , fields are similar. The thickness of the horizontal layers is smaller than for 960×240 . We can see more small scales between these large horizontal layers than for the case with lower resolution. The increase of the Reynolds number enhances thus the apparition of small scales in the flow.

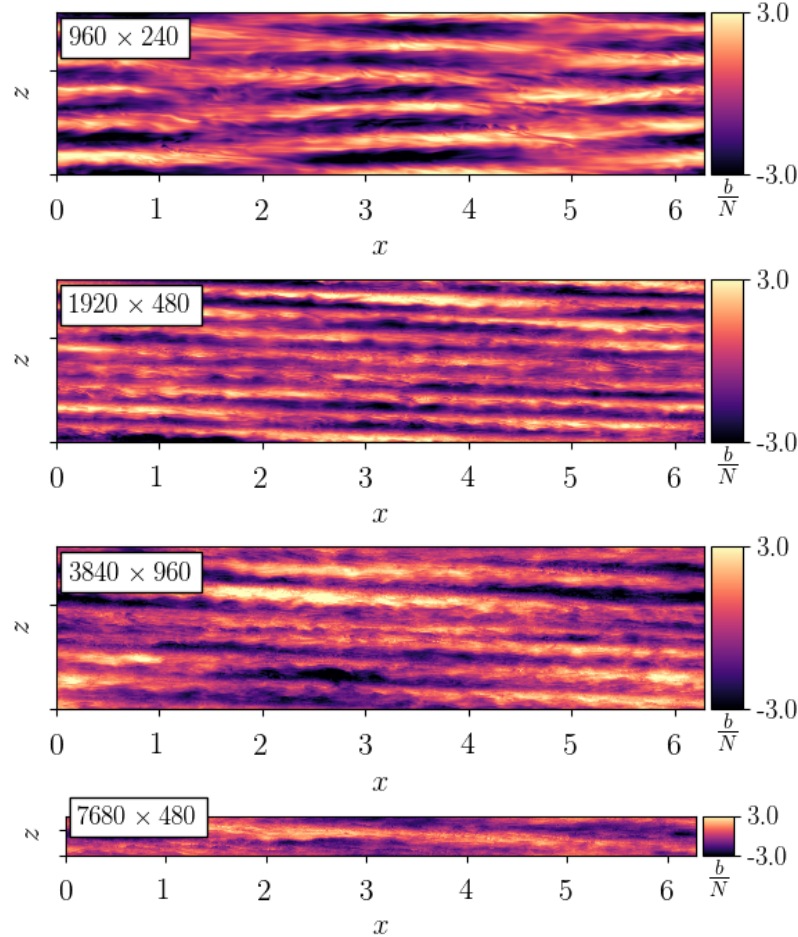


Figure 4.16: Snapshots of the quantity b/N in the statistically stationary state for different numerical resolutions $n_x \in [960, 1920, 3840, 7680]$ and for a fixed stratification strength $F_{h,f} = 0.09$ ($\gamma = 8.0$). Simulations $n_x \in [960, 1920, 3840]$ have a domain size $L_x = 4L_z$, while the simulation $n_x = 7680$ has a domain size $L_x = 16L_z$.

How does the Reynolds number affect the energy spectra?

Figure 4.17 displays the energy spectra for two different numerical resolutions: (a) 960×240 and (b) 7680×480 . For a low resolution (960×240), the horizontal energy spectra (solid lines) decreases fast at scales smaller than the forcing scale $k_x > k_{f,x}$. At this resolution, the dynamics are strongly affected by the viscosity. For a large resolution (figure 4.17 b), one can observe that the horizontal energy spectra does not decrease in the inertial range, which means that the dynamics is weakly affected by the viscosity. The vertical energy spectra has a peak located at $k \sim 0.5k_b$ corresponding to the thickness of the horizontal layers observed in figure 4.16. Furthermore, the vertical energy spectra decays in the inertial range with k_z^{-2} power law. At this point, two questions may come up: (i) does the vertical energy spectra scale with k_z^{-2} power law in $k_f \leq k \leq k_b$?; (ii) does the vertical energy spectra scale with $k_z^{-5/3}$ for modes $k > k_o$? The first question requires performing numerical simulations forced at large vertical scales. The second question can be answered by performing larger numerical simulations where the Ozmidov scale k_o is resolved. To conclude, one can notice that the dotted lines do not exist at the left side of the grey band. The forcing vertical mode corresponds to the first vertical mode δk_z of the numerical box.

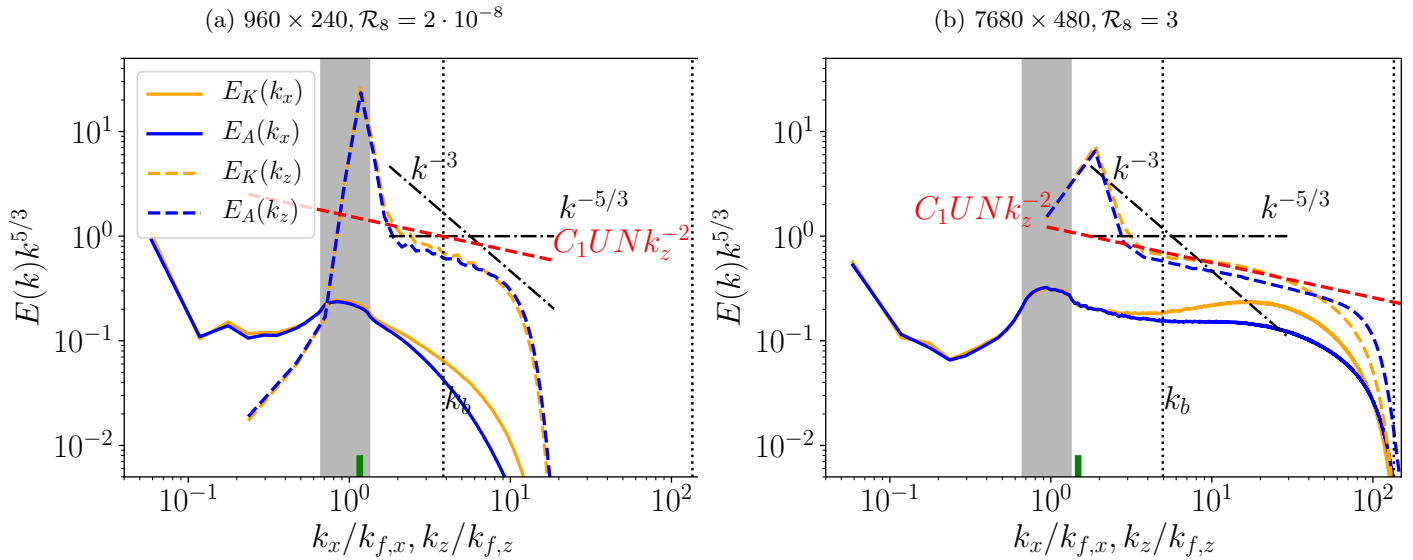


Figure 4.17: Horizontal (solid-line) and vertical (dashed-line) energy spectra for two different numerical resolutions: (a) 960×240 ; (b) 7680×480 . The stratification strength is $\gamma = 8.0$. The blue line represents the potential energy spectra. The orange line represents the kinetic energy spectra. The energy spectra is compensated by a power law $k^{5/3}$. The dashed black line represents the power laws $k^{-5/3}$ and k^{-3} . The red dashed line displays the model for the vertical energy spectra $E(k_z) = C_1 UN k_z^{-2}$, where $C_1 = 0.02$. The vertical grey band represents the forcing region. The green line displays the characteristic vertical wavenumber computed with the expression 4.7.

How does the Reynolds number affect the energy transfer mechanisms?

Figures 4.18 and 4.19 display the horizontal and vertical spectral energy budgets for two different numerical resolutions: (a) 960×240 and (b) 7680×480 . We first focus on figure 4.18 (a). We see that the spectral dissipation curve (green line) starts increasing at low wavenumbers k_x , meaning that large horizontal scales are affected by the viscosity. At the left side of the grey band, the dynamics is similar in figures 4.18 (a) and (b). It corresponds to the flux the loop already mentioned in Boffetta et al. (2011). At small scales for the horizontal energy budget (figure 4.18 (a)), we see that BOTH Π_K and Π_A (orange and blue lines) tend to zero, meaning that the dissipation damps all transfer of energy. For the vertical energy budget 4.18 (b), we see that the spectral dissipation curve (green line) starts increasing at $k_x/k_{f,x} \sim 30$. The dissipation acts at scales lower than the forcing scale, which means that effect of dissipation is weak and a true inertial range is developed in the horizontal direction. The effect of the Reynolds number is lower in the vertical direction (4.19 (a) and (b)). For both numerical resolutions, the dissipation starts acting at scales smaller than the forcing scale, which confirms that the dissipation does not have any effect on the vertical transfer of the energy. In both cases (figures 4.19 (a) and (b)), the black dotted line becomes constant. It means that there is a transfer of energy to small scales. The energy transfer is not dominated by the viscosity and an inertial range develops even at low resolution.

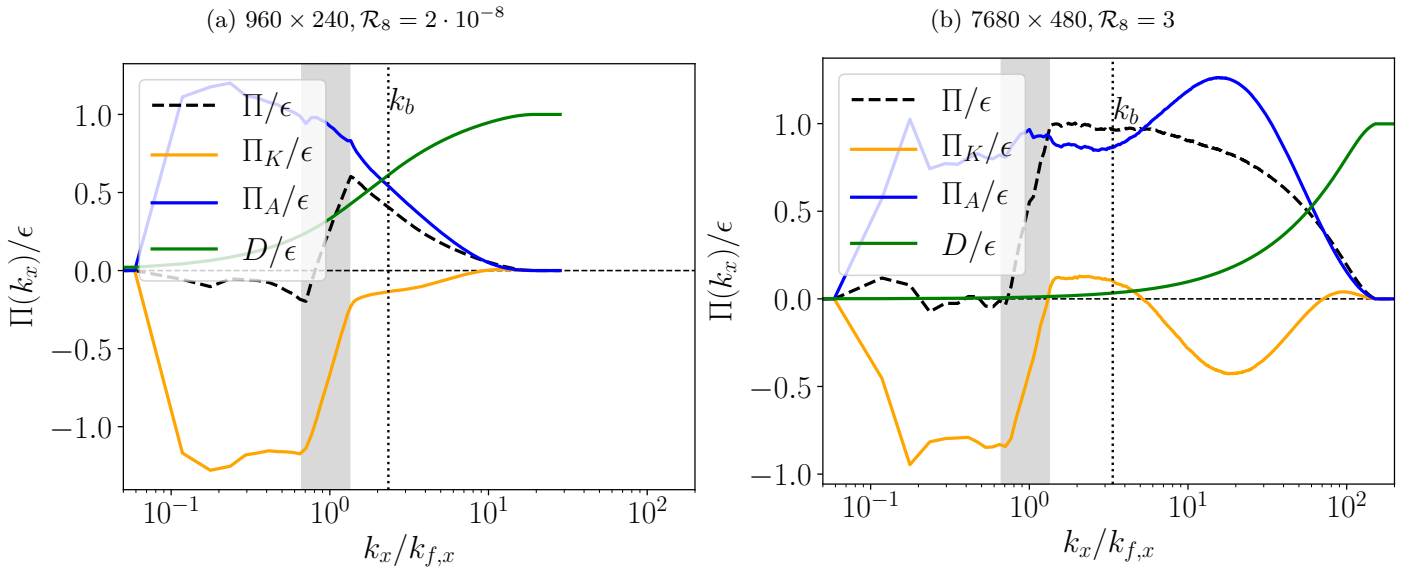


Figure 4.18: Horizontal energy fluxes for two numerical resolutions: (a) 960×240 ; (b) 7680×480 . The stratification strength is $\gamma = 8.0$. The blue line represents the potential energy flux Π_A . The orange line represents the kinetic energy flux Π_K . The black dotted line represents the flux of the total energy $\Pi = \Pi_K + \Pi_A$. The green line is the cumulative dissipation. The grey band represents the forcing wavenumbers. All quantities are normalized by the mean dissipation ϵ .

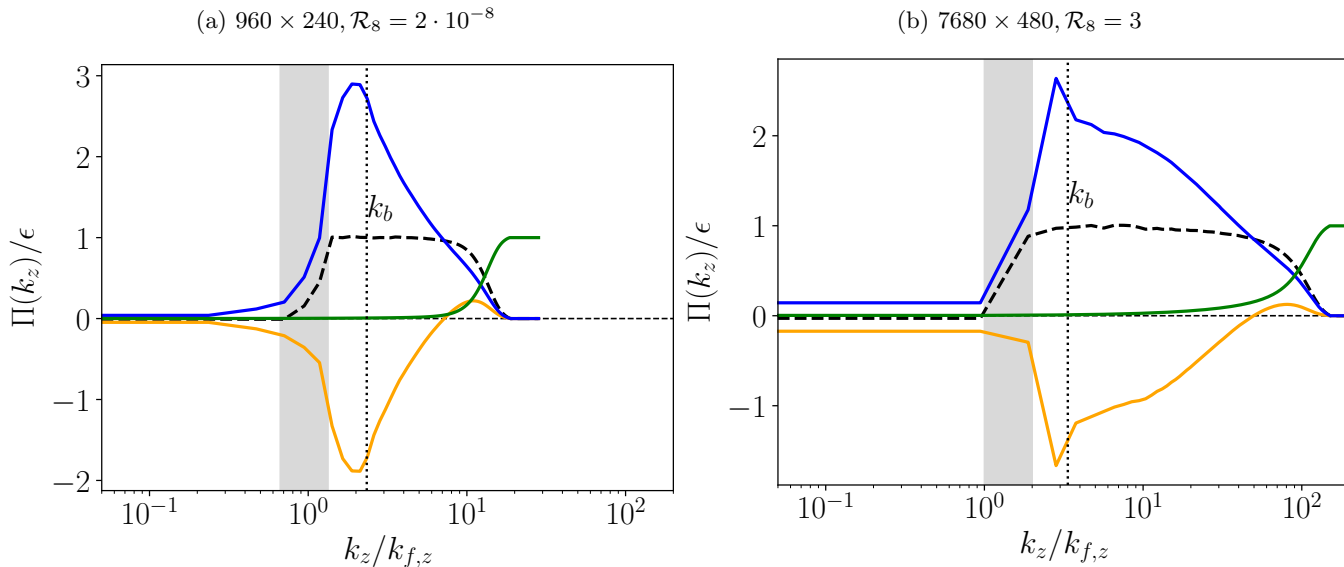


Figure 4.19: Same as in figure 4.18 for vertical energy fluxes.

4.3 Varying stratification and Reynolds number

In this section, we analyze simulations with different stratification strengths and different Reynolds number in order to identify the regimes in 2D stratified turbulence. We first focus on the averaged energy of the simulations. Figure 4.20 shows the averaged energy as function of the forcing horizontal Froude number $F_{h,f}$ for all simulations. The colors represent the four different numerical resolutions $n_x \times n_z$: green square (960×240), red triangle (1920×480), blue dot (3840×960) and yellow cross (7680×480). The averaged energy has been normalized by the energy injected in one period of forcing $\langle E \rangle_t / (P / \omega_{af})$. At low Froude number, the equation 4.3 shows that $\langle E \rangle_t / (P / \omega_{af}) \sim F_{h,f} / F_h$, where $F_{h,f} = F / \gamma$ and F_h is the horizontal Froude number. The errorbar displays the standard deviation of the averaged energy. For weakly stratified flows $F_{h,f} > 1$, one can observe that the markers are superposed. Their averaged energy slightly increases. The fact that the markers are superposed indicate that the averaged energy does not depend on the Reynolds number. These flows are weakly affected by the dissipation and therefore they do not depend on the Reynolds number. The increase of the averaged energy when decreasing the stratification has been already discussed in figure 6.4. When we decrease the stratification strength, the mechanisms to transport energy to small scales are less efficient. One needs to introduce, in average, more energy to reach the statistically stationary state. We now focus on values $10^{-1} < F_{h,f} < 1$. The markers are superposed indicating that there is no dependency on the Reynolds number. The flat region around values $F_{h,f} \sim 10^{-1}$ indicates the location of the strongly stratified turbulence regime. The scaling presented in the equation (4.4) indeed works for values $F_{h,f} \sim 10^{-1}$. Finally, for values $F_{h,f} < 10^{-1}$, the averaged energy increases to reach the statistically stationary state. The markers are less clear superposed, implying dependence with the Reynolds number.

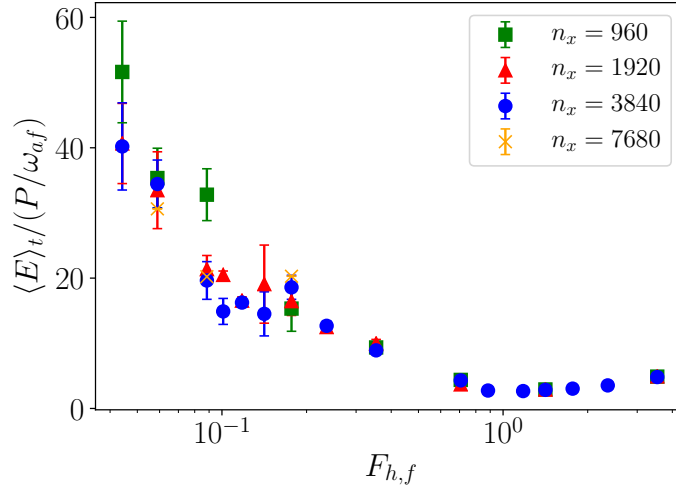


Figure 4.20: Averaged energy E as function of the forcing horizontal Froude number $F_{h,f}$ for all simulations. The colors represent the four different numerical resolutions $n_x \times n_z$: green square (960×240), red triangle (1920×480), blue dot (3840×960) and yellow cross (7680×480). The errorbar displays the standard deviation of the averaged energy σ_E .

Shear instabilities for different Reynolds numbers

We have seen that strongly stratified flows are anisotropic. The energy dissipation takes place at small vertical scale between the large horizontal scales. Shear instabilities can develop due to the large vertical gradient of velocity between these large horizontal scales. These may produce small scales where the energy is dissipated. The creation of small scales is strongly related to the effect of the viscosity. Flows with a low Reynolds number are strongly affected by the viscosity. The dissipation prevents the development of the shear instabilities and the production of small scales. It has been already observed in the field presented in figure 4.16 for 960×240 . It is therefore important to study the development of the shear instabilities for different Reynolds number.

Figure 4.21 displays the instantaneous local Richardson number Ri for four stratification strengths $\gamma \in [0.2, 1, 4, 8]$ and for three different numerical resolutions $n_x \in [960, 1920, 3840]$. Three numerical resolutions are presented for simplicity. As it has been mentioned in figures 4.11 - 4.14, the development of the Kelvin-Helmholtz instability is only possible for values $0 < Ri < 1/4$. The colormap ranges only for values of $0 < Ri < 1/4$. The white regions mean that no shear instabilities can be developed. The dependency of the Richardson number Ri has been discussed in figures 4.11 - 4.14. I will discuss the dependency of the Ri for different numerical resolutions n_x . In fields with $\gamma = 0.2$, we see more dark colored regions for large numerical resolutions $n_x = 3840$ than for low resolutions $n_x = 960$. Simulations with low numerical resolutions are more affected by the viscosity than simulations with larger n_x . The viscosity prevents the development of the shear instabilities on the flow. The effect of the Reynolds number, i.e. dissipation, is more pronounced for large stratifications. We now focus on the Ri fields for $\gamma = 8.0$. We see that, for $n_x = 960$, the field is almost white. It means that not shear instabilities are developed. It is due to the fact that the flow is strongly affected by the dissipation. When we increase the numerical resolution $n_x = 3840$, we see that zones with potential shear instabilities start appearing on the flow. As it has been observed in figure 4.14, the zones with lowest value Ri are the interface of the horizontal layers. The development of

the KH instability is associated with the strong shear of the horizontal layers. It has to be noticed that increasing the Reynolds number decreases the effect of the dissipation in the flow. It enhances thus the possibility to develop shear instabilities.

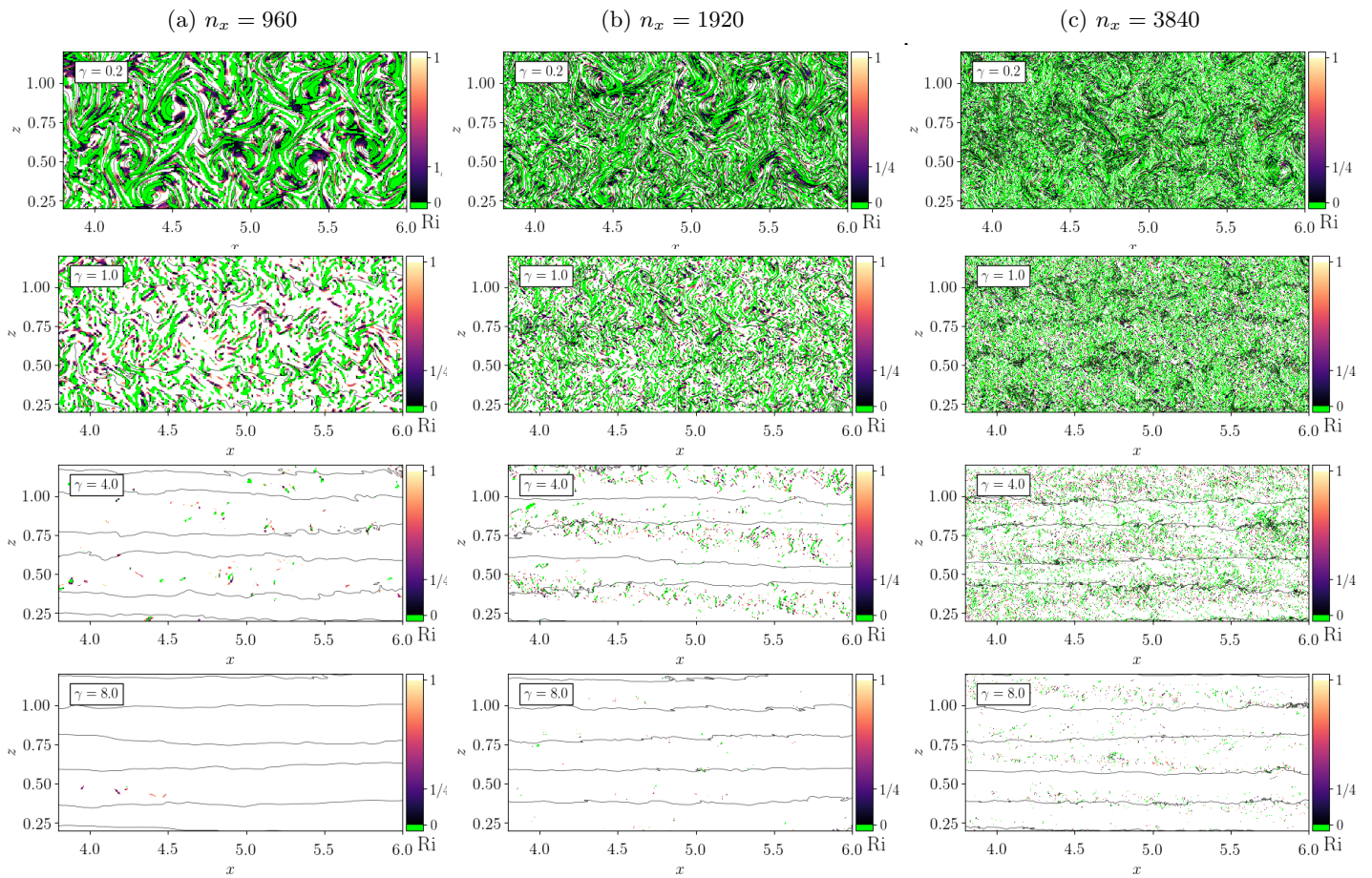


Figure 4.21: Local Richardson number Ri for different values of $\gamma \in [0.2, 1.0, 4.0, 8.0]$ and for different numerical resolutions $n_x \in [960, 1920, 3840]$.

Isotropy at large scales \mathcal{I}_E and isotropy of the dissipation \mathcal{I}_d

In this section, we analyze the dependency on the Reynolds number for the isotropy at large scales \mathcal{I}_E and isotropy of the dissipation \mathcal{I}_d . Figure 4.22 displays the isotropy quantity \mathcal{I}_E , defined in the equation (4.5), as function of the forcing horizontal Froude number $F_{h,f}$. The colors display the four different Reynolds number. For $F_{h,f} > 2 \cdot 10^{-1}$, the markers are superposed indicating that there is no dependency on the Reynolds number. For $F_{h,f} < 2 \cdot 10^{-1}$, the index \mathcal{I}_E depends on the Reynolds number. Strongly stratified flows with a low Reynolds number are indeed affected by the viscosity. Flows with large numerical resolution n_x are less affected by viscous dissipation. Their vertical motions are less damped by dissipation.

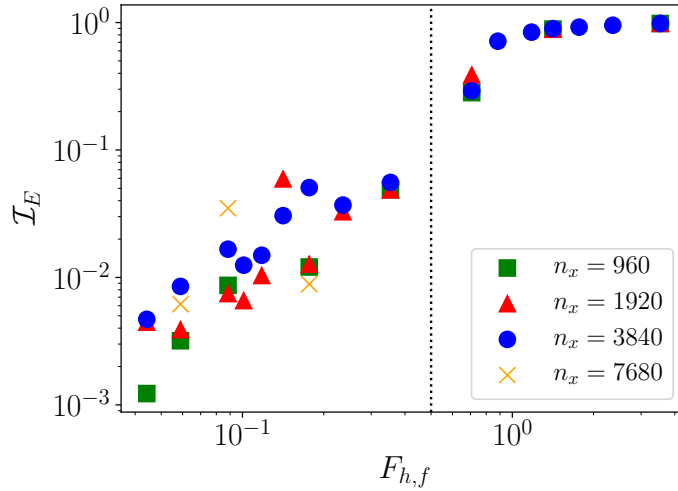


Figure 4.22: Isotropy \mathcal{I}_E as function of the forcing horizontal Froude number $F_{h,f}$. The colors represent the different numerical resolutions n_x

We have seen that, for strongly stratified flows, the anisotropy is larger for those with low Reynolds numbers than for those with large Reynolds. I study now the isotropy of the dissipation for different numerical resolutions n_x , i.e. Reynolds numbers. I use the index \mathcal{I}_d defined in the equation (4.6). For values $\mathcal{I}_d \rightarrow 1$, the dissipation is isotropic. For values $\mathcal{I}_d \rightarrow 0$, the dissipation is anisotropic. In the latter case, the dissipation occurs at large horizontal scales with small vertical scales. It is due to the anisotropy of the flow. As it has been mentioned in section 2, strongly stratified turbulent regimes require a buoyancy Reynolds number $\mathcal{R}_8 > 1$. The quantity \mathcal{I}_d is analyzed in terms of the buoyancy Reynolds number \mathcal{R}_8 . Figure 4.23 displays the isotropy of the dissipation \mathcal{I}_d as function of the forcing horizontal Froude number $F_{h,f} = F/\gamma$ (figure 4.23, left) and as function of the buoyancy Reynolds number \mathcal{R}_8 (figure 4.23, right). The colors represent the different numerical resolutions. The vertical dotted lines indicate the breaks of the slopes indicating potentially three different regimes. These regimes will be discussed in detail later in section 4.4. We now focus on figure 4.23 (left). For large values of $F_{h,f}$, the value of \mathcal{I}_d is of order of unity. It means that for weak stratification flows, the dissipation is isotropic. It has to be noticed that the markers are superposed. It means that there is no dependence on their Reynolds number. For small values of $F_{h,f}$, the value of \mathcal{I}_d decreases. Strongly stratified flows have an anisotropic dissipation. The markers are not anymore superposed. The dissipation is more anisotropic for those flows with lower Reynolds number (green square and red triangle) than for those with larger Reynolds number (blue dot and yellow cross).

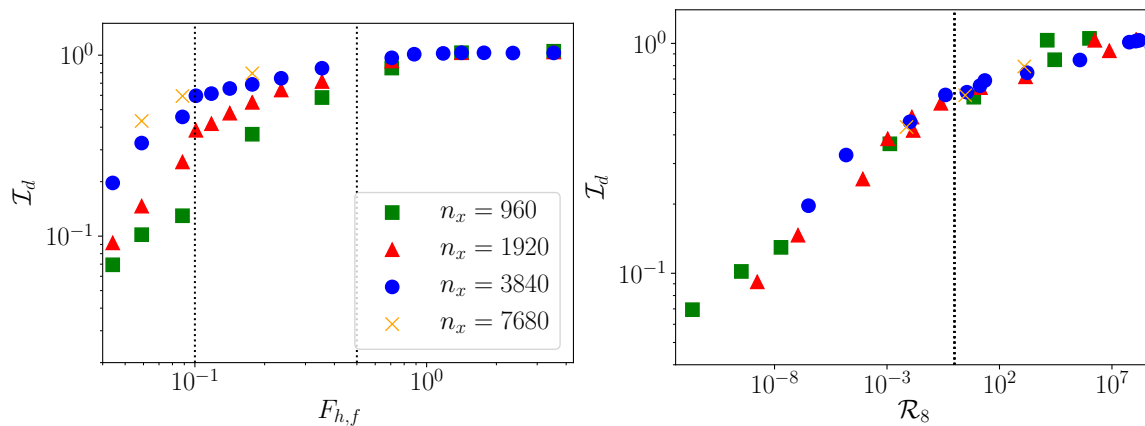


Figure 4.23: Dissipation quantity \mathcal{I}_d as function of the horizontal forcing horizontal Froude number $F_{h,f}$ (left) and as function of the buoyancy Reynolds number \mathcal{R}_8 (right). The colors represent the different numerical resolutions n_x . The vertical dotted lines in right figure delimit the break of the slopes.

In figure 4.23 (right), we see that the dissipation is nearly isotropic for $\mathcal{R}_8 > 1$. For low values of the buoyancy Reynolds $\mathcal{R}_8 < 1$, the dissipation starts becoming anisotropic. One has noticed that the markers are superposed. If our definition of \mathcal{R}_8 is valid, the quantity \mathcal{I}_d should not have any dependence on the \mathcal{R}_8 . The points should be superposed. We can thus consider our definition of the buoyancy Reynolds number \mathcal{R}_8 valid.

Vertical scale k_v for different Reynolds numbers

In this section, we analyze the characteristic vertical scale for different Reynolds numbers. Figure 4.24 displays the vertical wavenumber k_v as function of the forcing horizontal Froude number $F_{h,f}$ (a) and as function of the buoyancy Reynolds number \mathcal{R}_8 (b). The colors represent the different numerical resolutions. In figure 4.24 (a), we see that k_v decreases when $F_{h,f}$ increases. The flow becomes isotropic when increasing the value $F_{h,f}$. Its vertical scale increases until be similar to the horizontal scale (isotropy). For values $F_{h,f} < 1$, the value k_v remains constant. It is due to the viscosity. Dissipation does not allow the layers to decrease their thickness. Figures 4.24 (c) - (d) display the ratio of the vertical and buoyancy wavenumbers k_v/k_b as function of the $F_{h,f}$ and \mathcal{R}_8 respectively. It allows to check the inviscid scaling proposed by Billant, Chomaz (2001) of the strongly stratified turbulence. We see that the scaling is not valid for large values of forcing Froude $F_{h,f} > 1$. For values $F_{h,f} \sim 0.4$, the ratio k_v/k_b is slightly constant. We can consider that the strongly stratified regime is achieved at $F_{h,f} \sim 0.4$. For values $F_{h,f} < 0.2$, the scaling is not valid. For large stratification strengths, the flows become indeed highly anisotropic and dissipative. Figures 4.24 (e) - (f) display the ratio of the vertical and viscous wavenumbers $k_v/k_{\nu 8}$ as function of the $F_{h,f}$ and \mathcal{R}_8 respectively. It allows to check the scaling proposed by Godoy-Diana et al. (2004) of strongly stratified flows affected by the dissipation. The markers are totally scattered indicating that this scaling is not valid.

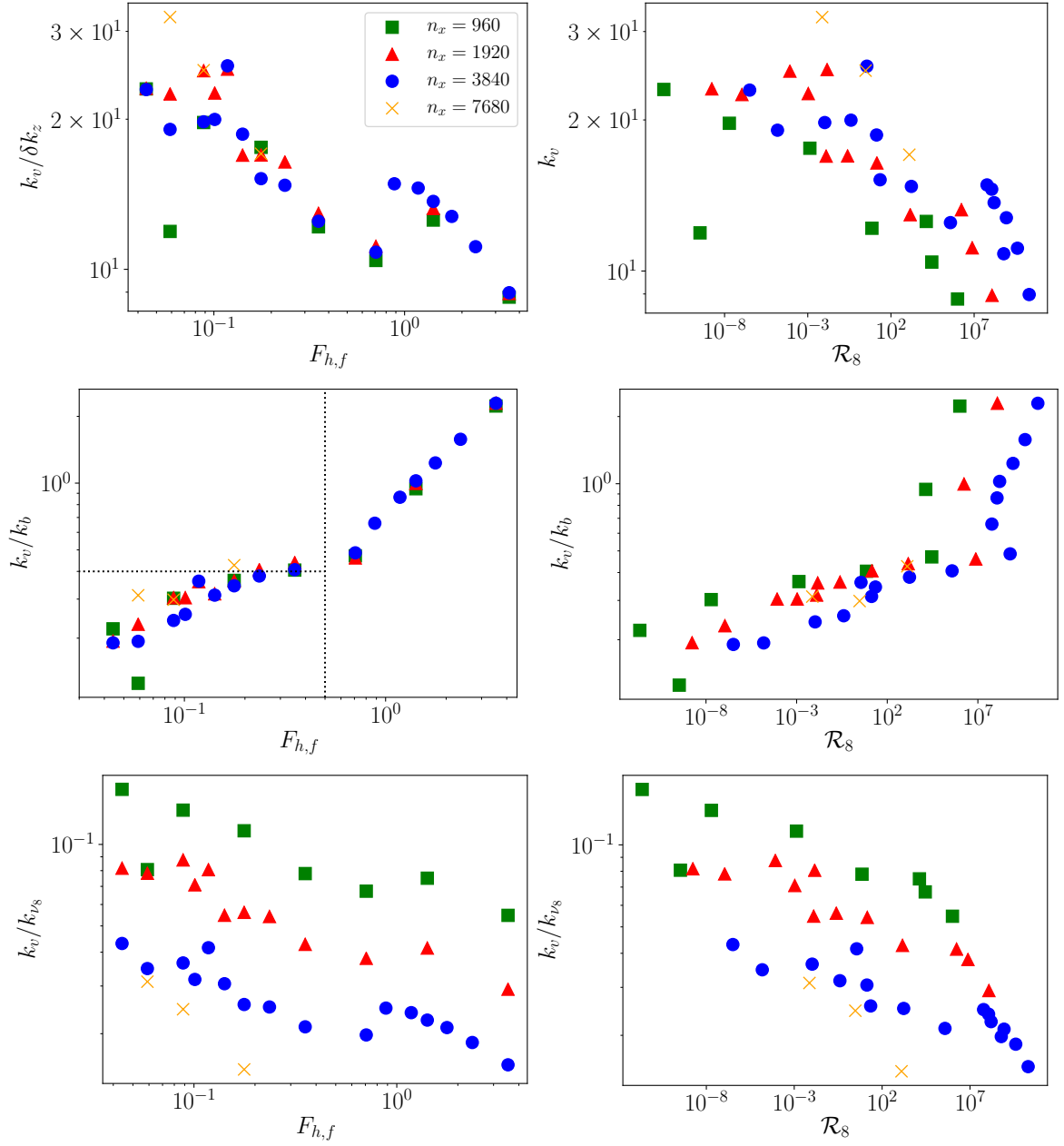


Figure 4.24: Vertical wavenumber k_v as function of the horizontal forcing Froude number $F_{h,f}$ (a). Vertical wavenumber k_v as function of the buoyancy Reynolds number \mathcal{R}_8 (b). Ratio vertical and buoyancy wavenumbers k_v/k_b as function of $F_{h,f}$ (c). Ratio k_v/k_b as function of \mathcal{R}_8 (d). Ratio vertical and viscous wavenumber $k_v/k_{\nu 8}$ as function of $F_{h,f}$ (e). Ratio $k_v/k_{\nu 8}$ as function of \mathcal{R}_8 (f). The colors represent the different numerical resolutions n_x .

4.4 Regimes in 2D stratified turbulence

This PhD work aims to develop a phenomenology of the 2D stratified turbulence. We have reviewed, throughout the chapter 4, the dynamics of a stratified fluid for different stratification strengths and different non-linear regimes. We have identified three different regimes depending on the value of the buoyancy Reynolds number \mathcal{R}_8 and the forcing horizontal Froude number $F_{h,f}$. Figure 4.25 displays the buoyancy Reynolds number \mathcal{R}_8 as function of the forcing horizontal Froude number $F_{h,f}$ for all simulations performed in this chapter. Note higher resolution simulations 15360×960 have been included in this figure and they will be discussed in the next section. The colormap of the figure displays the isotropy quantity \mathcal{I}_E . The size of the markers indicate the isotropy of the dissipation \mathcal{I}_d . The shape of the markers represent the different numerical resolutions n_x . The vertical and horizontal dotted lines delimit the different regimes in the parameter space $\{F_{h,f}, \mathcal{R}_8\}$

One can identify three different regimes depending on the value pair $\{F_{h,f}, \mathcal{R}_8\}$: (i) weakly stratified and strongly non-linear regime, (ii) strongly stratified and strongly non-linear regime, and (iii) strongly stratified viscosity-affected regime. Weakly stratified flows have a forcing horizontal Froude number $F_{h,f} > 0.5$. These flows are isotropic at large scales, i.e. large \mathcal{I}_E . They have a flux loop with a forward cascade of energy towards small scales. We focus now on the strongly stratified and strongly non-linear regime. This regime belongs to the range $F_{h,f} < 0.5$ and $\mathcal{R}_8 > 1$. It is the most similar to the regimes observed in nature. The flows are anisotropic, i.e. small \mathcal{I}_E , with isotropic dissipative scales. A clear inertial range is developed with a forward cascade of energy towards small scales. The vertical energy spectra follows k_z^{-2} power-law. At the interface of the large horizontal scales, shear instabilities take place and produce isotropic small scales. The thickness of the horizontal scales are of order $l_v \sim l_b$, where l_b is the buoyancy length scales as predicted in Billant, Chomaz (2001). Nevertheless, we need to perform higher resolution numerical simulations to resolve, at least, the Ozmidov length scale. It will allow us to check the spectral break of the vertical energy spectra. We focus now on the strongly stratified but viscosity-affected regime. These flows are delimited by $F_{h,f} < 0.5$ and $\mathcal{R}_8 < 1$. These flows are anisotropic, i.e. small \mathcal{I}_E , and with anisotropic dissipative scales. The horizontal scales are strongly affected by viscous dissipation preventing the development of a clear inertial range. In section 4.3, we have tested the scaling proposed by Godoy-Diana et al. (2004) for a 3D configuration. We have seen that this scaling is not valid for the same regime for a 2D configuration. To conclude and as it has been mentioned, geophysical flows such as oceans and the atmosphere belong to the strongly stratified and strongly non-linear regime. They are characterized to be strongly anisotropic but with isotropic dissipative scales. In the last part of this chapter, section 4.5, we describe the dynamics of the strongly stratified and strongly non-linear regime. We have not considered here turbulent regimes driven by weakly interacting waves. We expect to obtain this regime for $F_h \ll 1$ (strong stratification) and $\mathcal{R} \sim 1$ (weakly non-linear and weakly dissipative at large-scales). In chapter 5, we discuss turbulence driven by weakly nonlinear internal waves by means of spatio-temporal analysis.

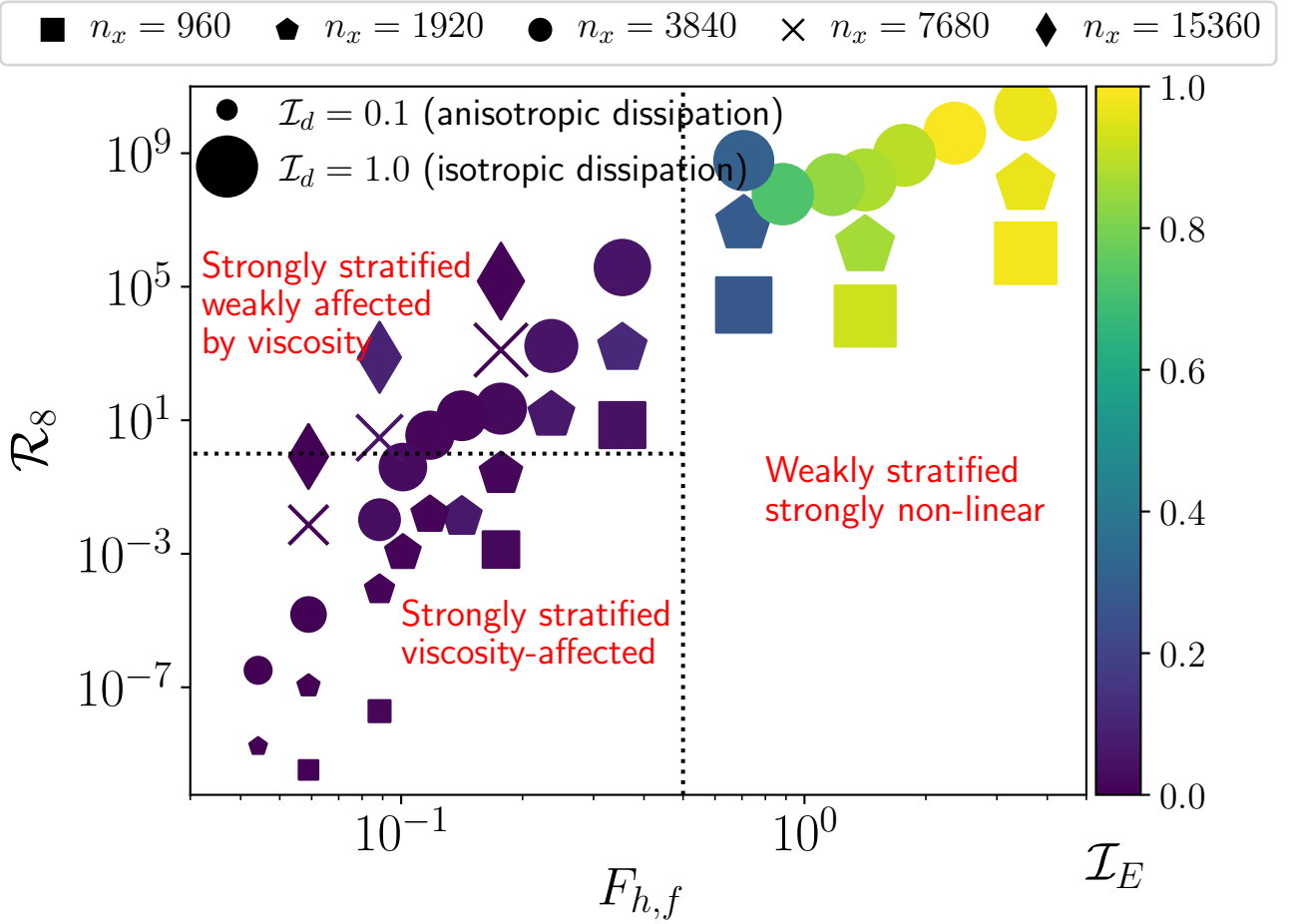


Figure 4.25: Buoyancy Reynolds number \mathcal{R}_8 as function of the forcing horizontal Froude number $F_{h,f}$ for all simulations. The colormap displays the isotropy quantity \mathcal{I}_E . The size of the markers represents the isotropy of the dissipation \mathcal{I}_d . The shape of the markers represent the different numerical resolutions n_x . Three regimes are identified: (i) weakly stratified and strongly non-linear regime, (ii) strongly stratified and strongly non-linear regime, and (iii) strongly stratified viscosity-affected regime.

4.5 Description of the strongly stratified and strongly non-linear regime $F_{h,f} < 0.5$ and $\mathcal{R}_8 > 1$

Geophysical flows, such as flows in the middle atmosphere or in the upper ocean, are considered to be turbulent and strongly affected by the stratification. This regime requires both low Froude number F_h and high Reynolds number Re (Brethouwer et al., 2007). In figure 4.9, we have seen that the flow becomes viscosity-affected for large stratification strength in our DNS. In order to approach to geophysical regimes with horizontal scales weakly affected by the dissipation, we have performed numerical simulations with a numerical resolution 15360×960 . The simulations have been performed in the French National supercomputer Occigen (CINES). In this section, I discuss flows with a large Reynolds number Re_8 , i.e. large numerical resolutions, for two different stratification strengths $\gamma = 4.0$ and $\gamma = 8.0$. Figures 4.26 and 4.27 display the snapshots of the quantity b/N at the statistically stationary state for $\gamma = 4.0$ and $\gamma = 8.0$, respectively. The white rectangles represents a zoomed region, which is represented in figures below the original figure. For $\gamma = 4.0$, the flow is developed in horizontal layers. The thickness of the layers are similar to the vertical size of the domain. At large scales, the dynamics is strongly anisotropic. The zoomed region shows us the presence of small scales within the layers. We see that the dynamics is isotropic at small scales. It might be due to the fact that small scales do not feel the buoyancy effect. For $\gamma = 8.0$, we see that the dynamics develop in horizontal layers. The thickness of the layers decreases as the stratification strength increases, i.e. large values of γ . We see that the flow is strongly anisotropic overall.

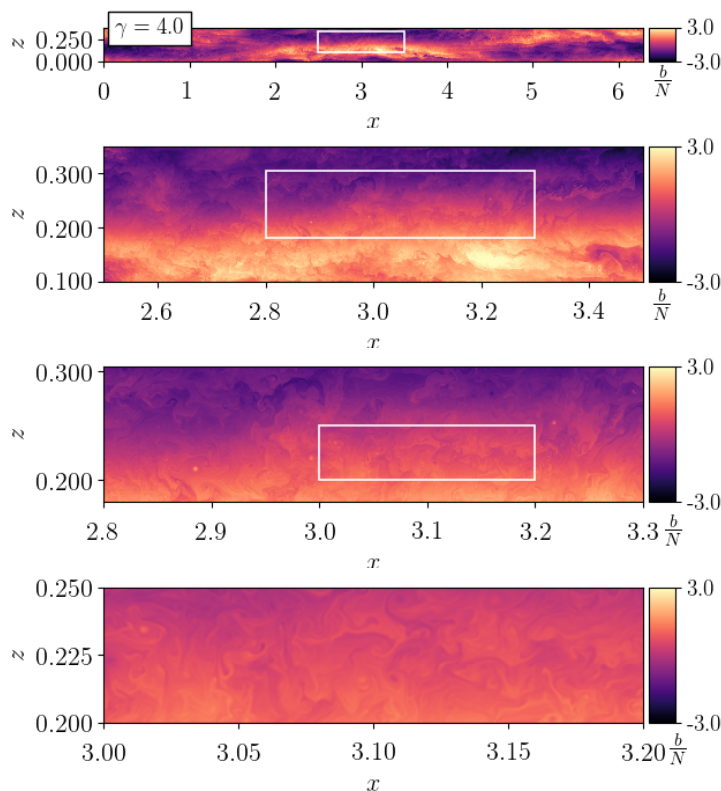
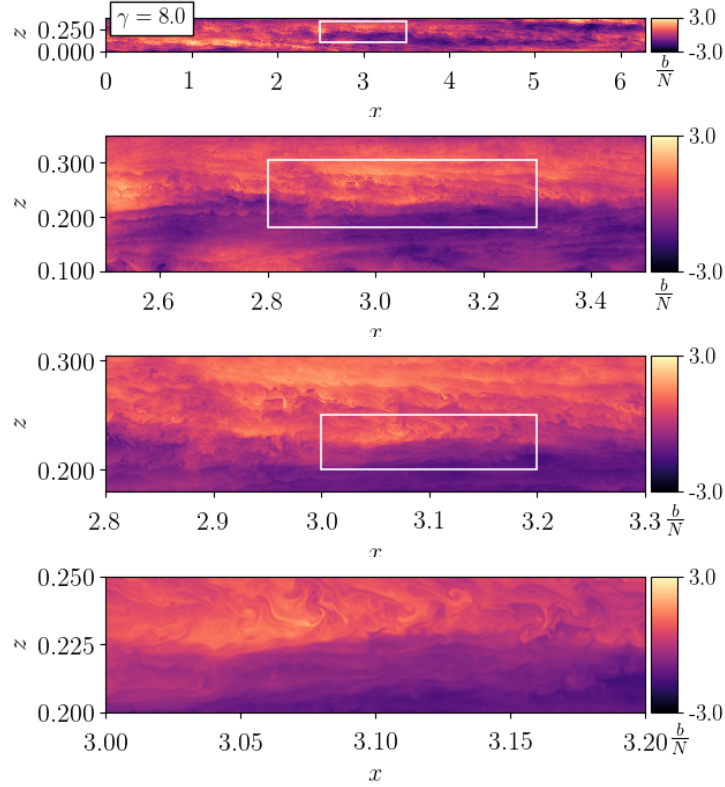


Figure 4.26: Snapshot of the field b/N at the statistically stationary state for $\gamma = 4.0$. The resolution of the simulation is 15360×960 . The white rectangle displays the zoomed region represent in figure below.


 Figure 4.27: Same as figure 4.26 but for $\gamma = 8.0$.

Energy spectra for $F_{h,f} < 0.5$ and $\mathcal{R}_8 > 1$

We now discuss the energy distribution among the scales. Figure 4.29 displays the energy spectra for two values of γ : (a) $\gamma = 4.0$, (b) $\gamma = 8.0$. The orange lines represent the kinetic energy spectra. The blue line represent the potential energy spectra. The solid lines represent the horizontal energy spectra. The dashed lines represent the vertical component of the energy spectra. The energy spectra is compensated with the power law $k^{-5/3}$. The wavenumbers are normalized by the forcing wavenumbers $k_{f,x}$ and $k_{f,z}$ respectively. The grey vertical band displays the forcing region. We first focus on the energy spectra for $\gamma = 4.0$ (figure 4.29 (a)). For large horizontal scales $k_x < k_{f,x}$, the kinetic (orange solid) and potential (blue solid) energy spectra are superposed, which suggesting the presence of large scale internal gravity waves. We see that at the first horizontal mode, there is a peak in the horizontal energy spectra, which corresponds to the horizontal layers observed in figure 4.26. At small scales $k_x > k_{f,x}$, the kinetic energy (orange) dominates over the potential (blue) energy along the inertial range. A transition occurs at the Ozmidov wavenumber k_o . The potential energy (blue solid line) dominates over the kinetic energy (orange solid line). We now focus on the vertical energy spectra (dashed lines). Like the horizontal component, at wavenumbers $k_z > k_{f,z}$, the kinetic energy spectra (orange dashed line) dominates over the potential energy spectra (blue dashed line). There is a transition at the Ozmidov wavenumber k_o . The potential energy spectra follow the power law of k^{-2} for wavenumbers $k_{f,z} < k_z < k_o$. For wavenumbers $k_z > k_o$, the potential energy spectra is horizontal. It means that it follows the power law $k^{-5/3}$. The main difference with the lower-resolution simulations presented in the previous sections is that the Ozmidov scale is resolved with high resolution. We can see indeed a transition of the energy spectra at the Ozmidov scale. At this scale, the energy spectra become isotropic again. We now focus on the energy spectra for $\gamma = 8.0$ (figure 4.29 (b)). For $k_{f,x} < k_x < k_b$, the horizontal energy spectra (solid lines) seem to follow a k_x^{-2} power-law with a bump

of the kinetic energy spectrum at scales $k_x > k_b$. This bump, at horizontal wavenumbers slightly larger than k_b , has been also reported in previous numerical studies (Waite, 2011; Augier et al., 2015). Figure 4.28 (a) displays the horizontal energy spectra extracted from Waite (2011), and figure 4.28 (b) the horizontal and vertical energy spectra extracted from Augier et al. (2015). Both works show that the horizontal energy spectra develops a bump at $k_x > k_b$. We have mentioned that the horizontal energy spectra scales as k_x^{-2} for modes

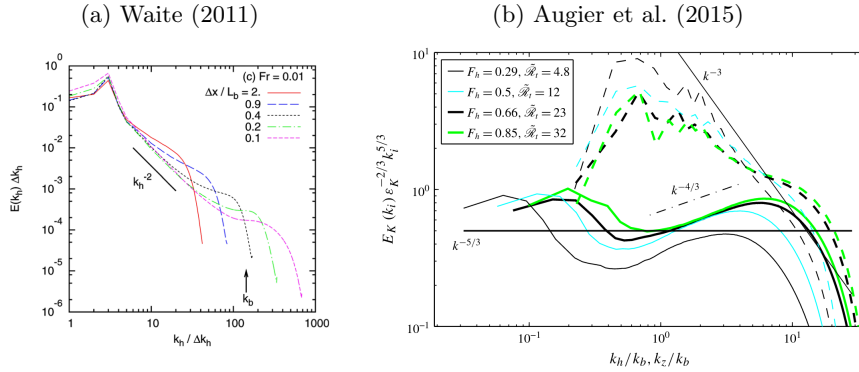


Figure 4.28: (a) Horizontal energy spectra extracted from Waite (2011), and (b) horizontal (solid lines) and vertical (dashed lines) compensated energy spectra extracted from Augier et al. (2015).

$k_{f,x} < k_x < k_b$ as reported in Waite (2011); Yokoyama, Takaoka (2019). Furthermore, an equipartition of kinetic and potential energy is displayed at $k_{f,x} < k_x < k_b$, suggesting the presence of internal gravity waves. One needs to compute the energy fluxes to check if the energy transfer is dominated by a wave mechanism. We now focus on the vertical component of the energy spectra (dashed lines). One can observe that there is a peak at $k_z > k_{f,z}$. As it has been mentioned before, this peak might be probably correspond to the thickness of the horizontal layers. The vertical potential energy spectra (blue dashed line) follows the power law of k_z^{-2} . There is no transition found. It might be due to the fact that the Ozmidov wavenumber is found at the dissipative scales. It is important to notice that the blue dashed line and orange dashed line are similar at the inertial range. It could suggest a possible cascade dominated by internal waves.

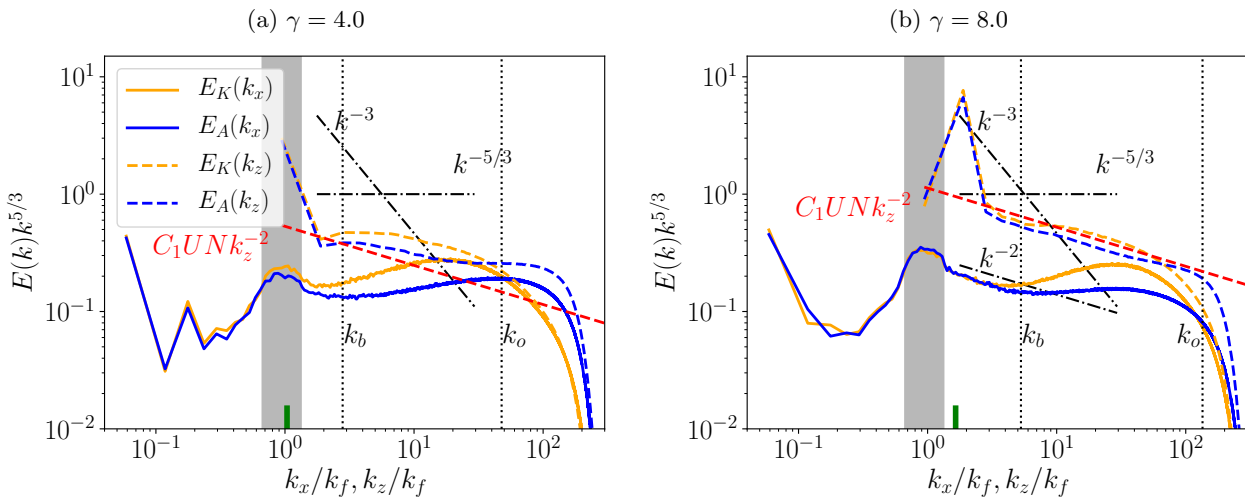


Figure 4.29: Horizontal (solid-line) and vertical (dashed-line) energy spectra for two different stratifications: (a) $\gamma = 4.0$; (b) $\gamma = 8.0$.

Spectral energy budget for $F_{h,f} < 0.5$ and $\mathcal{R}_8 > 1$

We refer to the energy fluxes in order to study the energy transfer mechanisms of the strongly stratified turbulence regime. Figures 4.30 and 4.31 display the spectral energy budget for $\gamma = 4.0$ and $\gamma = 8.0$ respectively. The orange line is the kinetic energy flux Π_K . The blue line is the potential energy flux Π_A . The black dotted line is the total energy flux $\Pi = \Pi_K + \Pi_A$. The green line is the dissipation. All curves are normalized by the mean dissipation rate ϵ . Note that both numerical simulations have not reached yet a statistically stationary state at this stage of the PhD work. The total energy flux (black dashed line) is indeed not zero for large horizontal scales $k_x < k_{f,x}$. Nevertheless, the dynamics is sufficiently developed to give insights about the energy transfer mechanisms.

We focus first on the spectral energy budget for $\gamma = 4.0$ (figure 4.30). We see that the horizontal (a) and vertical components (b) of the spectral energy budget are quite different. It confirms that the dynamics is anisotropic. We focus on the horizontal component (figure 4.30 (a)). At scales $k_x < k_f$, we see that the orange line is negative and the blue line is positive. At scales larger than the forcing scale, we have a negative flux of kinetic energy Π_K and positive flux of potential energy Π_A . The energy is transferred from the injection scale to large scales through an inverse cascade of kinetic energy. At large scales, where the buoyancy effect is important, the kinetic energy is converted to the potential energy. The potential energy is transferred down scale. At wavenumbers $k_f < k_x < k_b$, the orange and blue lines are positive. Between the forcing k_f and buoyancy k_b wavenumbers there is a downscale cascade of kinetic (orange) and potential (blue) energy. It might be due to a possible cascade of waves. At wavenumbers $k_x > k_b$ there is a transition of the orange line. The orange line becomes negative. At this point, there is an inverse cascade of kinetic energy (orange) and a direct cascade of potential energy (blue). In the vertical spectral energy budget (figure 4.30 (b)), we see no flux at large scales, i.e. wavenumbers $k_z < k_{f,z}$. For scales smaller than the forcing scale, we see a positive blue line and negative orange line. There is a direct cascade of energy dominated by the potential energy (blue line) coupled with an inverse cascade of kinetic energy (orange). We see that the black dashed lined forms a plateau around $\Pi/\epsilon = 1$. The transfer of energy is not affected by the dissipation.

We focus now on the spectral energy budget for $\gamma = 8.0$ (figure 4.31). We see similar behavior as for $\gamma = 4.0$. In the horizontal component of the spectral energy budget (figure 4.31 (a)), we see the dual flux loop mechanisms. At wavenumbers $k_x < k_{f,x}$, it appears the first energy flux loop. There is an inverse cascade of kinetic energy. At large scales, the kinetic energy is converted to potential energy where is transferred towards small scales. The second flux loop observed is at wavenumbers $k_x > k_b$, where the energy cascades towards small scales. The vertical component of the spectral energy budget (figure 4.31 (b)) has only a direct cascade of energy. To conclude, the kinetic energy flux develops three different regimes: (i) for $k_{f,x} < k_x < k_b$, the kinetic energy flux is positive, (ii) $k_b < k_x < k_o$ the kinetic energy flux becomes negative developing a flux loop at small scales, and (iii) for $k_x > k_o$ the kinetic energy flux becomes positive. Note that it is the horizontal energy flux sensible to the buoyancy wavenumber k_b , instead of being the vertical energy flux. As it has been mentioned above, this positive flux of kinetic energy could be related to a wave cascade.

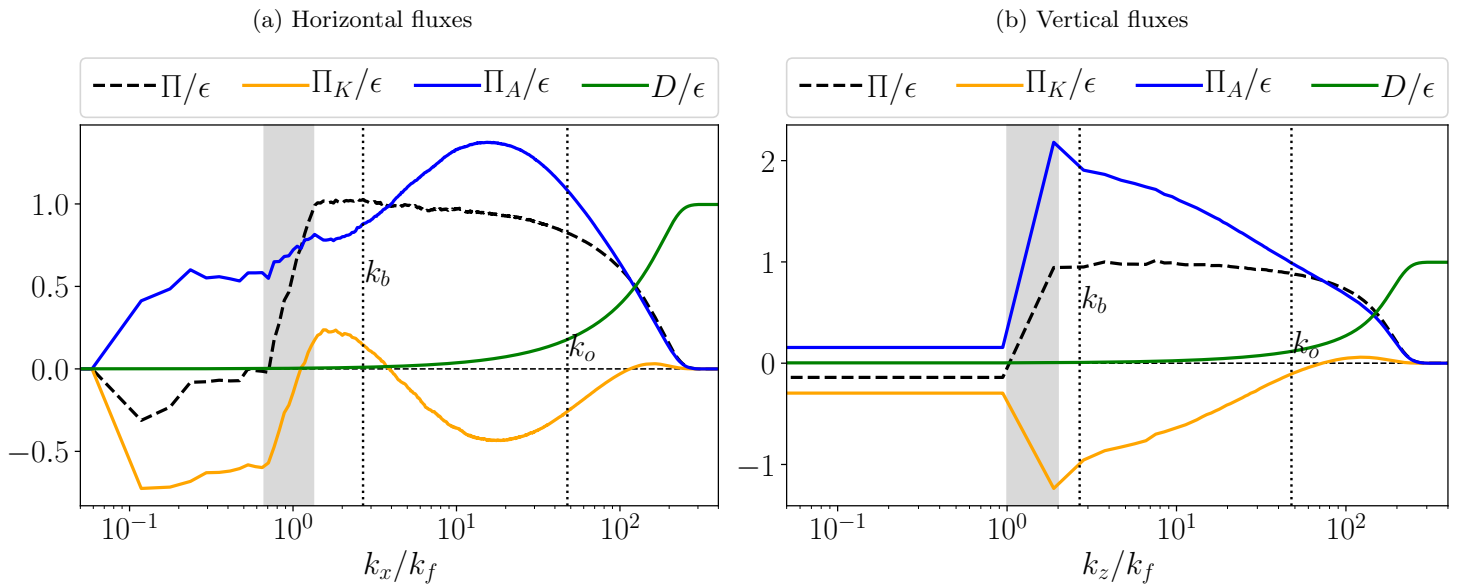


Figure 4.30: Horizontal (a) and vertical (b) spectral energy budget for $\gamma = 4.0$ and for a numerical resolution 15360×960 . The orange line is the kinetic energy flux Π_K . The blue line is the potential energy flux Π_A . The black dotted line is the total energy flux $\Pi = \Pi_K + \Pi_A$. The green line is the dissipation. All curves are normalized by the mean dissipation rate ϵ .

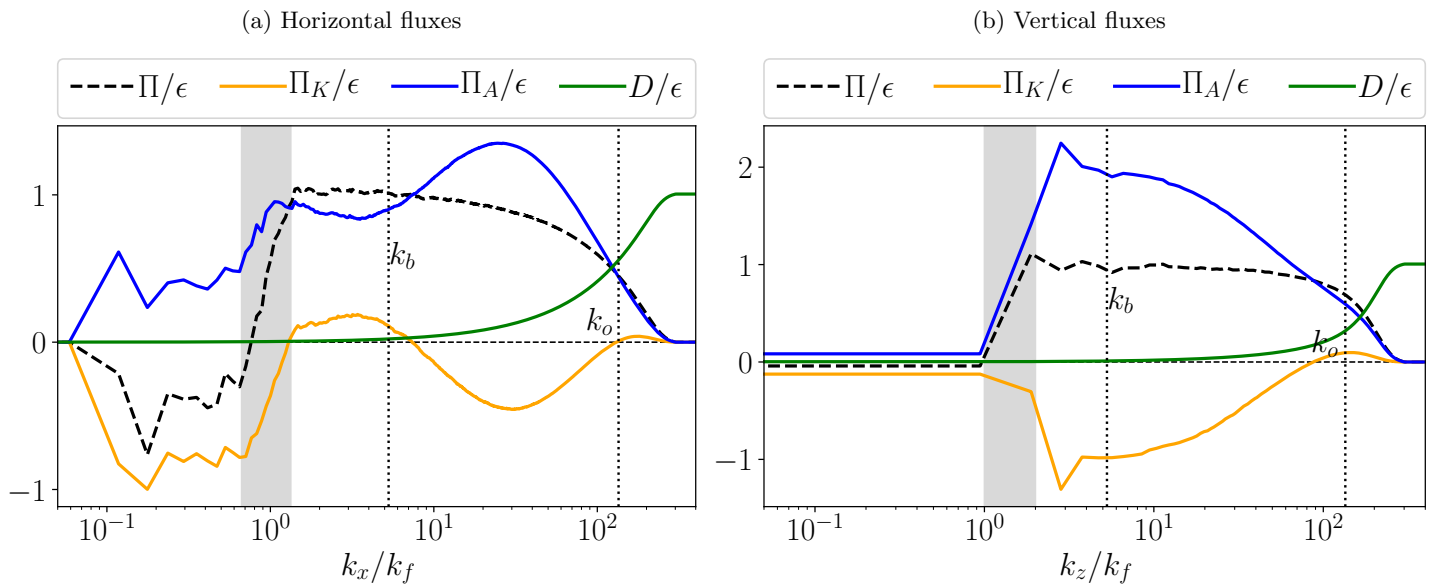


Figure 4.31: Same as figure 4.30 for $\gamma = 8.0$.

Chapter 5

Is 2D stratified turbulence driven by weakly nonlinear interacting internal gravity waves?

The ocean energy spectra is reconstructed as a superposition of non-linear interacting internal gravity waves from many ocean observations (Garrett, Munk, 1979). The wave-wave interactions are thought to be responsible for the transfer of energy from low frequencies to small spatial scales developing a continuous wave spectrum. Such non-linear interactions are based on three-waves (triad), which have been often observed experimentally in the form of the parametric subharmonic instability (Joubaud et al., 2012; Maurer et al., 2016; Ghaemsaidi et al., 2016). For a review of resonant interactions of waves refer to Dauxois et al. (2018). However, the application of Weak Turbulence Theory to internal waves remains open (Lvov et al., 2004; Polzin, Lvov, 2011). In this section, a spatio-temporal analysis is performed in order to identify the presence of internal gravity waves. Furthermore, we focus on the phenomenon of wave-wave nonlinear interactions. In particular, we attempt to give answers to the two following questions: (i) are we able to generate turbulence driven by weakly nonlinear waves?, and (ii) where is this regime placed in the parameter space $\{F_{h,f}, \mathcal{R}_8\}$?

Spatio-temporal analysis have been often used to identify internal gravity waves in stratified turbulence (Lindborg, Brethouwer, 2007; Clark di Leoni et al., 2015). It requires saving a large amount of fields in time in order to resolve both small spatial and temporal scales. In this PhD work, I perform a spatio-temporal analysis of linear modes $\hat{a}_+ = N^2 \hat{u}_z + i\omega \hat{b}$ (see section 2.2 for the definition of the linear mode). One can express the spatio-temporal energy spectra of the linear mode \hat{a}_+ as

$$E_a(k_x, k_z, \omega) = \frac{1}{N_F} \sum_{N_F} \left(\frac{1}{2} \frac{1}{\delta k_x} \frac{1}{\delta k_z} \frac{1}{\delta \omega} |\tilde{a}_+(k_x, k_z, \omega)|^2 \right), \quad (5.1)$$

where N_F is the number of temporal Fourier transforms performed, $\delta k_x = 2\pi/L_x$, $\delta k_z = 2\pi/L_z$ and $\delta \omega = 2\pi/T$. L_x and L_z are the horizontal and vertical sizes of the numerical domain. The temporal Fourier transform is performed over a windows size given by T . The $\hat{a}_+(k_x, k_z, \omega)$ is the spatio-temporal Fourier transform of the linear mode \hat{a}_+ expressed as

$$\hat{a}_+(k_x, k_z, \omega) = \frac{1}{L_x} \frac{1}{L_z} \frac{1}{T} \int_0^{L_x} \int_0^{L_z} \int_0^T a_+(\mathbf{x}, t) e^{-i(\mathbf{k}\mathbf{x} - \omega t)} dx dz dt. \quad (5.2)$$

5.1 The spatio-temporal energy spectra

The spatio-temporal energy spectra is computed for three different regimes in 2D stratified turbulence. Figure 5.1 displays, in red, the three simulations used to perform the spatio-temporal analysis. They correspond to the three different regimes: (a) weakly stratified regime, (b) strongly stratified weakly affected by the viscosity, and (c) strongly stratified viscosity-affected regime. We start saving the fields once the statistically stationary regime is reached. The Fourier transform is computed over a windows size $T = 50(2\pi/N)$. The spatio-temporal Fourier transform of a signal assumes periodicity in both, spatial $L_{x,z}$ and temporal T , domains. As it is mentioned in chapter 3, the spatial domain has periodic boundary conditions. The signal in spatial domain is thus $L_{x,z}$ periodic. Nevertheless, the signal in the temporal domain is not T periodic. In order to overcome this issue, I use a classical Hanning function as a windowing function. Table 5.1 shows the numerical parameters for the computation of the spatio-temporal spectra.

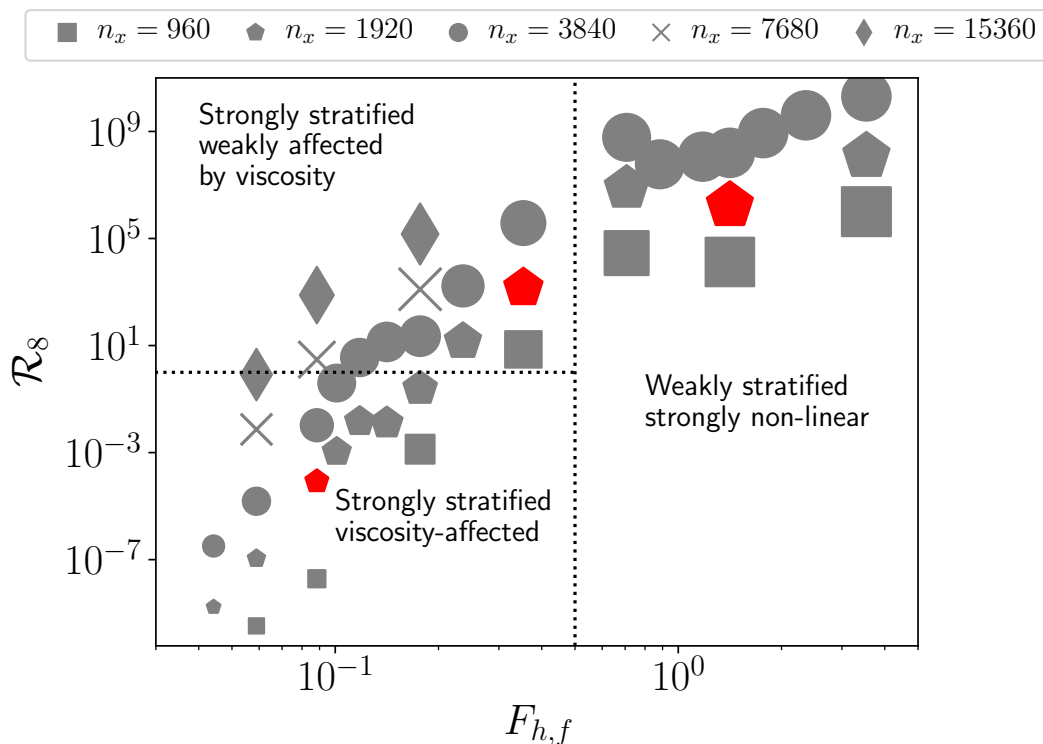


Figure 5.1: All simulations displayed in the parameter space $\{F_{h,f}, \mathcal{R}_8\}$. The marker shape indicates the numerical resolution. The simulations used to compute the spatio-temporal energy spectra are displayed in red. They correspond to three different regimes: (a) weakly stratified regime, (b) strongly stratified weakly affected by the viscosity, and (c) strongly stratified viscosity-affected regime.

The spatio-temporal energy spectra has three dimensions $E(k_x, k_z, \omega)$. We are thus forced to display the spectra by means of cross-sections. Figure 5.2 shows cross-sections of $\log_{10} E^*(k_x, k_z, \omega)$ for given values of k_z and for the three regimes: (a) weakly stratified turbulence and strongly non-linear, (b) strongly stratified weakly affected by the viscosity, and (c) strongly stratified viscosity-affected regime. $E^*(k_x, k_z, \omega)$ is the non-dimensional spatio-temporal energy spectra. We consider that the spatio-temporal energy spectra has dimensions $E_a \sim L^4 T^{-5}$. One could thus normalize the spectra by a quantity representing the forcing with the same dimensions which is expressed as

$$E_{norm} = N^4 (PL_f^{10})^{1/3}. \quad (5.3)$$

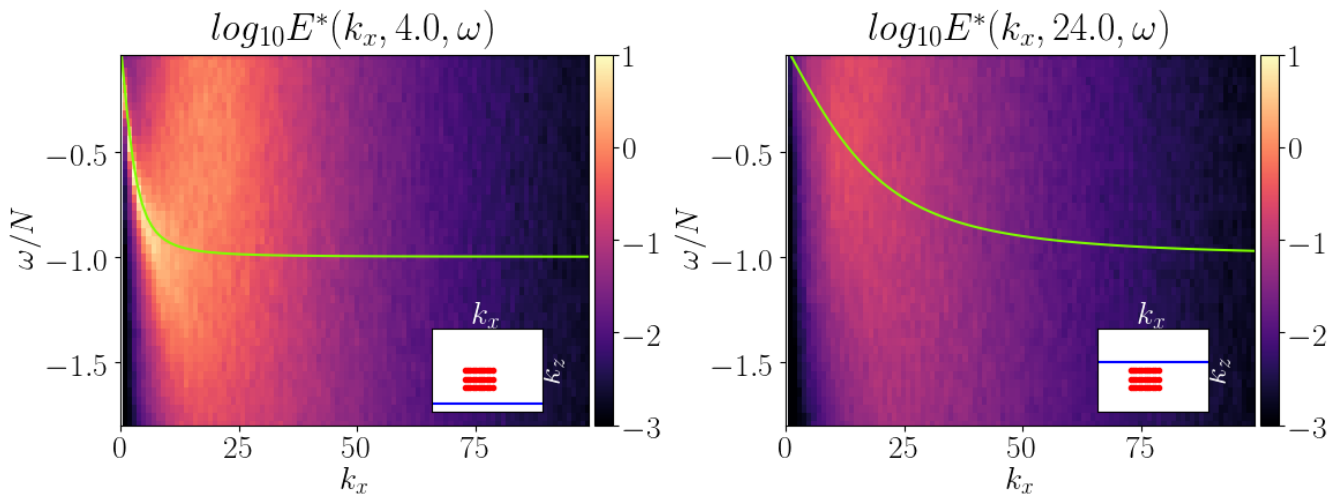
| γ | $F_{h,f}$ | $\mathcal{R}_8 = Re_8 F_h^8$ | ν_8 |
|----------|-----------|------------------------------|----------|
| 0.5 | 1.41 | 1.7e+06 | 6.37e-21 |
| 2 | 0.35 | 1.4e+03 | 4.48e-21 |
| 8.0 | 0.09 | 8.4e-05 | 7.93e-21 |

Table 5.1: Overview of the numerical parameters for the computation of the spatio-temporal energy spectra for three different stratification strengths. The numerical resolution of the simulations is 1920×480 . The stratification strength is given by the value of γ . The forcing horizontal Froude number is expressed as $F_{h,f}$. \mathcal{R} is the buoyancy Reynolds number. ν_8 is the hyper-viscosity coefficient. The windows size of the temporal Fourier transform is $T = 50(2\pi/N)$.

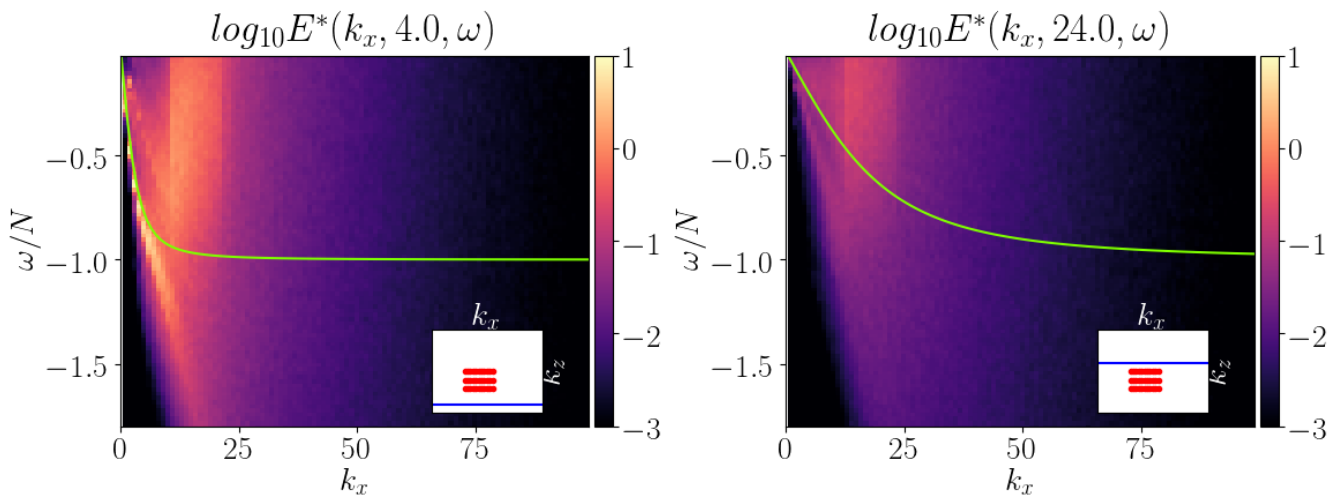
P is the energy injection rate and L_f is the forcing scale. This normalization allow us to compare the spatio-temporal energy spectra for the three different regimes. The cross-sections of figure 5.2 correspond to different values of the vertical wavenumber k_z . The green curve corresponds to the linear dispersion relation of internal gravity waves. The inset plot represents the spectral space with the forcing region (red square) and the cross-section (blue line). For the strongly stratified case (figure 5.2 (b)), the energy is less scattered than in the weakly stratified case (figure 5.2 (a)). In figure 5.2 (b), one can observe that the concentration of energy is offset by the curve of the dispersion relation. It might be due to the Doppler shifts observed also in Clark di Leoni et al. (2015). They observed that waves associated with low wavenumbers have a modified frequency due to the advection of the large scale flow. For the three regimes, we can observe always waves in the flux loop at horizontal scales larger than the forcing scale. Internal waves at low horizontal wavenumbers have been also reported in Lindborg, Brethouwer (2007). In figure 5.2 (c), one can observe more energy concentrated around the dispersion relation than in figures 5.2 (b) and (c). It might be due to the fact that the dynamics are affected by the viscosity, i.e. less non-linear. To conclude, decreasing $F_{h,f}$ implies the concentration of energy around the linear dispersion relation with the Doppler shift.

Figure 5.3 displays cross-sections of $\log_{10} E^*(k_x, k_z, \omega)$ for given values of k_x . Like in figure 5.2, the energy concentrates around the dispersion relation for low wavenumbers for the three cases with a strong concentration at low $F_{h,f}$. The energy concentration is less clear at large horizontal wavenumbers (right column), which it spreads from the dispersion relation (5.3, (c)). The scattering of energy from the dispersion relation curve (green line) can be interpreted as a measure of the non-linearity of the dynamics (Mordant, Miquel, 2017).

(a) Weakly stratified regime $\{F_{h,f} = 1.4, \mathcal{R}_8 = 1.7 \cdot 10^6\}$



(b) Strongly stratified weakly-affected by the viscosity $\{F_{h,f} = 0.35, \mathcal{R}_8 = 1.4 \cdot 10^3\}$



(c) Strongly stratified strongly-affected by the viscosity $\{F_{h,f} = 0.09, \mathcal{R}_8 = 8.4 \cdot 10^{-5}\}$

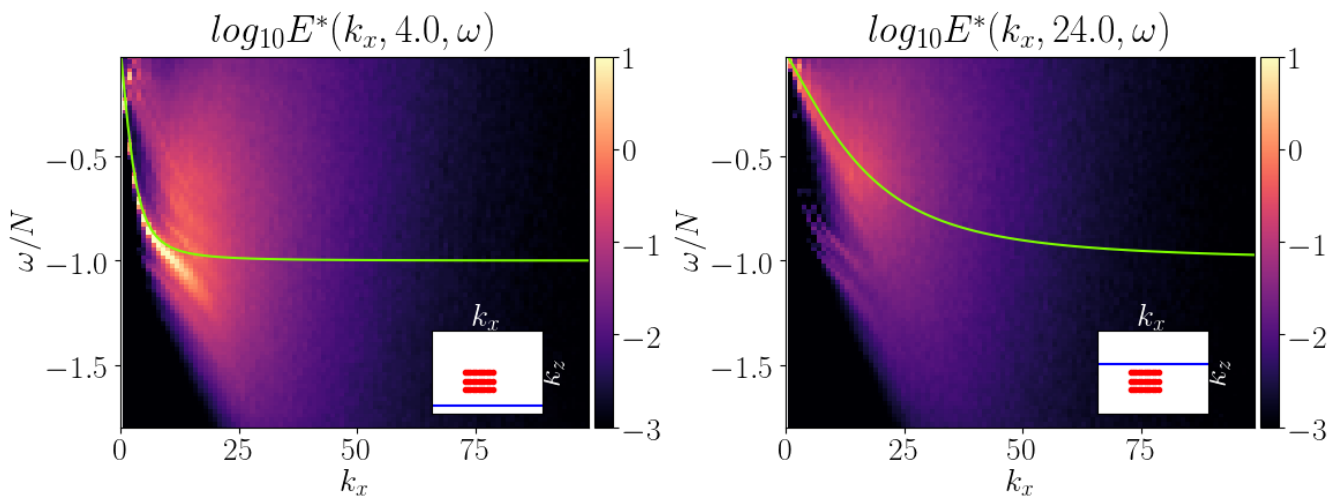
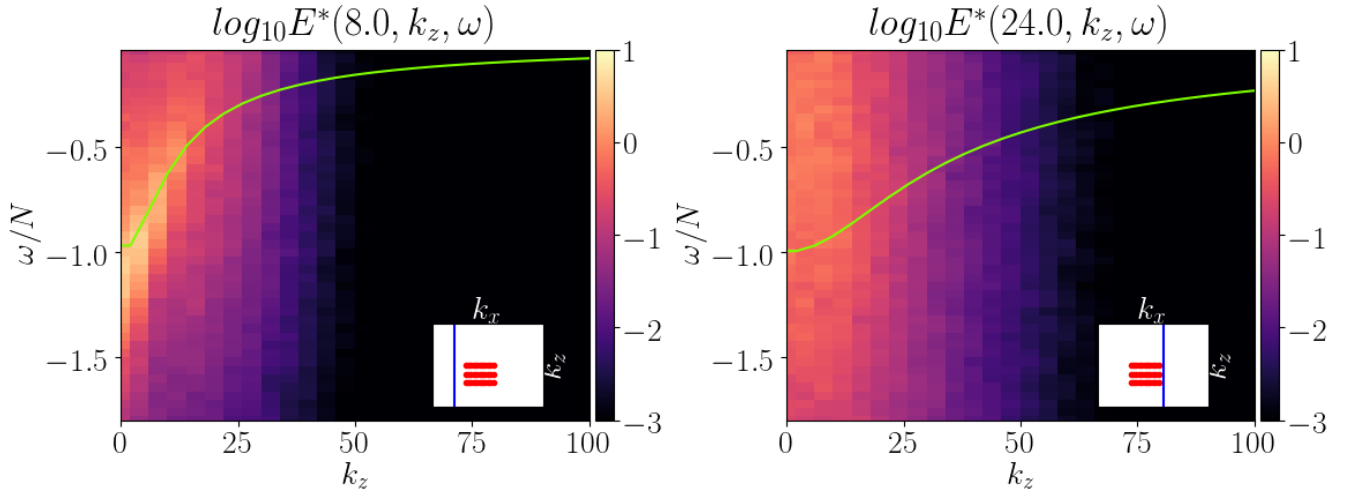
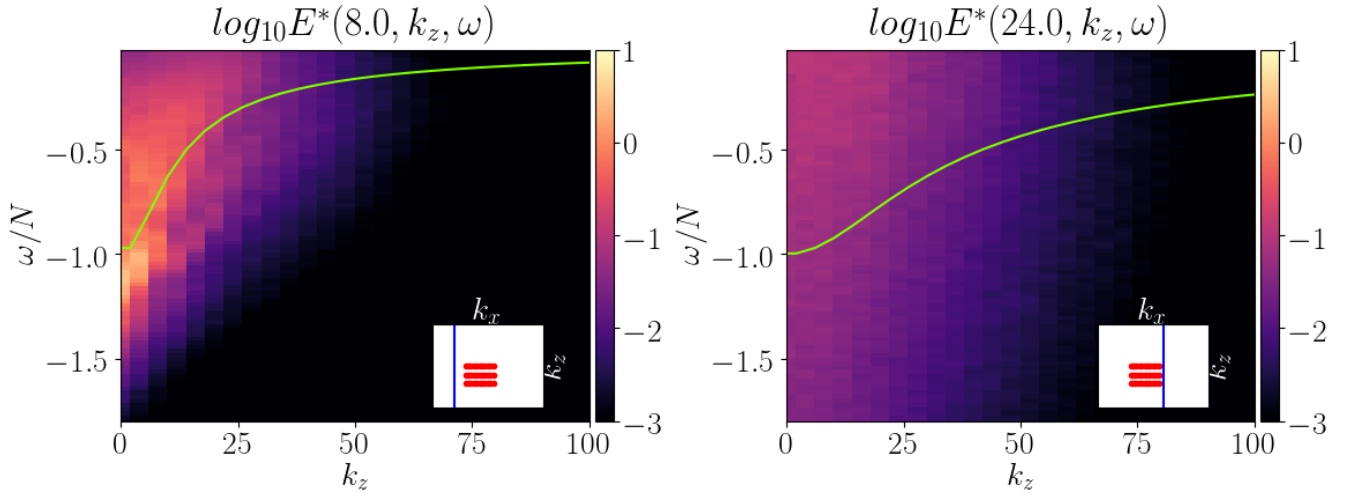


Figure 5.2: Cross-sections $\log_{10} E^*(k_x, k_z, \omega)$ of the non-dimensional spatio-temporal energy spectra for two given values of k_z : $k_z = 4 \text{ rad/m}^{-1}$ (left column) and $k_z = 24 \text{ rad/m}^{-1}$ (right column), and for the three different regimes. The frequency ω is normalized by N . The green line represents the dispersion relation $\omega(k_x, k_z)$. The inset graph represents the space (k_x, k_z) . The forcing modes are displayed in red and the blue line shows the position of the displayed cross-section.

(a) Weakly stratified regime $\{F_{h,f} = 1.4, \mathcal{R}_8 = 1.7 \cdot 10^6\}$



(b) Strongly stratified weakly-affected by the viscosity $\{F_{h,f} = 0.35, \mathcal{R}_8 = 1.4 \cdot 10^3\}$



(c) Strongly stratified strongly-affected by the viscosity $\{F_{h,f} = 0.09, \mathcal{R}_8 = 8.4 \cdot 10^{-5}\}$

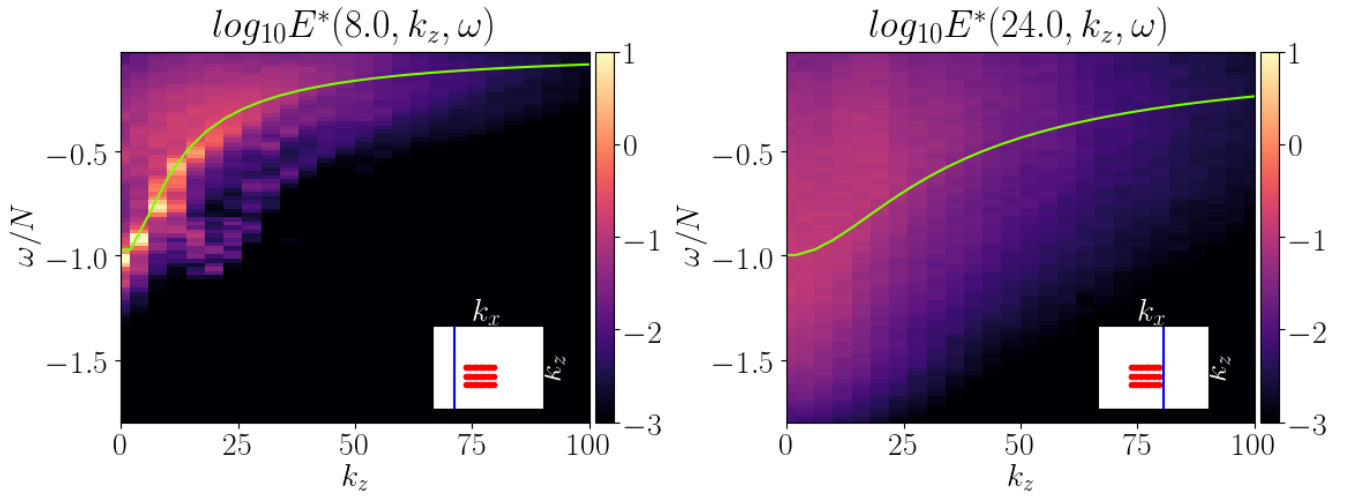
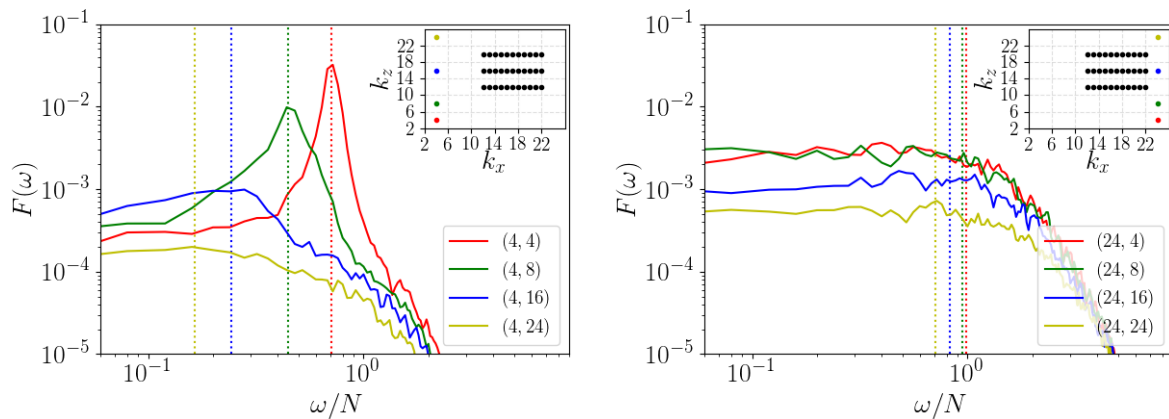


Figure 5.3: Same caption as figure 5.2 for cross-sections $\log_{10} E^*(k_x, k_z, \omega)$ and for $k_x = 8$ rad/m^{-1} (left column) and $k_x = 24$ rad/m^{-1} (right column).

Figure 5.4 displays the frequency spectra $E(k_x, k_z, \omega)$ in the logarithmic scale for four individual modes. The frequency axis ω is normalized by the buoyancy frequency N . The inset plot displays the position of these Fourier modes in relation to the forcing modes (black dots). The vertical dotted lines correspond to the internal gravity waves frequency associated with the Fourier modes. For both regimes, we observe that the peaks at low frequencies are perfectly aligned with the vertical lines at modes with lower wavenumbers than the forcing modes (see red and green lines of the left column of the figure 5.4). It confirms again the presence of large-scale internal gravity waves as observed in figures 5.2 and 5.3. Furthermore, the frequency spectra for the strongly stratified regime (figure 5.4, (b) left) contains more peaks than the frequency spectra for the weakly stratified case (figure 5.4, (a) left). In the strongly stratified case, the dynamics are indeed weakly non-linear. At horizontal wavenumbers larger than the forcing wavenumber $k_x > k_{f,x}$ (figure 5.4, right column), we do not peaks corresponding to the internal wave frequencies.

(a) Weakly stratified regime $\{F_{h,f} = 1.4, \mathcal{R}_8 = 1.7 \cdot 10^6\}$



(b) Strongly stratified strongly-affected by the viscosity $\{F_{h,f} = 0.09, \mathcal{R}_8 = 8.4 \cdot 10^{-5}\}$

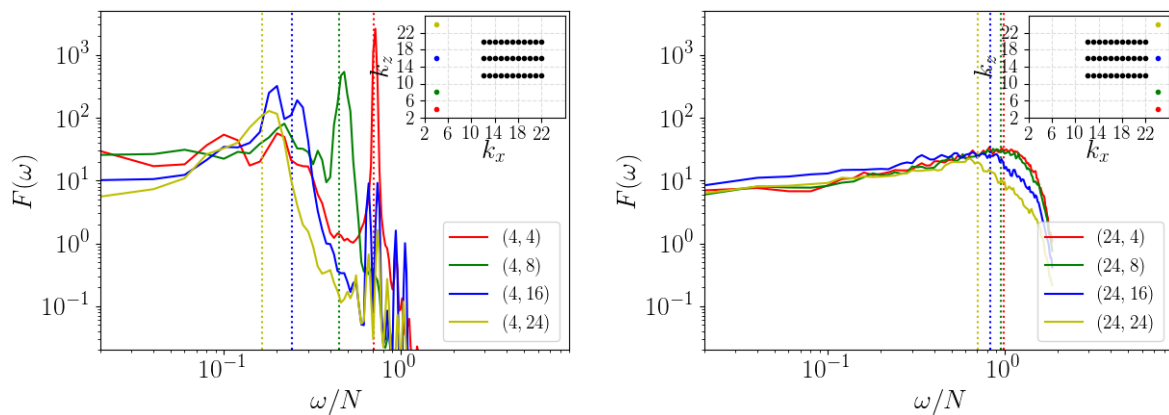


Figure 5.4: Frequency spectra $E(k_x, k_z, \omega)$ of individual Fourier modes, in the logarithmic scale, for the regimes (a) weakly stratified regime and (b) strongly stratified viscosity-affected regime. The frequency ω is normalized by the buoyancy frequency N . The inset plot displays the forcing modes (black dots) and the Fourier modes for which the frequency spectra is computed. The vertical dotted lines correspond to the frequency of the internal gravity waves for the four Fourier modes.

In the wave energy spectrum model proposed by Garrett, Munk (1979), the frequency spectrum displays a ω^{-2} power-law for $\omega_f < \omega < N$, being ω_f the excitation frequency. As it has been mentioned before, this model has been reconstructed from oceanic observations such as the moored measurements performed by Cairns (1975). Figure 5.5 displays the frequency spectra of the vertical displacement of the isotherms extracted from Cairns (1975). The red arrow shows the characteristic frequency of the excitation by tides in cph which is $\omega_f \sim 0.08$ cph. Considering a buoyancy frequency of the ocean $N \sim 0.02\text{s}^{-1} \sim 70$ cph, N is out of the plot. One can observe that the frequency spectrum of this oceanic measurement displays a ω^{-2} power-law.

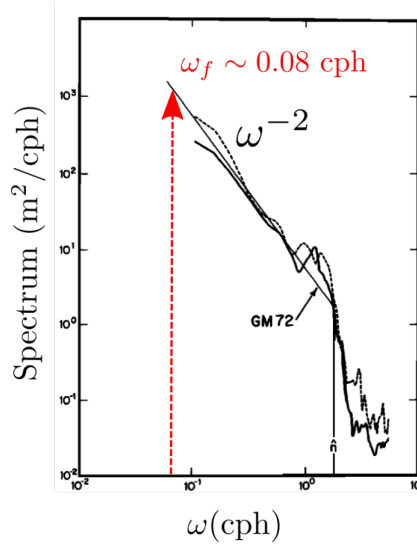


Figure 5.5: Frequency spectra of the vertical displacement of the isotherms measured at $30^{\circ}20'N$, $121^{\circ}20'W$ on June 1973. The image has been extracted from Cairns (1975).

Figure 5.6 (a) displays the normalized frequency spectrum for the three regimes in 2D stratified turbulence. The spectrum is computed directly as $E(\omega) = \sum_{\mathbf{k}} E(k_x, k_z, \omega)$, and is normalized by the quantity $N^4(PL_f^4)^{1/3}$. Figure 5.6 (b) displays the frequency spectrum of the DNS extracted from Le Reun et al. (2018). We first focus on figure 5.6 (a), which contains a peak at $\omega/\omega_l \sim 1$, corresponding to the forcing frequency of the simulations. For $\omega < \omega_l$, we observe a flat spectrum similar to those observed in experiments of turbulence driven by internal gravity waves carried out at the Coriolis platform (LEGI, France). Unlike the work of Le Reun et al. (2018), we excite high-frequencies close to N , preventing the development of the ω^{-2} power-law. We need therefore to increase the gap between the characteristic forcing and buoyancy frequencies.

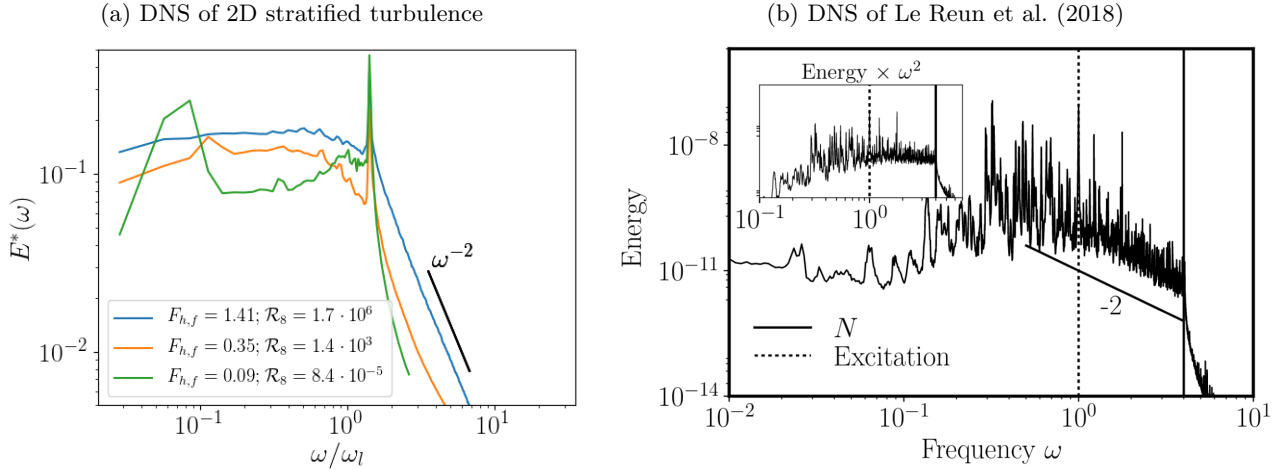


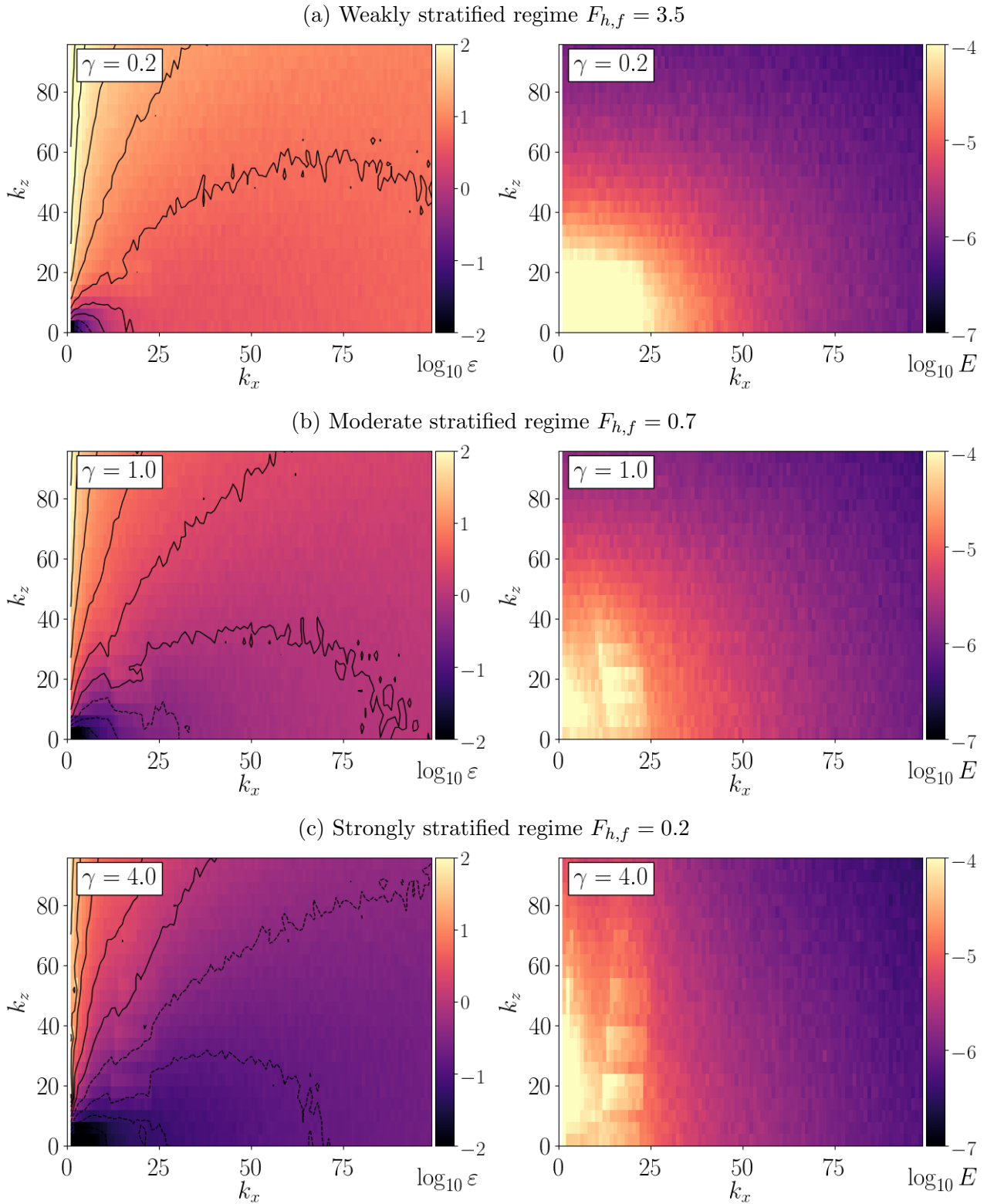
Figure 5.6: Normalized frequency spectrum $E^*(\omega)$ for three different regimes (a), calculated directly as $E(\omega) = \sum_{\mathbf{k}} E(k_x, k_z, \omega)$. $E^*(\omega)$ is normalized by the quantity $N^4(PL_f^4)^{1/3}$ and frequency axis is normalized by the characteristic frequency of the forced waves $\omega_l = N \sin \theta_f$. (b) Frequency spectrum of the DNS of Le Reun et al. (2018).

5.2 Where are internal waves most likely to develop?

In the previous section, we have observed that the energy concentrates along the linear dispersion relation of internal gravity waves at low wavenumbers. It indeed confirms the presence of large-scale waves. In this section, we analyze in which modes internal gravity waves are most likely to occur. We use the non-dimensional quantity ε , which is the ratio between a linear and non-linear time scale expressed as

$$\varepsilon = \frac{\tau_l}{\tau_{nl}} = \frac{k^2 \sqrt{E}}{N \sin \theta_k} \quad (5.4)$$

Internal gravity waves are most likely to occur for values of $\varepsilon \ll 1$, i.e. $\tau_l \ll \tau_{nl}$. Figure 5.7 displays the value of ε in the spectral space (left column) and the two-dimensional energy spectra $E(k_x, k_z)$ (right column). The black contours in the left column represents the isolines for the value of $\log_{10} \varepsilon$. Both fields are displayed in the logarithmic scale. The field of ε indicates in which modes the linear time is smaller than the non-linear time, i.e. small value of $\log_{10} \varepsilon$ (dark region). When we decrease $F_{h,f}$, the dark region associated with low horizontal and vertical wavenumbers increases its size. The domain of weak non linearity is thus anisotropic, with a wider extension in k_x than in k_z . In all cases the non-linearity is strong at small scales. Our observation is in qualitative agreement with the 3D DNS of Yokoyama, Takaoka (2019) (see figure 7 of this reference). In order to have a true weakly non-linear regime not affected by viscosity, we need to further decrease $F_{h,f}$ and increase the resolution keeping $\mathcal{R}_s \geq 1$.



In order to quantify the energy contained in modes within the linear region ($\varepsilon < 1$), we use the ratio

$$\mathcal{R}_l = \frac{E_l}{E}, \quad (5.5)$$

which is the energy contained in the linear modes E_l over the total energy E . E_l and E are computed from the two-dimensional energy spectra $E(k_x, k_z)$. Figure 5.8 displays the ratio \mathcal{R}_l as function of the forcing Froude number $F_{h,f}$. The color of the markers represents the different numerical resolution n_x . For $F_{h,f} > 0.7$, \mathcal{R}_l increases when the stratification strength is increased. Surprisingly, for $F_{h,f} < 0.7$, the ratio \mathcal{R}_l decreases. It can be explained by the fact that, when the stratification is increased, the energy concentrates at strongly non-linear modes, low k_x and large k_z (see figure 5.9).

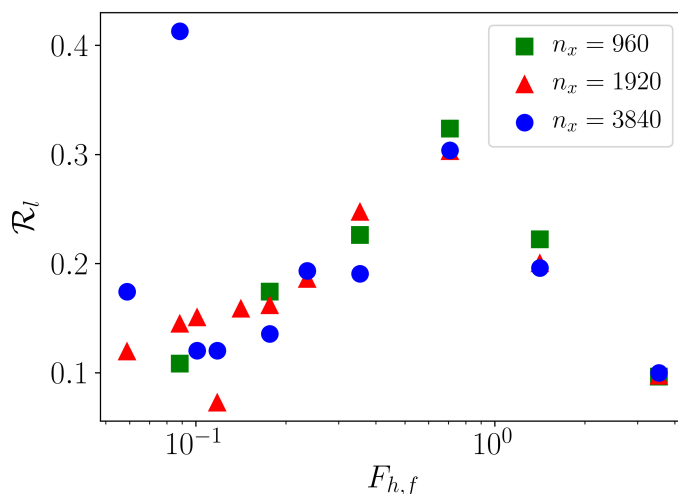


Figure 5.8: \mathcal{R}_l against the forcing Froude number $F_{h,f}$ for different numerical resolutions.

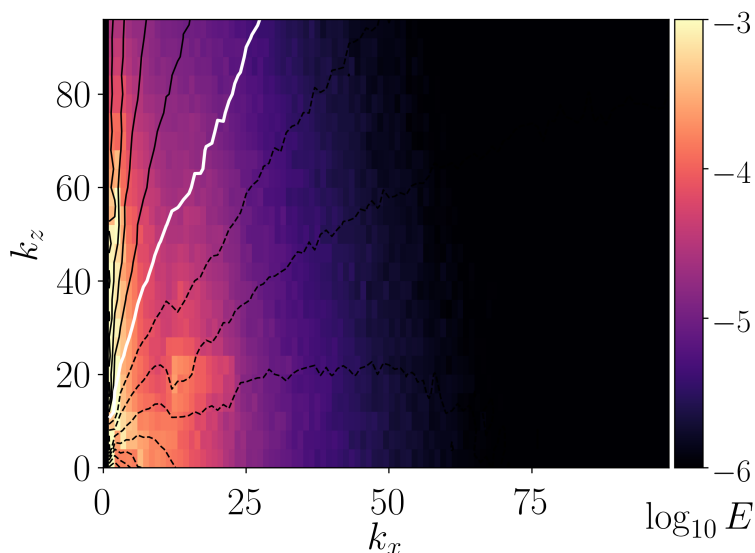


Figure 5.9: 2D energy spectrum in logarithmic scale for the strongly stratified regime $F_{h,f} = 0.09$. The dashed and solid curves display the isolines for values of $\varepsilon < 1$ and $\varepsilon > 1$, respectively. The white curve represents $\varepsilon = 1$.

Chapter 6

Effects of varying the forcing on 2D stratified turbulence

All simulations presented so far have been forced on the linear mode \hat{a}_+ , which excites waves propagating with the same direction as the wavevector \mathbf{k} . As it has been mentioned before, these waves are known as prograde waves. At this point, one may wonder whether the dynamics of 2D stratified turbulence depend on the forcing quantity or whether it is an universal regime. Several studies of 3D stratified turbulence (Waite, Bartello, 2004, 2006a) attempted to study numerically the degree of universality of the strongly stratified regime. The dynamics forced by large scale waves (Waite, Bartello, 2006a) differ from simulations forced with vortical modes (Waite, Bartello, 2004). In particular, the scaling $F_v \sim 1$ is not reached and they are not successful at reproducing the saturation spectrum $N^2 k_z^{-3}$ when forcing with waves. Lindborg, Brethouwer (2007) performed numerical simulations with a forcing either in vortical or wave modes. In both cases, they observe a forward energy cascade and inertial-range scaling of the horizontal kinetic and potential energy spectra. Furthermore, it is shown that the vertical forcing wavenumber $k_{v,f}$ is a crucial parameter when forcing waves. For large $k_{v,f}$, they show that the resulting dynamics forced with vortical and wave motions are similar, with an equipartition of kinetic energy in the inertial range.

In this chapter, we attempt to study numerically the effects of varying the forcing quantity on 2D stratified turbulence. Four different forcing schemes are thus analyzed: (a) linear mode \hat{a}_+ on $k_z > 0$, (b) linear mode \hat{a}_+ on both $k_z \gtrless 0$, (c) vorticity $\hat{\xi}$ on $k_z > 0$, and (d) vorticity $\hat{\xi}$ on $k_z \gtrless 0$. By forcing the vorticity $\hat{\xi}$, the injected energy is only kinetic energy. We force the vorticity equation instead of the momentum equation since the code `ns2d.strat` solves directly the vorticity equation (see equation (3.1)). When we force the linear mode, prograde waves \hat{a}_+ , the injected energy is equally kinetic and potential energy. All simulations presented in this chapter have a numerical resolution 1920×480 . Figure 6.1 displays the 2D energy spectra of the four different forcing schemes for the strongly stratified viscosity-affected regime $\{F_{h,f} = 0.18, \mathcal{R}_8 = 2 \cdot 10^{-1}\}$. One can observe that the linear mode \hat{a}_- does not have energy when forcing the linear mode \hat{a}_+ , (see figure 6.1 (a) and (b)). Forcing the vorticity $\hat{\xi}$ injects energy to both linear modes \hat{a}_+ and \hat{a}_- (see figure 6.1 (c) and (d)).

Figure 6.2 shows snapshots of the quantity b/N for two simulations forced on the linear mode \hat{a}_+ on $k_z > 0$ (a), and $k_z \gtrless 0$ (b) for the strongly stratified viscosity-affected regime $\{F_{h,f} = 0.2, \mathcal{R}_8 = 2 \cdot 10^{-1}\}$. Forcing the linear mode on $k_z > 0$ (figure 6.2 (a)) excites waves propagating only towards the top-right corner, i.e. $k_x > 0$ and $k_z > 0$. However, forcing the linear mode on $k_z \gtrless 0$ generates waves propagating towards top-right and bottom-right corner, simultaneously, producing thus smaller scales at early times of the simulation. The statistically stationary states seem to be similar in both cases (see figure

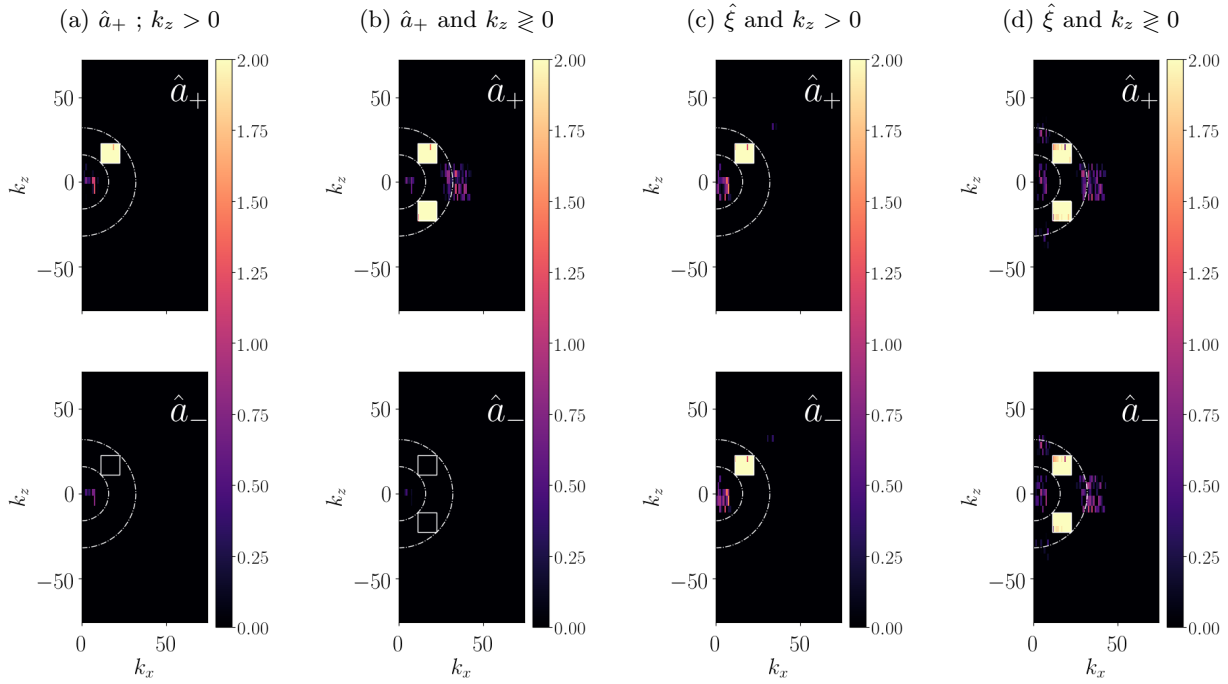


Figure 6.1: 2D energy spectra at the early time $t = 0.2\tau_{af}$, i.e. representing the forcing, for the four forcing schemes: (a) linear mode \hat{a}_+ on $k_z > 0$, (b) linear mode \hat{a}_+ on $k_z \geq 0$, (c) vorticity $\hat{\xi}$ on $k_z > 0$, and (d) vorticity $\hat{\xi}$ on $k_z \geq 0$ for the strongly stratified viscosity-affected regime $\{F_{h,f} = 0.18, \mathcal{R}_8 = 2 \cdot 10^{-1}\}$.

6.2 bottom left and right).

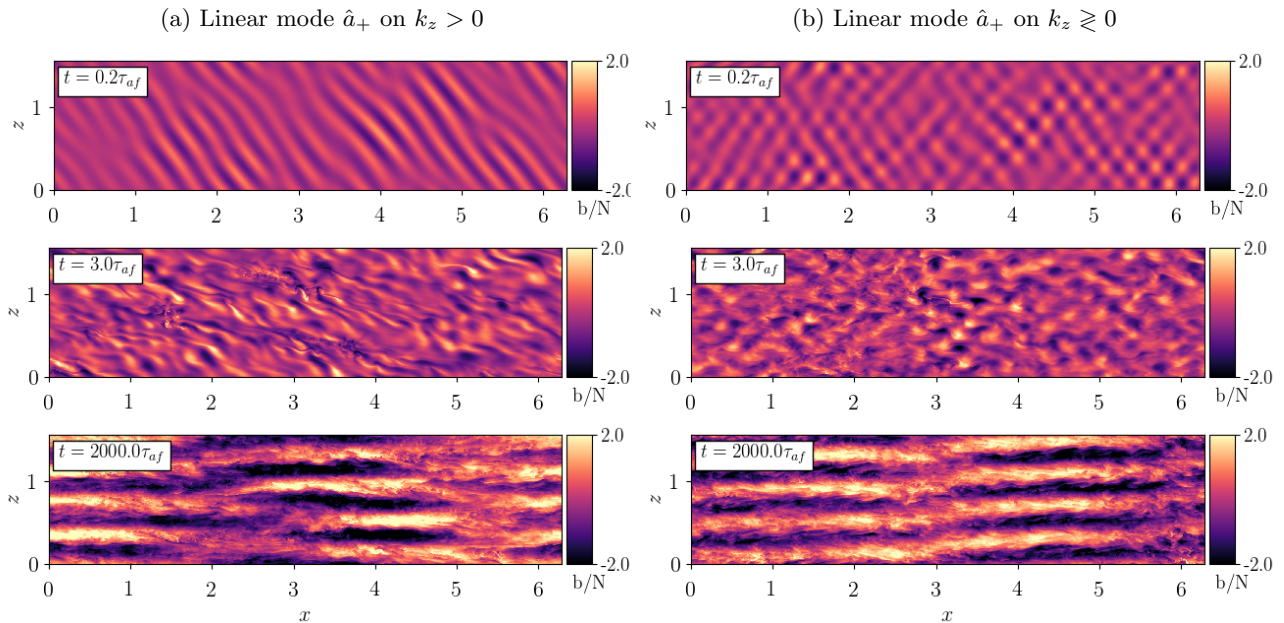


Figure 6.2: Snapshots of the field b/N of two simulations forced on the linear mode \hat{a}_+ on $k_z > 0$ (a), and $k_z \geq 0$ (b), and for the strongly stratified viscosity-affected regime $\{F_{h,f} = 0.18, \mathcal{R}_8 = 2 \cdot 10^{-1}\}$.

In order to study the effects of forcing on the dynamics, we compare simulations with different forcing schemes and for two different regimes. Figure 6.3 displays all simulations in the parameter space $\{F_{h,f}, \mathcal{R}_8\}$. The simulations analyzed in this chapter are displayed in red. They correspond to: (a) weakly stratified regime, and (b) strongly stratified viscosity-affected regime.

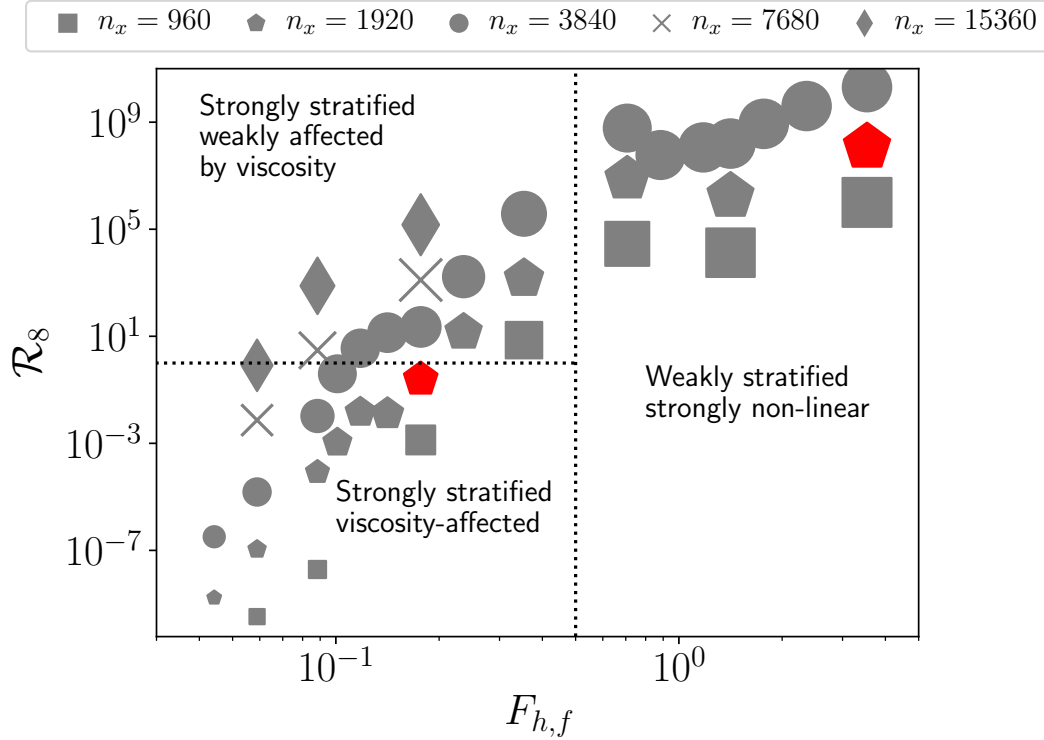


Figure 6.3: Same as in figure 5.1. The simulations analyzed in this section are displayed in red.

Figure 6.4 shows the time evolution of the averaged energy for the two regimes: (a) weakly stratified regime $\{F_{h,f} = 3.54, \mathcal{R}_8 = 1.2 \cdot 10^8\}$, and (b) strongly stratified viscosity-affected regime $\{F_{h,f} = 0.18, \mathcal{R}_8 = 2 \cdot 10^{-1}\}$. The averaged energy is normalized by P/ω_{af} , for a given energy injection rate P and ω_{af} is the characteristic forcing frequency. The green solid lines represent simulations forced on the vorticity $\hat{\xi}$. The black solid lines represent simulations forced on the prograde waves \hat{a}_+ . The dotted lines represent simulations forced also on negative values of k_z . For weakly stratified flows and at the stationary state, the line corresponding to the simulation forced on the vorticity ($\hat{\xi}$, green line) is different to the line corresponding to the simulation forced on the prograde waves (\hat{a}_+ , black line), meaning that the energy depends upon the quantity forced. It has to be noted that the magnitude of the energy is larger in those simulations forced on the vorticity $\hat{\xi}$ (green line, figure 6.4 (a)) than those forced on the prograde waves \hat{a}_+ (black line, figure 6.4 (a)). When the stratification is weak, we have a strong inverse cascade of kinetic energy. By forcing the vorticity $\hat{\xi}$ (green line), the energy injected is only kinetic energy. The energy will be transferred to larger scales through an inverse cascade mechanism before transferred to smaller scales and dissipated. By forcing the prograde waves \hat{a}_+ (black line), we inject potential and kinetic energy. The potential energy will be transferred to smaller scales and dissipated, resulting in a lower averaged energy. For strongly stratified flows (figure 6.4 (b)), the green and black lines tend to get closer at the stationary state although with strong fluctuations. It means that the energy of the simulations forced on the prograde waves is somewhat similar to the energy forced on vorticity.

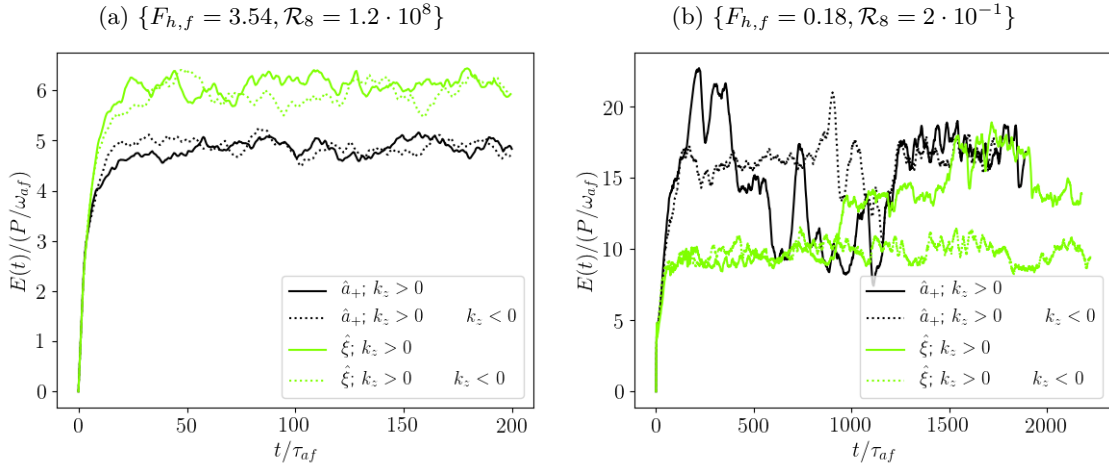


Figure 6.4: Temporal evolution of the normalized averaged energy for (a) weakly stratified regime $\{F_{h,f} = 3.54, \mathcal{R}_8 = 1.2 \cdot 10^8\}$ and (b) strongly stratified regime viscosity-affected regime $\{F_{h,f} = 0.18, \mathcal{R}_8 = 2 \cdot 10^{-1}\}$ and for different forcing schemes: vorticity $\hat{\xi}$ (green lines) ; prograde waves \hat{a}_+ (black lines). The solid lines correspond to simulations forced only on $k_z > 0$. The dashed line corresponds to simulations forced on $k_z \geq 0$.

Figure 6.5 displays the 2D energy spectra at the statistically stationary state with four different forcing schemes and for the weakly stratified regime $\{F_{h,f} = 3.54, \mathcal{R}_8 = 1.2 \cdot 10^8\}$. When forcing \hat{a}_+ , the linear mode \hat{a}_- contains less energy than \hat{a}_+ . However, when forcing the vorticity $\hat{\xi}$, both \hat{a}_+ and \hat{a}_- have similar energy since both linear modes are forced directly. Furthermore, we do not see any clear qualitative difference at the steady state when forcing \hat{a}_+ and the vorticity $\hat{\xi}$ (see figure 6.5 (a) and (c)).

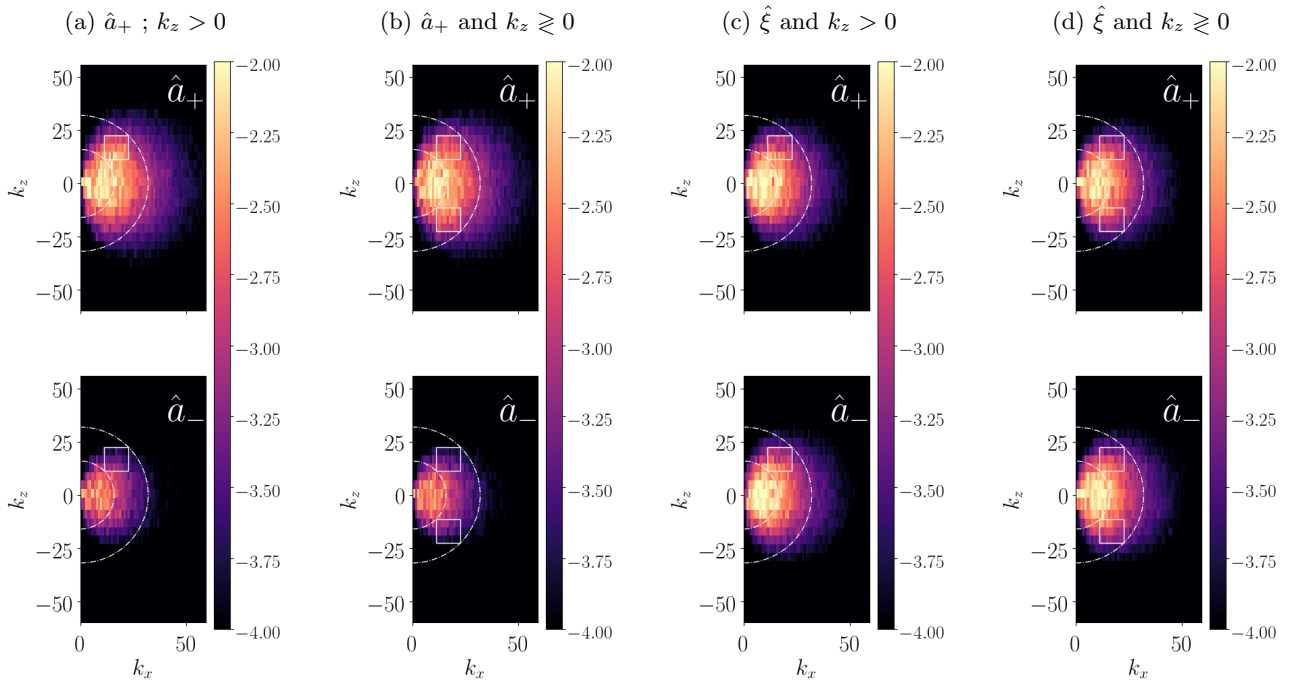


Figure 6.5: 2D energy spectra at the statistically stationary state for the four forcing schemes and for the weakly stratified regime $\{F_{h,f} = 3.54, \mathcal{R}_8 = 1.2 \cdot 10^8\}$.

Figure 6.6 displays the 2D energy spectra for the strongly stratified viscosity-affected regime $\{F_{h,f} = 0.18, \mathcal{R}_8 = 2 \cdot 10^{-1}\}$. Unlike the weakly stratified case, we observe squares at modes $k_z > k_{f,z}$, which correspond to the harmonics of the forcing. The difference between the four cases is much weaker than for the weakly stratified case. We can conclude that the observed steady state has some degree of universality.

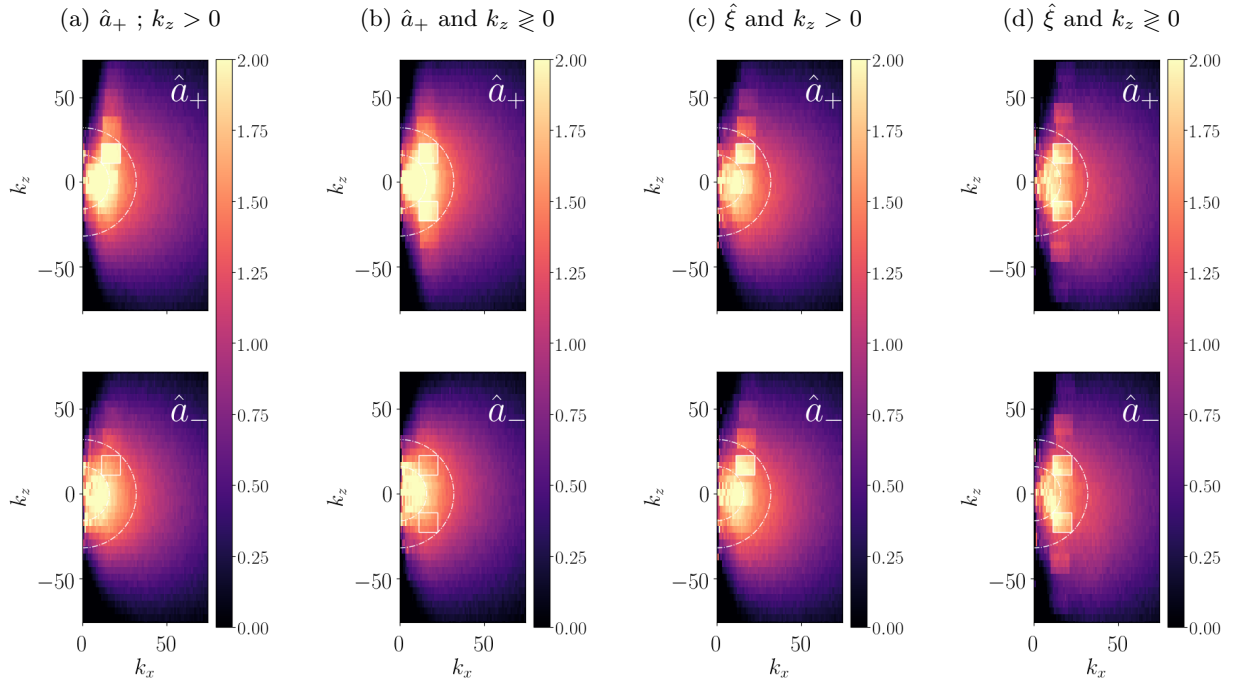


Figure 6.6: Same as figure 6.5 for the strongly stratified viscosity-affected regime $\{F_{h,f} = 0.18, \mathcal{R}_8 = 2 \cdot 10^{-1}\}$.

Chapter 7

Conclusions and perspectives

In this thesis, we have studied 2D stratified turbulence by means of direct numerical simulations of the 2D Navier-Stokes equations with the Boussinesq approximation constrained in a vertical plane and with an hyper-viscosity ν_8 . The main motivation is to be able to run high-resolution DNS for long times and for strong stratification with a moderate computational cost. The simulations are forced on the linear mode of the Navier-Stokes operator and on a localized region of the spectral space, so that only waves with similar time scale are excited. Three regimes have been identified in 2D stratified turbulence depending on the value of $F_{h,f}$ and \mathcal{R}_8 : (i) weakly stratified regime $\{F_{h,f} > 0.5\}$, (ii) strongly stratified regime weakly-affected by the viscosity $\{F_{h,f} > 0.5 \text{ and } \mathcal{R}_8 > 1\}$, and (iii) strongly stratified viscosity-affected regime $\{F_{h,f} > 0.5 \text{ and } \mathcal{R}_8 < 1\}$. For the weakly stratified regime, the flow is isotropic at large scales and dissipative scales. For strongly stratified flows, large horizontal layers with small vertical layers emerge in the flow, enhancing anisotropy at large scales. Strongly stratified weakly-affected by the viscosity support isotropic dissipative scales, while viscosity-affected strongly stratified flows contain anisotropic dissipative scales. Analogously to 3D stratified turbulence and for the strongly stratified regime weakly affected by the viscosity, we have observed that the flow develops a vertical scale similar to the buoyancy length scale $l_v \sim U/N$ in agreement with Billant, Chomaz (2001); Lindborg (2006). Furthermore, for $k_{f,x} < k_x < k_b$, we have observed that the horizontal energy spectra scales with a k_x^{-2} power-law with an equipartition between the kinetic and potential energies, which is interpreted as a subject of internal gravity waves. Moreover, a bump on the horizontal kinetic energy spectrum is observed at horizontal wavenumbers slightly larger than the buoyancy wavenumber $k_x \gtrsim k_b$. It seems to be in agreement with previous numerical studies of stratified turbulence (Waite, 2011; Augier et al., 2015).

In chapter 5, we have performed an spatio-temporal analysis of the three different regimes. For the three regimes, we observe a concentration of energy along the dispersion relation for $k < k_f$, confirming therefore the presence of internal gravity waves at large horizontal scales in agreement with Lindborg, Brethouwer (2007). We can conclude that waves are always present in the flux loop at horizontal scales larger than the forcing scale. At small scales, the energy concentration along the dispersion relation is less clear, which means that non-linearity is strong in small-scale dynamics. Furthermore, we have analyzed at which modes the linear time is smaller than the non-linear time, indicating thus where internal gravity waves are most likely to occur. We have observed that when we increase the stratification strength the region of the spectral space where waves (weak non-linearity) can occur also increases. It increases with a wider extension in k_x than in k_z . This observation is in agreement with the work of Yokoyama, Takaoka (2019). In chapter 6, we have studied the effects on the dynamics of varying the forcing quantity. Four different forcing schemes have been used: linear mode \hat{a}_+ and $k_z > 0$, linear mode \hat{a}_+

and $k_z \geq 0$, vorticity $\hat{\xi}$ and $k_z > 0$, and vorticity $\hat{\xi}$ and $k_z \geq 0$. We have not observed any clear qualitative difference when forcing on the vorticity or on the linear mode, suggesting some degree of universality of 2D stratified turbulence with respect to the forcing scheme.

Perspectives. Larger resolution numerical simulations, i.e. larger buoyancy Reynolds number \mathcal{R}_8 with lower horizontal Froude number F_h , need to be performed to resolve the Ozmidov scale and to attain regimes similar those observed in nature. In particular, further spatio-temporal analysis are required for a better understanding of energy fluxes.

For the strongly stratified regime weakly-affected by the viscosity, we have observed the presence of slow-propagating internal gravity waves associated with low k_x and large k_z . All simulations in this thesis are forced on a localized region of the spectral space with an angle $\theta_f = 45^\circ$ respect to the vertical direction, meaning that we force modes with a frequency close to the buoyancy frequency $\omega_f \sim N$. We could thus decrease θ_f in order to force modes with low frequencies, which is similar to the excitation frequencies observed in nature. Internal gravity waves in the ocean are usually excited by tides with a frequency similar to the Coriolis frequency $\omega_f \sim f \ll N$. We have started to perform numerical simulations with $\theta_f = 12^\circ$, which its buoyancy field and energy spectra are displayed in figure 7.1. We observe that the horizontal energy spectra (solid lines) scales with k_x^{-2} power-law for $k_{f,x} < k_x < k_b$ with an equipartition between the kinetic and potential energy, suggesting that the energy transfer on these modes is a signature of waves.

Finally, 3D high resolution numerical simulations are needed to be able to compare with the recent experimental work on turbulence driven by weakly non-linear internal gravity waves. These simulations are extremely challenging due to the high computational cost. For weakly non-linear regimes, the simulations need to be computed for very long times since the non-linear time scale is considerably larger than the linear time scale $\tau_{NL} \gg \tau_L$. An intermediate step to a 3D configuration could be to have a strong anisotropic domain with one horizontal dimension very large in comparison to the other dimensions "pencil domain", supporting thus the presence of vertical vorticity. The "pencil" configuration would allow us to simulate flows with a large Reynolds number in the horizontal with 3D effects for a reasonable computational cost.

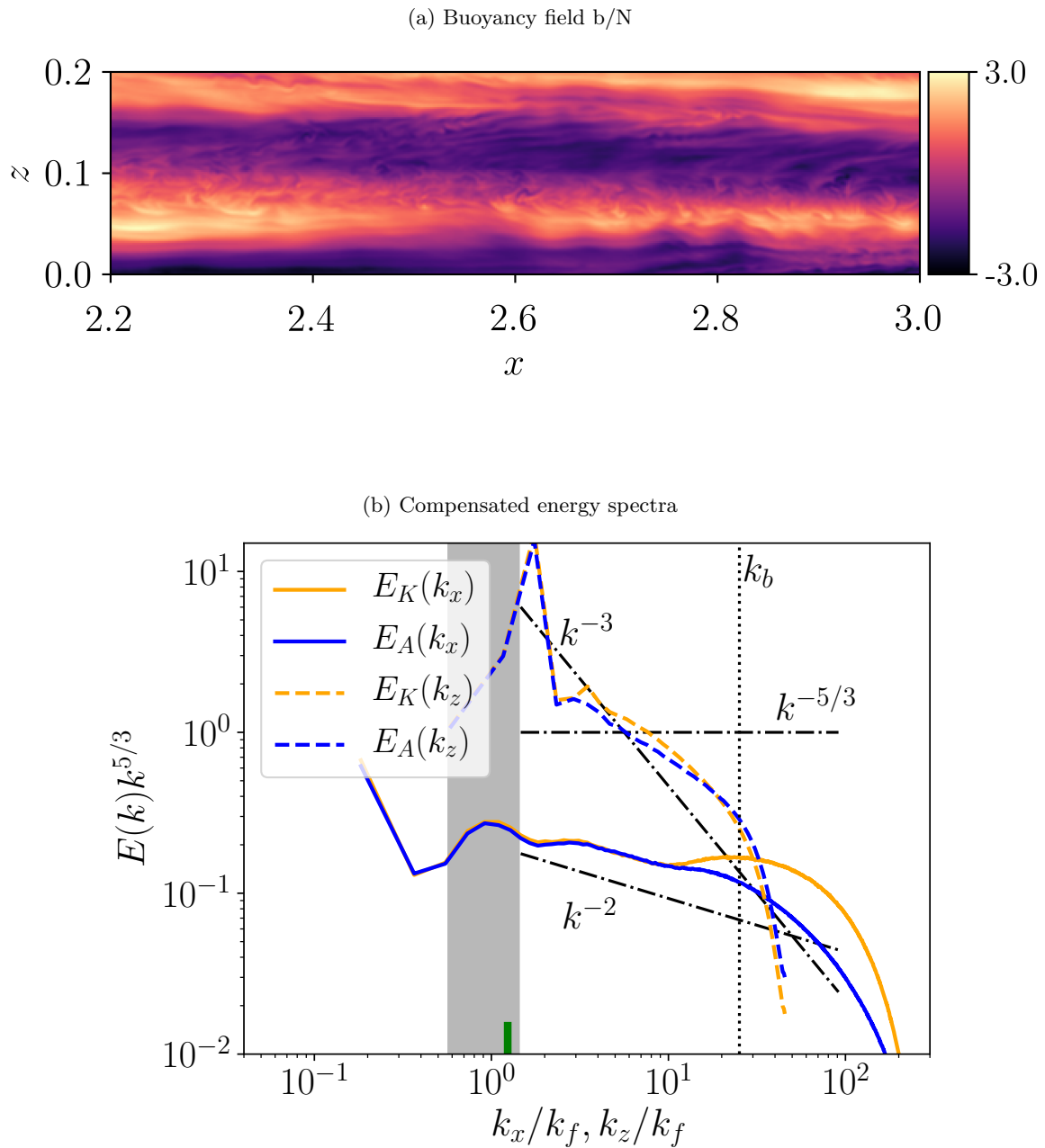


Figure 7.1: (a) Snapshot of the buoyancy field b/N , and (b) compensated energy spectra for simulation $F_{h,f} = 0.09$ with a forcing angle $\theta_f = 12^\circ$ forced on the linear mode \hat{a}_+ on $k_z > 0$. The spatial resolution of the simulation is 3840×240 with a domain size $L_x = 2\pi = 16L_z$

Bibliography

- Augier P.* Turbulence en milieu stratifié, étude des mécanismes de la cascade. 2011.
- Augier P., Billant P., Chomaz J.M.* Stratified turbulence forced with columnar dipoles: numerical study // *Journal of Fluid Mechanics*. 2015. 769. 403–443.
- Augier P., Billant P., Negretti M.E., Chomaz J.M.* Experimental study of stratified turbulence forced with columnar dipoles // *Physics of Fluids*. 2014. 26.
- Augier P., Mohanan A. V., Bonamy C.* FluidDyn: A Python Open-Source Framework for Research and Teaching in Fluid Dynamics by Simulations, Experiments and Data Processing // *J. Open Research Software*. 2019. 7.
- Bartello P.* Geostrophic adjustment and inverse cascades in rotating stratified turbulence // *Journal of Atmospheric Sciences*. 1995. 52. 4410–4428.
- Billant P., Chomaz J. M.* Experimental evidence for a new instability of a vertical columnar vortex pair in a strongly stratified fluid // *Journal of Fluid Mechanics*. 2000a. 418. 167–188.
- Billant P., Chomaz J.M.* Self-similarity strongly stratified inviscid flows // *Physics of Fluids*. 2001. 13. 1645–1651.
- Boffetta G., De Lillo F., Mazzino A., Musacchio S.* A flux loop mechanism in two-dimensional stratified turbulence // *Europhysics Letters*. 2011. 95, 3.
- Bourget B., Dauxois T., Joubaud S., Odier P.* Experimental study of parametric subharmonic instability for internal plane waves // *J. Fluid Mech.* 2013. 723. 1–20.
- Brethouwer G., Billant P., Lindborg E., Chomaz J.M.* Scaling analysis and simulation of strongly stratified turbulence // *Journal of Fluid Mechanics*. 2007. 585. 343–368.
- Broecker W. S.* Does the trigger for abrupt climate change reside in the ocean or in the atmosphere? // *Science*. 2003. 300. 1519–1522.
- Caillol P., Zeitlin V.* Kinetic equations and stationary energy spectra of weakly non-linear internal gravity waves. // *Dyn. Atmos. Oceans*. 2000. 32. 81–112.
- Cairns J. L.* Internal wave measurements from a midwater float // *Journal of Geophysical Research* (1896-1977). 1975. 80, 3. 299–306.
- Callies J., Ferrari R.* Interpreting Energy and Tracer Spectra of Upper-Ocean Turbulence in the Submesoscale Range (1–200 km) // *Journal of Physical Oceanography*. 2013. 43. 2456–2474.
- Celani A., Cencini M., Mazzino A., Vergassola M.* Active and passive fields face to face // *New J. Phys.* 2004. 6.

- Celani A., Musacchio S., Vicenzi D.* Turbulence in more than two and less than three dimensions // *Phys. Rev. Lett.* 2010. 104.
- Cho J. Y. N., Lindborg E.* Horizontal velocity structure functions in the upper troposphere and lower stratosphere // *Journal of Geophysical Research Atmospheres.* 2001. 106.
- Clark di Leoni P., Cobelli P. J., Mininni P. D.* The spatio-temporal spectrum of turbulent flows // *The European Physical Journal E.* 2015. 38. 1–10.
- Dauxois T., Joubaud S., Odier P., Venaille A.* Instabilities of internal gravity waves // *Annu. Rev. Fluid Mech.* 2018. 50. 1–28.
- Dewan E. M.* Stratospheric spectra resembling turbulence // *Science.* 1979. 204. 832–835.
- Dewan E. M.* Saturated-cascade similitude theory of gravity wave spectra // *Journal Geophysical Research.* 1997. 29. 799–817.
- Dewan E.M., Picard R.H., O’Neil R.R., Gardiner H.A., Gibson J., Mill J.D., Richards E., Kendra M., Gallery W. O.* MSX satellite observations of thunderstorm-generated gravity waves in mid-wave infrared images of the upper stratosphere // *Geophysical Research Letters.* 1998. 25, 7. 939–942.
- Egbert G. D., Ray R. D.* Significant dissipation of tidal energy in the deep ocean inferred from satellite altimeter data // *Nature.* 2000. 405. 775–778.
- Emanuel K. A.* Overview and definition of mesoscale meteorology // In *Mesoscale Meteorology and Forecasting.* 1986. 1–17.
- Ferrari R., Jansen M. F., Adkins J. F., Burke A., Stewart A. L., Thomson A.F.* Antarctic sea ice control on ocean circulation in present and glacial climates. // *Proceedings of the National Academy of Sciences of the United States of America.* 2014. 111. 8753–8758.
- Ferrari R., Wunsch C.* The distribution of eddy kinetic and potential energies in the global ocean // *Tellus A.* 03 2010.
- Fofonoff N. P.* Spectral characteristics of internal waves in the ocean. 1969.
- Gage K. S.* Evidence for a $k^{-5/3}$ law inertial range in mesoscale two-dimensional turbulence // *J. Atmos. Sci.* 1979. 36. 1950–1954.
- Garrett C.* Internal tides and ocean mixing // *Science.* 2003. 301. 1858–1859.
- Garrett C., Munk W.* Space-time scales of internal waves: A progress report // *Journal of Geophysical Research.* 1975. 80, 3. 291–297.
- Garrett C., Munk W.* Internal waves in the ocean // *Annual Review of Fluid Mechanics.* 1979. 11. 339–369.
- Gaube P., Chelton D. B., Samelson R. M., Schlax M. G., O’Neill L. W.* Satellite observations of mesoscale eddy-induced Ekman pumping // *Journal of Physical Oceanography.* 2015. 45. 104–132.
- Ghaemsaïdi S. J., Joubaud S., Dauxois T., Odier P., Peacock T.* Nonlinear internal wave penetration via parametric subharmonic instability // *Physics of Fluids.* 2016. 28, 1. 011703.
- Godeferd F., Staquet C.* Statistical modelling and direct numerical simulations of decaying stably stratified turbulence. Part 2. Large-scale and small-scale anisotropy // *Journal of Fluid Mechanics.* 2003. 486. 115–159.

- Godeferd F. S., Cambon C.* Detailed investigation of energy transfers in homogeneous stratified turbulence // *Physics of Fluids*. 1994. 6. 2084–2100.
- Godoy-Diana R., Chomaz J.M., Billant P.* Vertical length scale selection for pancake vortices in strongly stratified viscous fluids // *Journal of Fluid Mechanics*. 2004. 504. 229–238.
- Gostiaux L., Dauvois T.* Laboratory experiments on the generation of internal tidal beams over steep slopes // *Physics of Fluids*. 2007. 19.
- Hasselmann K.* Feynman diagrams and interaction rules for wave-wave scattering // *Rev. Geophys.* 1966. 4. 1–32.
- Hasselmann K.* A criterion for nonlinear wave stability. // *Journal Fluid Mechanics*. 1967. 3. 737–39.
- Herbert C., Marino R., Rosenberg D., Pouquet A.* Waves and vortices in the inverse cascade regime of stratified turbulence with or without rotation // *Journal of Fluid Mechanics*. 2016. 806. 165–204.
- Herring J. R., Métais O.* Numerical experiments in forced stably stratified turbulence. // *Journal Fluid Mechanics*. 1989. 202. 97–115.
- Holford J.M., Linden P.F.* Turbulent mixing in stratified fluid // *Dyn. Atmos. Oceans*. 1999. 173–198.
- Holloway G.* Oceanic Internal Waves Are Not Weak Waves // *Journal of Physical Oceanography*. 1980. 10, 6. 906–914.
- Joubaud S., Munroe J., Oddier P., Dauvois T.* Experimental parametric subharmonic instability in stratified fluids // *Physics of Fluids*. 2012. 24, 4. 041703.
- Katz E. J.* Profile of an Isopycnal Surface in the Main Thermocline of the Sargasso Sea // *Journal of Physical Oceanography*. 1973. 3, 4. 448–457.
- Kumar A., Verma M. K., Sukhatmae J.* Phenomenology of two-dimensional stably stratified turbulence under large-scale forcing // *Journal of Turbulence*. 2017. 18. 219–239.
- Kunze E.* A Unified Model Spectrum for Anisotropic Stratified and Isotropic Turbulence in the Ocean and Atmosphere // *Journal of Atmospheric Sciences*. 2019.
- Lamorgese A. G., Caughey D. A., Pope S. B.* Direct numerical simulations of homogeneous turbulence with hyperviscosity // *Phys. Fluids*. 2005. 17.
- Lapeyre G., Klein P., Hua B. L.* Does the tracer gradient vector align with the strain eigenvectors in 2D turbulence? // *Physics of Fluids*. 1999. 11.
- Le Reun T., Favier B., Bars M. Le.* Parametric instability and wave turbulence driven by tidal excitation of internal waves // *Journal of Fluid Mechanics*. 2018. 840. 498–529.
- Lelong M. P., Riley J. J.* Internal wave-vortical mode interactions in strongly stratified flows // *Journal of Fluid Mechanics*. 1991. 232. 1–19.
- Li Q., Lindborg E.* Weakly or Strongly Nonlinear Mesoscale Dynamics Close to the Tropopause? // *Journal of the Atmospheric Sciences*. 2018. 75, 4. 1215–1229.
- Lilly D. K.* Stratified turbulence and the mesoscale variability of the atmosphere // *Journal of the Atmospheric Sciences*. 1983. 40. 749–761.

- Lindborg E.* The energy cascade in a strongly stratified fluid // *Journal of Fluid Mechanics*. 2006. 550. 207–242.
- Lindborg E., Brethouwer G.* Stratified turbulence forced in rotational and divergent modes // *Journal of Fluid Mechanics*. 2007. 586. 83–108.
- Lindborg E., Riley J. J.* A condition on the average Richardson number for weak non-linearity of internal gravity waves // *Tellus A: Dynamic Meteorology and Oceanography*. 2007. 59, 5. 781–784.
- Liu Y., , Jing Z., Wu L.* Wind Power on Oceanic Near-Inertial Oscillations in the Global Ocean Estimated From Surface Drifters // *Geophysical Research Letters*. 2019. 46, 5. 2647–2653.
- Lvov Y. V., Polzin K. L., TabakPolzin E. G.* Energy Spectra of the Ocean’s Internal Wave Field: Theory and Observations // *Phys. Rev. Lett.* 2004. 92. 128501.
- MacKinnon J.* Mountain waves in the deep ocean // *Nature*. 2013. 501. 321–322.
- Maffioli A., Brethouwer G., Lindborg E.* Mixing efficiency in stratified turbulence // *Journal of Fluid Mechanics*. 2016. 795.
- Maurer P., Joubaud S., Odier P.* Generation and stability of inertia–gravity waves // *Journal of Fluid Mechanics*. 2016. 808. 539–561.
- Miles J.* On the stability of heterogeneous shear flows // *Journal of Fluid Mechanics*. 1961. 10. 496–508.
- Millard R.* Further comments on vertical temperature spectra in the MODE region // *MODE Hot Line News*. 1972. 18, 1.
- Moffatt H. K.* The topology of scalar fields in 2D and 3D turbulence // *IUTAM Symposium on Geometry and Statistics of Turbulence*. 1999. 59. 13–22.
- Mohanam A. V., Bonamy C., Augier P.* FluidFFT: Common API (C++ and Python) for Fast Fourier Transform HPC Libraries // *J. Open Research Software*. 2019a. 7.
- Mohanam A. V., Bonamy C., M. Calpe Linares, P. Augier.* FluidSim: modular, object-oriented Python package for high-performance CFD simulations // *J. Open Research Software*. 2019b. 7.
- Mordant N., Miquel B.* Intermittency and emergence of coherent structures in wave turbulence of a vibrating plate // *Phys. Rev. E*. Oct 2017. 96. 042204.
- Munk W. H., Wunsch C.* Abyssal recipes II: Energetics of tidal and wind mixing // *Deep-Sea Research*. 1998. 45. 1977–2010.
- Müller P., Holloway G., Henvey F., Pomphrey N.* Nonlinear interactions among internal gravity waves // *Rev. Geophys.* 1986. 24. 493–536.
- Nastrom G. D., Gage K. S.* A climatology of atmospheric wavenumber spectra of wind and temperature observed by commercial aircraft // *Journal of Atmospheric Science*. 1985. 42. 950–960.
- Nycander J.* Generation of internal waves in the deep ocean by tides // *Journal of Geophysical Research*. 2005. 110.

- Park Y. G., Whitehead J. A., Gnanadeskian A.* Turbulent mixing in stratified fluids: layer formation and energetics // *Journal of Fluid Mechanics*. 1994. 279. 279–311.
- Pedlosky J.* *Geophysical Fluid Dynamics*. 1987.
- Polzin K. L., Lvov Y. V.* Toward regional characterizations of the oceanic wavefield // *Reviews of Geophysics*. 2011. 49, 4.
- Rahmstorf S.* Ocean circulation and climate during the past 120,000 years // *Nature*. 2002. 419. 207–214.
- Richardson L.F.* *Weather prediction by numerical process*. 1922.
- Riley J. J., Lelong M. P.* Fluid motion in the presence of strong stable stratification // *Annu. Rev. Fluid Mechanics*. 2000. 32. 613–657.
- Riley J. J., Lindborg E.* Stratified Turbulence: A Possible Interpretation of Some Geophysical Turbulence Measurements // *Journal of the Atmospheric Sciences*. 2008. 65. 2416 – 2424.
- Riley J. J., Metcalfe R. W., Weissman M. A.* Direct numerical simulations of homogeneous turbulence in density-stratified fluids. // *Proc. AIP Conf*. 1981. 76. 79–112.
- Sanford T. B.* Observations of the vertical structure of internal waves // *Journal of Geophysical Research (1896-1977)*. 1975. 80, 27. 3861–3871.
- Schuster U., Watson A.* A variable and decreasing sink for atmospheric CO₂ in the North Atlantic. // *Journal of Geophysical Research*. 2007. 112.
- Smith L. M., Waleffe F.* Generation of slow large scales in forced rotating stratified turbulence, // *Journal of Fluid Mechanics*. 2002. 451.
- Staquet C., Sommeria J.* Internal gravity waves: from instabilities to turbulence // *Annual Review Fluid Mechanics*. 2002. 34. 559–593.
- Sutherland B. R.* *Internal Gravity Waves*. 2010.
- Sutherland B.R., Achatz U., Caulfield C. P., Klymak J. M.* Recent progress in modeling imbalance in the atmosphere and ocean // *Phys. Rev. Fluids*. Jan 2019. 4. 010501.
- Taylor G. I.* Statistical theory of turbulence part i - ii // *Proc. R. Soc. Lond*. 1935. 421–464.
- Thorpe S.* *An introduction to ocean turbulence*. 2005. 340–367.
- Vallis G. K.* *Atmospheric and Oceanic Fluid Dynamics*. 2006.
- Waite M. L.* Stratified turbulence at the buoyancy scale // *Physics of Fluids*. 2011. 23, 6. 066602.
- Waite M. L., Bartello P.* Stratified turbulence dominated by vortical motion // *Journal of Fluid Mechanics*. 2004. 517. 281–308.
- Waite M. L., Bartello P.* Stratified turbulence generated by internal gravity waves // *Journal of Fluid Mechanics*. 2006a. 546. 313–339.
- Waite M. L., Bartello P.* The transition from geostrophic to stratified turbulence // *Journal of Fluid Mechanics*. 2006b. 568. 89–108.

-
- Webb P.* Introduction to Oceanography. 2019.
- Webster F.* Estimates of the coherence of ocean currents over vertical distances // Deep Sea Research and Oceanographic Abstracts. 1972. 19, 1. 35 – 44.
- Wunsch C., Ferrari R.* Vertical mixing, energy, and the general circulation of the ocean // Annual Review of Fluid Mechanics. 2004. 36. 939–942.
- Wurtele M.G., Sharman R.D., Datta A.* Atmospheric lee waves // Annual Review Fluid Mechanics. 1996. 28. 429–476.
- Yokoyama N., Takaoka M.* Energy-based analysis and anisotropic spectral distribution of internal gravity waves in strongly stratified turbulence // Phys. Rev. Fluids. Oct 2019. 4. 104602.
- Zhang Z., Wang W., Qiu B.* Oceanic mass transport by mesoscale eddies // Science. 2014. 345. 322–324.
- Zhang Z., Wang Y., Zhang Y., Huang R. X.* Universal structure of mesoscale eddies in the ocean // Geophysical Research Letters. 07 2013. 40.

Abstract

The oceanic motions are composed of eddies with a very large horizontal scale and 3D propagating internal gravity waves. Its kinetic energy spectra follow the well-known Garrett and Munk spectrum, which is usually interpreted as the signature of interacting internal gravity waves. Our main motivation is to reproduce the turbulence regime observed in nature by forcing waves.

Two-dimensional (2D) stratified flows on a vertical cross-section differ from its analogous three-dimensional flows in its lack of vertical vorticity, supporting only waves and shear modes. In this PhD work, we perform a numerical study of 2D stratified turbulence forced with internal gravity waves. We get rid of the shear modes, sustaining a system only with wave modes. Unlike precedent studies, the forcing is applied to a localized region of the spectral space, in which forced internal waves have a similar time scale. We force intermediate-scale waves to allow the dynamics to develop both upscale and downscale energy cascade.

We first present the different regimes of 2D stratified turbulence with a particular interest in the ocean-like regime, i.e. strong stratification and large Reynolds number. The dynamics of the energy cascade is analysed by means of the spectral energy budget. Furthermore, we check if it is possible to obtain turbulence driven by weakly non-linear interacting waves by performing a spatio-temporal analysis. To conclude, we report results of numerical simulations forced either on the vorticity or on the eigenmode of the Navier-Stokes equations in order to study the degree of universality of 2D stratified turbulence with respect to the forcing.

Résumé

Les écoulements océaniques sont composés des tourbillons ayant une grande échelle horizontale et des ondes internes de gravité. Le spectre d'énergie cinétique suit le fameux spectre de Garrett et Munk qui est habituellement interprété comme la signature des ondes internes de gravité. Notre motivation principale est donc de reproduire le régime de turbulence observé dans la nature avec un système forcé seulement avec des ondes.

Les écoulements stratifiés bidimensionnels (2D) sur une section transversale verticale diffèrent des écoulements stratifiés tridimensionnels par l'absence de vorticit  verticale et par la pr sence d'ondes et de modes de cisaillement. Dans ce travail de th se, nous effectuons une  tude num rique de la turbulence stratifi e 2D forc e par des ondes internes de gravit . Nous  liminons les modes de cisaillement pour avoir un syst me uniquement constitu  d'ondes. Contrairement aux  tudes pr c dentes, le for age est appliqu    une r gion localis e de l'espace spectral. Nous for ons aussi les ondes avec une  chelle spatiale interm diaire pour permettre le d veloppement d'une cascade d' nergie directe et aussi inverse.

Nous pr sentons d'abord les diff rents r gimes de turbulence stratifi e 2D avec un int r t particulier au r gime typique de l'oc an avec une forte stratification et un grand nombre de Reynolds. La dynamique de la cascade d' nergie est analys e par un bilan  nerg tique spectral. Ensuite, nous v rifions s'il est possible d'obtenir un r gime de turbulence d'onde faible en r alisant une analyse spatio-temporelle. Nous  tudions enfin le degr  d'universalit  de la turbulence stratifi e 2D par rapport au for age.